DESIGN, ANALYSIS AND APPLICATION OF NOVEL

HYBRID EXCITATION FLUX MODULATION MACHINES

XING ZHAO

PhD

The Hong Kong Polytechnic University

2020

The Hong Kong Polytechnic University

Department of Electrical Engineering

Design, Analysis and Application of Novel Hybrid
Excitation Flux Modulation Machines

Xing Zhao

A thesis submitted in partial fulfillment of the requirements
for the degree of Doctor of Philosophy

February 2020

CERTIFICATE OF ORIGINALITY

I hereby declare that this thesis is my own work and that, to the best of my knowledge and belief, it reproduces no material previously published or written, nor material that has been accepted for the award of any other degree or diploma, except where due acknowledgement has been made in the text.

Signature

Name   Xing Zhao

Date   2020/02/14

ABSTRACT

Hybrid excitation machine, which combines the PM excitation and wound field excitation, has the potential to achieve both good torque density and flux regulation ability, and thus can be a potential candidate for electric or hybrid electric vehicle applications. For traditional PM machines in which PMs are arranged at rotor side, realizing a hybrid excitation structure usually needs brush and slip rings, which decreases system reliability. Although some design techniques featured by radial and axial combined magnetic circuits can eliminate brush and slip rings, they increase the complexity of mechanical structure, and worse, degrade torque density due to redundant air gap. For emerging stator PM machines with PMs arranged at stator side, the corresponding hybrid excitation structures can naturally achieve good flux regulation with a brushless structure. However, their torque density is poor than that of rotor PM counterparts, due to low PM utilization, extra DC saturation in stator core, and the space conflict between the AC field coils and DC field coils. Therefore, there is need of new hybrid excitation technologies, which realizes a brushless structure and integrates both good torque density and flux regulation ability.

In the recent decades, with the development of flux modulation theory, a variety of new design technologies have been proposed to increase machine torque density by utilizing modulated air gap harmonics. Moreover, the flux modulation principle allows more flexible arrangement of excitation sources and more possible slot pole combinations. This thesis aims to give a synthesis and investigation of new brushless hybrid excitation flux modulation machines with both good torque density and flux regulation ability.

A new hybrid excitation Vernier reluctance machine is proposed, in which consequent-pole PMs are artificially introduced into stator slots to generate flux modulation effect and

interact redundant armature harmonics, so that the machine torque density is greatly improved compared to its non-PM counterpart. Moreover, the introduced slot PMs share a parallel magnetic circuit with armature excitation, thus providing bidirectional flux regulation ability and demagnetization withstand ability. Besides, to address the space conflict between AC armature coils and DC field coils in the proposed topology, the zero-sequence current control is applied to generate DC current component in AC armature coils, which can function as virtual DC field coils at design stage and contributes to improve torque density and efficiency. The theoretical analysis, finite element simulation and protype experiments are conducted to demonstrate the proposed topology and its improved design based on zero-sequence current control.

A new hybrid excitation dual-PM Vernier machine is proposed. This machine adopts dual consequent-pole PMs arranged in both stator slots and rotor slots, thus contributes to boosted air gap flux density and increased torque density. Moreover, DC field excitation is introduced in stator to provide an extra flux weakening variable, which can be coordinated with the traditional d-axis vector flux weakening to further extend the torque speed range. Further, to address the issue of parasitic stator DC saturation effect in the proposed topology, an improved design is proposed, namely relieving-DC-saturation hybrid excitation dual-PM Vernier machine. Especially, a constant flux bias is constructed in stator core by use of tangentially-magnetized stator slots PMs, thus to cancel the DC flux component excited by DC field excitation. In this way, the DC saturation effect in stator core can be eliminated, which improves machine torque density and flux regulation ability. The theoretical analysis, finite element modeling and prototype experiments are performed to verify the proposed topology and its improved design with eliminated DC saturation.

PUBLICATIONS ARISING FROM THE THESIS

[1] **X. Zhao**, S. Niu, X. Zhang and W. Fu, "A new relieving-DC-saturation hybrid excitation Vernier machine for HEV starter generator application," *IEEE Trans. Ind. Electron*., early access, 2019.

[2] **X. Zhao**, S. Niu, X. Zhang and W. Fu, " Design of a new relieving-DC-saturation hybrid reluctance machine for fault-tolerant in-wheel direct drive," *IEEE Trans. Ind. Electron*., early access, 2019.

[3] **X. Zhao**, S. Niu. " A new slot-PM Vernier reluctance machine with enhanced zero sequence current excitation for electric vehicle propulsion," *IEEE Trans. Ind. Electron*., early access, 2019.

[4] **X. Zhao**, S. Niu and W. Fu. "Design of a novel parallel-hybrid-excited dual-PM machine based on armature harmonics diversity for electric vehicle propulsion," *IEEE Trans. Ind. Electron*., vol. 66, no. 6, pp. 4209-4219, Jun. 2019.

[5] **X. Zhao**, and S. Niu. "Design of a novel parallel-hybrid-excited Vernier reluctance machine with improved utilization of redundant winding harmonics," *IEEE Trans. Ind. Electron*., vol. 65, no. 11, pp. 9056-9067, Nov. 2018.

[6] **X. Zhao**, and S. Niu. "Design and optimization of a new magnetic-geared pole-changing hybrid excitation machine," *IEEE Trans. Ind. Electron*., vol. 64, pp. 943-952, Dec. 2017.

[7] **X Zhao**, and S. Niu. "Development of a novel transverse flux tubular linear machine with parallel and complementary PM magnetic circuit for precision industrial processing," *IEEE Trans. Ind. Electron*., vol. 66, no. 6, pp. 4945-4955, Jun. 2019.

[8] **X. Zhao**, and S. Niu. "Design and optimization of a novel slot-PM-assisted variable flux reluctance generator for hybrid electric vehicles," *IEEE Trans. Energy Convers.,* vol. 33, no. 4, pp. 2102-2111, Dec. 2018.

[9] **X. Zhao**, S. Niu and W. Fu, "A new modular relieving-DC-saturation Vernier reluctance machine excited by zero-sequence current for electric vehicle," *IEEE Trans. Magn.,* vol. 55, no. 7, pp. 1-5, Jul. 2019.

[10] **X. Zhao**, S. Niu and W. Fu, "A novel Vernier reluctance machine excited by slot

PMs and zero-sequence current for electric vehicle," *IEEE Trans. Magn.,* vol. 55, pp. 1-5, Jun. 2019.

[11]   **X. Zhao**, S. Niu and W. Fu, " Sensitivity analysis and design optimization of a new hybrid-excited dual-PM generator with relieving-DC-saturation structure for stand-alone wind power generation," *IEEE Trans. Magn.,* early access, 2019

[12]   **X. Zhao**, S. Niu and W. Fu, "Torque component quantification and design guideline for dual permanent magnet Vernier machine," *IEEE Trans. Magn.,* vol. 55, no. 6, pp. 1-5, Jun. 2019.

[13]   **X Zhao**, S. Niu and T. Ching. "Design and analysis of a new brushless electrically excited claw-pole generator for hybrid electric vehicle," *IEEE Trans. Magn.*, vol. 54, no. 11, pp. 1-5, Nov. 2018.

[14]   **X Zhao**, and S. Niu. "Investigation of a new hybrid excitation machine with auxiliary winding for energy recycling," *IEEE Trans. Magn.*, vol. 53, no. 11, pp. 1-5, Nov. 2017.

[15]   **X Zhao**, and S. Niu. "Design of a novel consequent-pole transverse-flux machine with improved permanent magnet utilization," *IEEE Trans. Magn.*, vol. 53, pp. 1-5, Nov. 2017.

[16]   **X Zhao**, S. Niu and W. Fu. " Design and comparison of electrically excited double rotor flux switching motor drive systems for automotive applications," *CES Trans. Electr. Mach. Syst.*, Jun. 2018. **(Invited Paper)**

[17]   S. Niu, **X Zhao**, X. Zhang, and T. Sheng, "A novel axial-flux-complementary doubly salient machine with boosted PM utilization for cost-effective direct-drive applications," *IEEE Access,* vol. 7, pp. 145970-145977, 2019.

[18]   X. Zhang, **X Zhao** and S. Niu. "A novel dual-structure parallel hybrid excitation machine for electric vehicle propulsion". *Energies*. Jan. 2019.

[19]   S. Niu, T. Sheng, **X Zhao** and X. Zhang, "Operation principle and torque component quantification of short-pitched flux-bidirectional-modulation machine*," IEEE Access,* vol. 7, pp. 136676-136685. 2019.

[20]   **X. Zhao**, S. Niu, X. Zhang and W. Fu, " Flux-modulated relieving-DC-saturation hybrid reluctance machine with synthetic slot PM excitation for electric vehicle in-wheel propulsion," *IEEE Trans. Ind. Electron.*, Under review.

ACKNOWLEDGEMENTS

TABLE OF CONTENTS

LIST OF FIGURES

LIST OF TABLES

CHAPTER 1. INTRODUCTION

1.1 RESEARCH BACKGROUD

With the increasing concern of environmental protection and energy saving, developing electric vehicles (EV) or hybrid electric vehicles (HEV) has become an important trend over the world. Electrical machine, as the core component in EV/HEV propulsion system, has been widely investigated in literature. Considering the various working conditions of vehicles, the main design requirements of electrical machines can be listed as,

1) High torque density and power density for cold starting and low-speed climbing;

2) Minimized torque ripple and acoustic noise for smooth driving;

3) Strong flux weakening ability for high-speed cruising;

4) High efficiency over a drive circle to extend driving mileage;

5) Good fault-tolerant ability;

6) Low cost and easy maintenance.

The traditional permanent magnet (PM) machines have been well explored for EV/HEV propulsion, including the interior PM machine (IPM) and surface-mounted PM machine (SPM). IPM has the advantages of high torque density and good flux weakening ability, due to the effective combination of PM field and saliency effect. However, IPM has relatively large torque ripple caused by its non-sinusoidal PM field. SPM can obtain both good torque density and low torque ripple ratio. However, flux weakening ability is a long-existing issue in SPM due to its non-saliency effect. Moreover, with the limited supply and volatile price of PMs, the cost of traditional PM machines increases tremendously.

Hybrid excitation machine (HEM) is a potential solution for EV/HEV propulsion. By reasonably combing PM excitation and wound excitation, HEM can achieve improved flux

regulation ability, extended constant power speed range (CPSR) as well as higher efficiency over a drive circle, while its torque density is less than that of traditional PM machines. Another emerging topology, flux modulation machine (FMM), has attracted much attention in the last decades due to its flexible slot pole combination and excellent torque density arising from so-called magnetic gearing effect. This thesis aims to perform a synthesis and investigation of a series of new hybrid excitation flux modulation machines (HE-FMM) for EV/HEV applications, which integrates both good torque density and flux regulation ability, by means of machine topology innovation, analytical modeling, design optimization, finite element analysis and prototype experiments.

1.2 REVIEW OF HYBRID EXCITATION MACHINES

Various topologies of HEMs have been proposed in literature as the combination of PM excitation and wound excitation is very flexible. According to the magnetic circuit relation between two excitation sources, HEMs can be classified into two groups, namely series HEMs and parallel HEMs. Series HEMs usually need less structure modification of PM machines, and meanwhile completely inherit the advantages of PM machines such as high torque density and power factor. However, in series HEMs, the wound field flux must pass through PMs, and due to the low PM permeability, the reluctance for wound field return path is quite high. Therefore, a large ampere-turn field potential is required to interact with PM excitation, which leads to a relatively lower efficiency of field adjustment, as well as potential demagnetization risk of magnet materials. In parallel PHEMs, two excitation sources own independent magnetic paths, which accordingly provides better improved field regulation ability and less PM demagnetization risk. However, some sacrifice in terms of torque density and power factor is inevitable in HEMs. It should be mentioned that, in

some HEMs, both series and parallel magnetic circuits exist when tuning wound excitation, and thus different analytical methods should be applied at different operation modes.

Moreover, according to the layout of PM sources, HEMs can be divided into three groups, namely rotor PM HEMs, stator PM HEMs and dual PM HEMs, respectively. Rotor PM HEMs are usually developed from traditional PM machines, including surface-mounted PM machine (SPM) and interior PM machine (IPM). The PM-assisted wound field synchronous machine (PMa-WFSM) can be referred as a special case of rotor PM HEMs. Stator PM HEMs are basically derived from stator PM machines, including doubly-salient machines (DSM), flux switching machines (FSM) and flux reversal machines (FRM). A special case, PM-assisted reluctance machine is also included into stator PM HEMs in this thesis. Dual PM HEM is an emerging topology, in which two sets of PMs are arranged at both stator and rotor sides, thus to achieve boosted machine torque density. A state-of-art review of three kinds of HEMs is presented as follows.

1.2.1 Rotor PM HEMs

SPM owns the merits of high torque density, power factor and efficiency, while its poor flux weakening (FW) ability is limited due to zero magnetic saliency [1-3]. To improve the FW ability of SPM and extend its CPSR, different HEM topologies based on SPM are developed by combing DC field coils and PMs at rotor side. Fig. 1.1 shows two typical configurations [4-5]. One design is housing DC field coils under rotor PM poles to directly control PM field, as shown in Fig. 1.1(a), which belongs to a series hybrid structure. Another design is replacing part of PM poles by DC field coils as shown in Fig. 1.1(b), which belongs to a parallel hybrid structure. Fig. 1.2 presents the rotor design of a parallel hybrid structure developed from consequent-pole SPM [6].
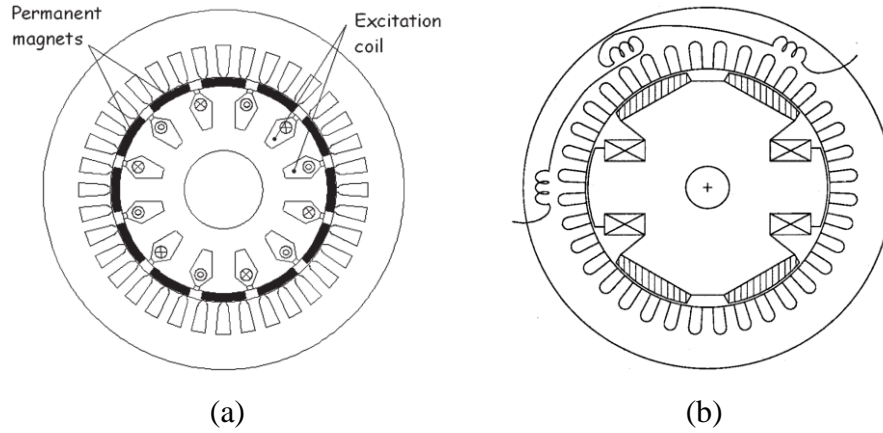
Fig. 1.1 Different hybrid structures for SPM. (a) Parallel type [4]. (b) Series type [5].
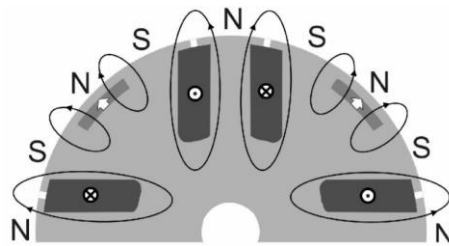
Fig. 1.2 Parallel hybrid structure for consequent-pole SPM [6].
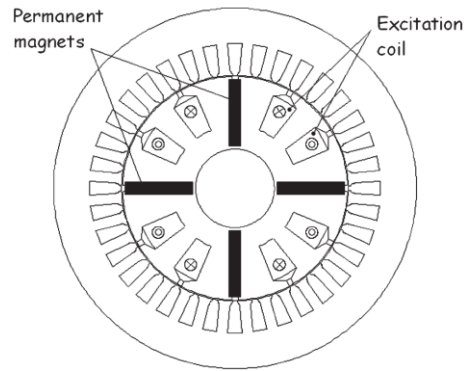
Fig. 1.3 Parallel hybrid structure for Spoke IPM [9].

IPM has the advantages of high torque density and efficiency. Besides, its FW ability is good, benefiting from magnetic saliency effect [7-8]. Some researchers try to introduce DC field coils into a spoke-type IPM [9], as presented in Fig. 1.3. The DC field terminal can serve as an extra FW control variable, which can be combined with the traditional d-axis vector flux weakening operation to further extend machine CPSR.

In general, the above HEM topologies based on SPM and IPM, can be derived by flexibly combining DC field coils and PMs at rotor side. However, one common issue for these HEM topologies is that brush and slip rings are needed to inject DC field current at rotor side, which increases the system complexity and decreases its reliability.

(a)   (b)
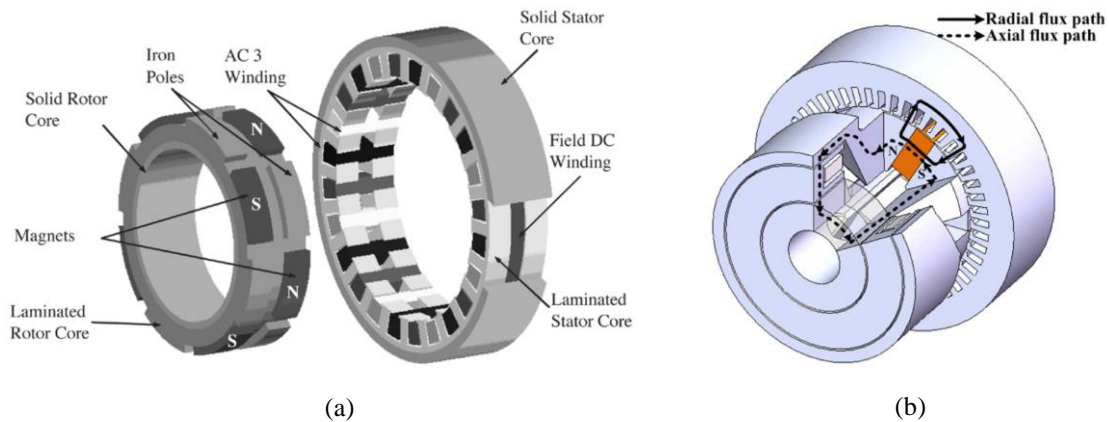
Fig. 1.4 Brushless hybrid structures with combined radial and axial magnetic circuit. (a) Brushless hybrid SPM using consequent-pole rotor and segmented stator [10-11]. (b) Brushless hybrid IPM using magnetic shunting rotor [12-13].

To eliminate the brush and slip rings, some brushless rotor PM HEM topologies are proposed by combing radial and axial magnetic circuits [10-13]. Fig. 1.4(a) shows a typical brushless hybrid SPM structure. In this machine, the DC coils is sandwiched between two stator segments and produce axial DC field to interact with radial PM field. The rotor uses a consequent-pole structure to reduce the loop reluctance of DC field excitation. The main drawback of this machine is the torque density sacrifice, since the air gap under DC field coils will not participate in electromagnetic energy conversion. Fig. 1.4(b) shows a typical brushless hybrid IPM. This machine utilizes a magnetic shunting rotor structure, in which the ends of rotor core are extended in axial direction to house DC field coils. By regulating DC field excitation, the PM leakage flux in axial direction can be controlled, and thus both

flux weakening and flux enhancing operation can be achieved. However, the magnetic shunting rotor increases the machine stack length, and thus the machine torque density is reduced. It can be concluded that, combing radial and axial magnetic circuits can realize brushless designs in rotor PM HEMs, while the machine mechanical complexity is usually increased, and torque density is reduced to some extent.
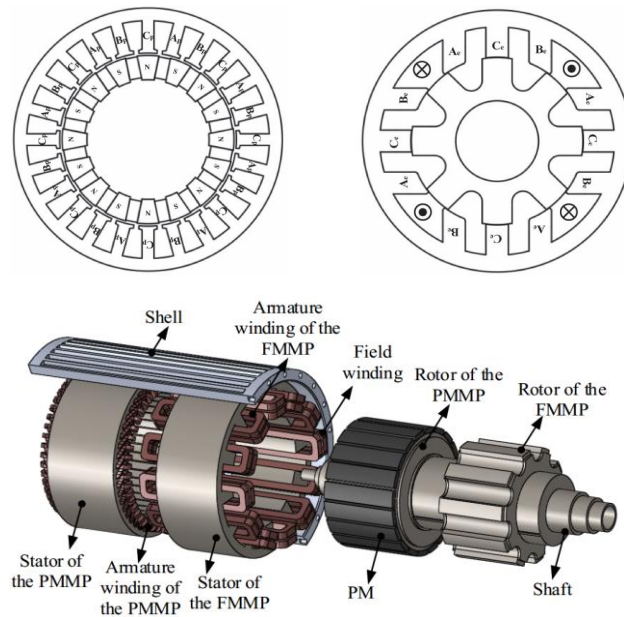
Fig. 1.5 Brushless hybrid structure by combining SPM and DC-excited doubly salient reluctance machine [14-16].

Another hybrid design is directly combining two machines with hybrid excitation sources. Fig. 1.5 shows a parallel rotor PM HEM, which combines a PM brushless machine and DC-excited reluctance machine in axial direction [14-16]. Two machine rotors share the common shaft and integrated as one mechanical port. The armature windings in two machines are cascaded together and form a single electrical port. Since the DC field coils are arranged in stator, brush and slip rings are eliminated in this machine. This topology realizes the decoupling of electrical power arising from PM excitation and DC field excitation. The issue is the machine mechanical complexity, which leads to increased manufacturing cost. Moreover, considering the influence of winding ends, the wasted air gap between two stators is remarkable, which decreases the machine torque density.
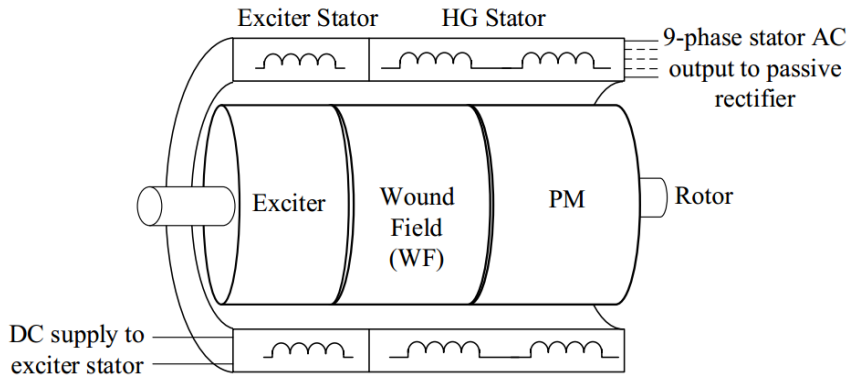
Fig. 1.6 Brushless hybrid structure by combining SPM and two-stage-excited brushless wound field synchronous machine [17-21].

By combing WFSM and SPM in axial direction, a three-stage brushless rotor PM HEM is proposed in [17-21], as shown in Fig. 1.6. Since the torque density of WFSM is larger than that of DC-excited reluctance, the combination of WFSM and SPM is more attractive compared to the above PM and reluctance combined solution. However, in this topology, an extra exciter and rotary rectifier are needed for brushless operation of WFSM.

In the recent years, an emerging solution, using inverter-fed AC field excitation to construct brushless rotor PM HEM topology, has attracted more and more attention in literature [22-23]. Fig. 1.7(a) shows a newly proposed dual-stator hybrid SPM. In this machine, AC field coils are arranged in the inner stator and fed by an independent inverter. In this way, a rotating wound field can be generated, which is similar with that produced by rotating DC field coils equipped with brush and slip rings. Further, this rotating wound field, together with rotating PM field, synchronously interact with armature field for energy conversion, which constitutes a brushless hybrid structure. This solution is interesting. However, the mechanical structure to house dual stators is complicated. Besides, one more inverter is needed for regulating AC field excitation, which increases the system cost. A simplified topology is further proposed as presented in Fig. 1.7(b), which integrates both

AC field winding and armature winding in a single stator. The mechanical structure is simplified. However, since AC field excitation and armature field couples in stator core, the saturation level of stator core becomes high, which limits torque density. Fig. 1.8 shows a hybrid IPM with inverter-fed AC field excitation in axial direction proposed in [24-25]. Although this machine realizes a brushless flux regulation by integrating an axial machine, it suffers from increased machine stack length, reduced torque density, more complicated mechanical structure as well as drive circuits, which limits its practical applications.

(a)   (b)
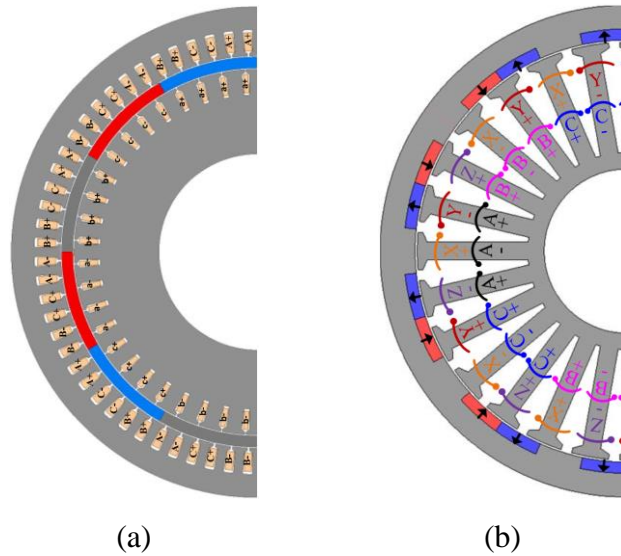
Fig. 1.7 Brushless hybrid structures of SPM with inverter-fed AC field excitation. (a) Double-stator structure [22]. (b) Double-winding structure [23].
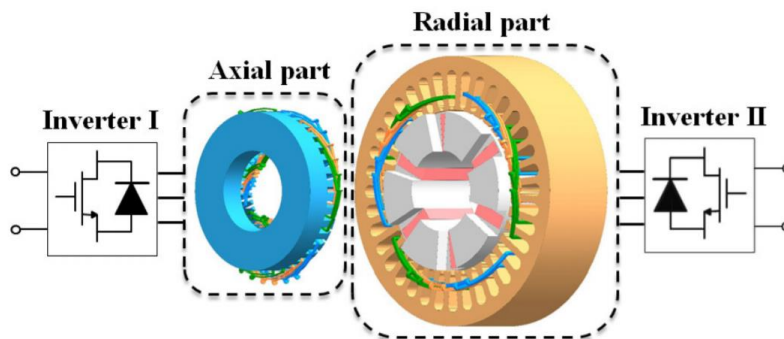
Fig. 1.8 Brushless hybrid structures of IPM with inverter-fed AC field excitation [24-25].
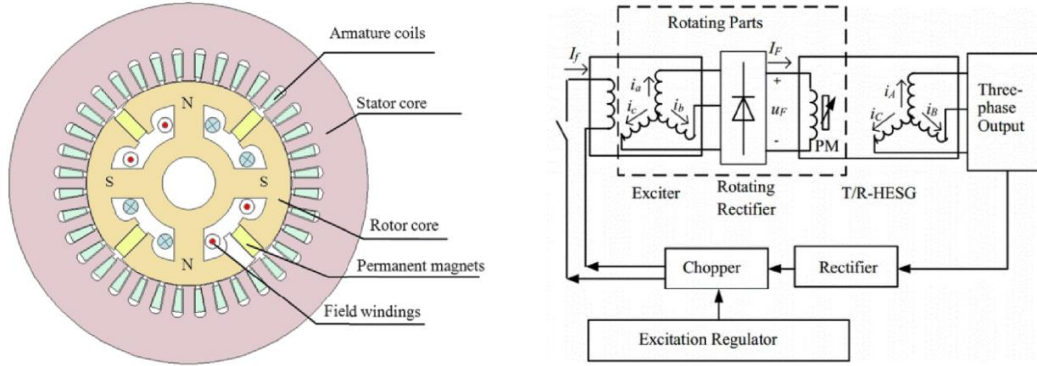
Fig. 1.9 Two-stage brushless PM-assisted WFSM [26-27].
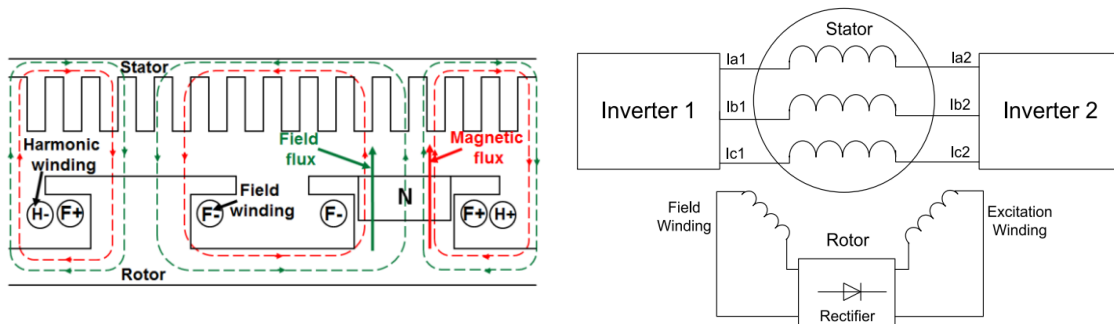
Fig. 1.10 Harmonic excitation brushless PM-assisted WFSM [28-29].

Different from the abovementioned rotor PM HEMs, a special case of hybrid excitation topology, namely PM-assisted WFSMs in which the PMs are introduced into WFSMs for torque and efficiency performance improvement [26-29], are also classified into rotor PM HEMs in this thesis. Fig. 1.9 presents a PM-assisted WFSM with tangentially-magnetized PMs embedded into adjacent wound poles, so that a two-stage brushless excitation solution can be realized by eliminating the extra PM exciter in the traditional three-stage brushless WFSM system. Fig. 1.10 presents a novel PM-assisted WFSM with harmonics excitation winding. In this topology, the brushless structure is realized by regulating common mode voltage under the open winding drive structure to generate induced voltage in harmonics excitation winding located at rotor side. A certain PMs are also introduced into the wound rotor poles to boost the starting torque and efficiency of WFSMs.

Based on the above analysis, the design approaches of rotor PM HEM can be listed as 1) Combing DC field excitation and PM excitation in rotor. 2) Combing radial and axial magnetic circuits. 3) Combining two machines in axial direction. 4) Using inverter-fed AC field excitation. 5) PM-assisted wound field synchronous machine.

Each rotor PM HEM owns its own advantages and disadvantages, in terms of brushless design, torque density, mechanical structure and drive complexity. Different topologies can be utilized based on specialized requirement and cost limit in practical applications.

1.2.2 Stator PM HEMs

Stator PM machine, as a relatively new class of PM machine, has attracted much attention in literature over the past twenty years [30-31]. In stator PM machines, the PMs are usually arranged at stator side, while the rotor consists of iron core, similar with that in SRM. Stator PM machines have the merits of robust rotor structure, controllable PM field, cooling benefit as well as fault-tolerant ability, while suffer from relatively low torque density, PM utilization factor and efficiency when compared to rotor PM machines. According to the location of PM sources, the stator PM machine can be divided into three groups, namely doubly salient PM machines (DSPM) [32-33], flux switching PM machines (FSPM) [34-35] and flux reversal PM machines [36-37]. By introducing DC field coils into stator PM machines, brushless HEM topologies can be constructed. Fig. 1.11 shows two doubly-salient HEMs (HE-DSPM) [38-39], in which the PMs are arranged in stator yoke across three stator teeth, and DC field coils share the series magnetic circuit in Fig. 1.11(a), or parallel magnetic circuit in Fig. 1.11(b). The DS-HEM has the advantages of simple rotor structure and controllable PM field. However, it inherits the drawbacks of DSPMs such as asymmetry magnetic circuit, large torque ripple and low torque density.
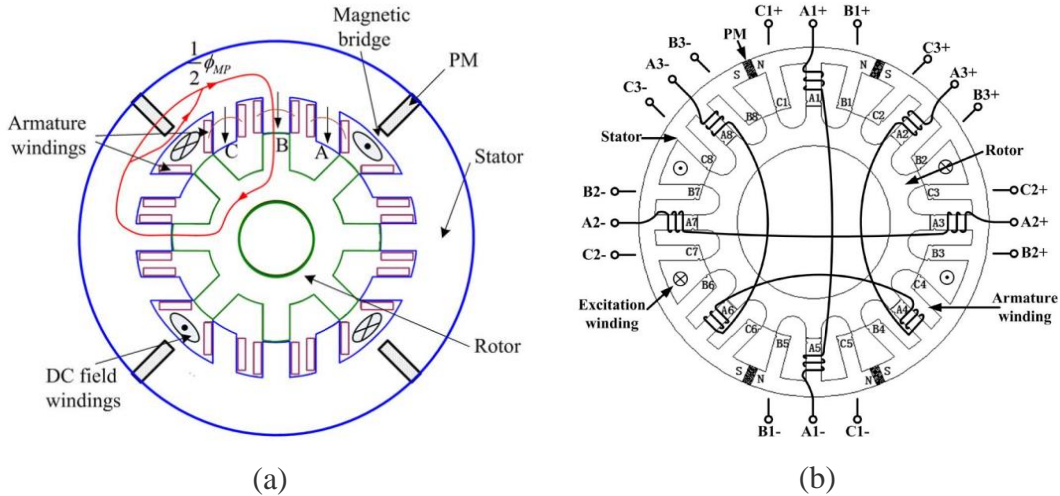
Fig. 1.11 Doubly-salient HEMs. (b) Series type [38]. (b) Parallel type [39].
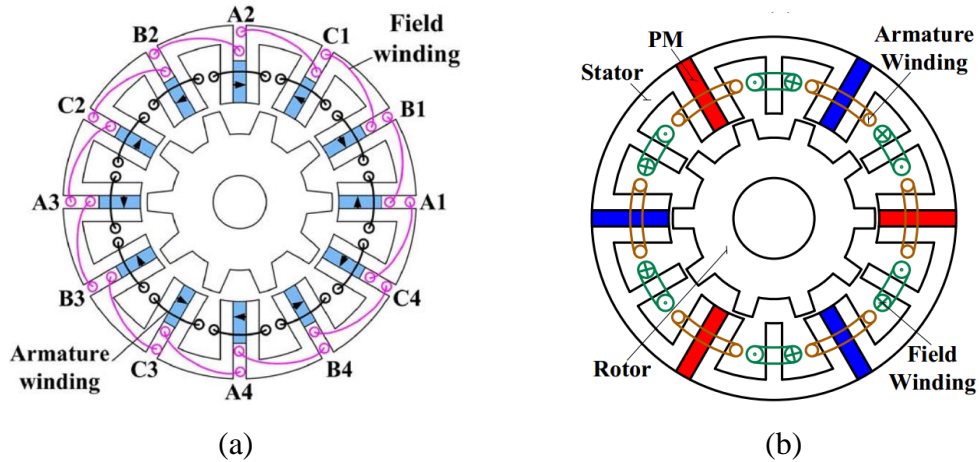
Fig. 1.12 Different HE-FSPM topologies (a) C-core type [40]. (b) E-core type [41].

In FSPM, tangentially-magnetized PMs are embedded in stator teeth to provide flux-concentrating effect and thus increase torque density, which has been widely investigated in literature. Further, the HE topologies of FSPM (HE-FSPM), including both E-core and C-core structures, as presented in Fig. 1.12, have been also proposed by replacing part of PMs by DC field coils [40-41]. HE-FSPM has the potential to achieve good torque density and controllable flux. However, the issues of PM utilization and PM demagnetization risk still exist and even amplified. Very recently, an emerging HE-FSPM with short-circuit PMs

sandwiched between different stator teeth is proposed [42-43], as shown in Fig. 1.13, which can be a potential solution for fault-tolerant power generation applications such as hybrid electric vehicles, considering its negligible no-load voltage and cogging torque.

FRPM uses alternate PMs mounted on stator teeth. Due to its inherent flux modulation effect, its torque density is good. Fig. 1.14 presents a novel topology of HE-FRPM with consequent-pole stator PMs [44-45]. In this machine, the flux linkage in a single armature coil becomes bipolar, which greatly degrades machine torque density
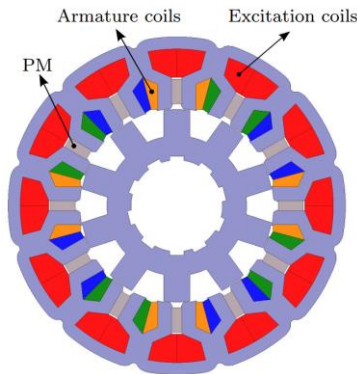
Fig. 1.13 Emerging HE-FSPM topologies with shorted-circuit PMs [42-43].
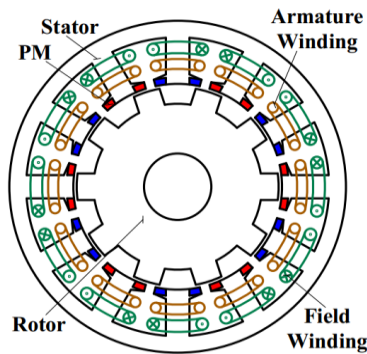
Fig. 1.14 Flux reversal HEM with consequent-pole PM structure [44-45].

In the abovementioned stator PM HEMs, a common issue is the space conflict between AC armature coils, DC field coils as well as PMs since they are all arranged at stator side, which leads to the reduction of torque density and efficiency. Therefore, stator PM HEMs

with double-stator structure are proposed in [46-47], in which the PMs and DC field windings are located at inner stator, while the AC armature winding is accommodated in outer stator. The rotor consists of iron segments only. Both series and parallel structures are investigated as shown in Fig. 1.15. This double-stator topology solves the space conflict between different excitation sources in stator PM HEMs. However, it inevitably increases the mechanical complexity as well as the machine manufacturing cost.

| (a) | (b) |
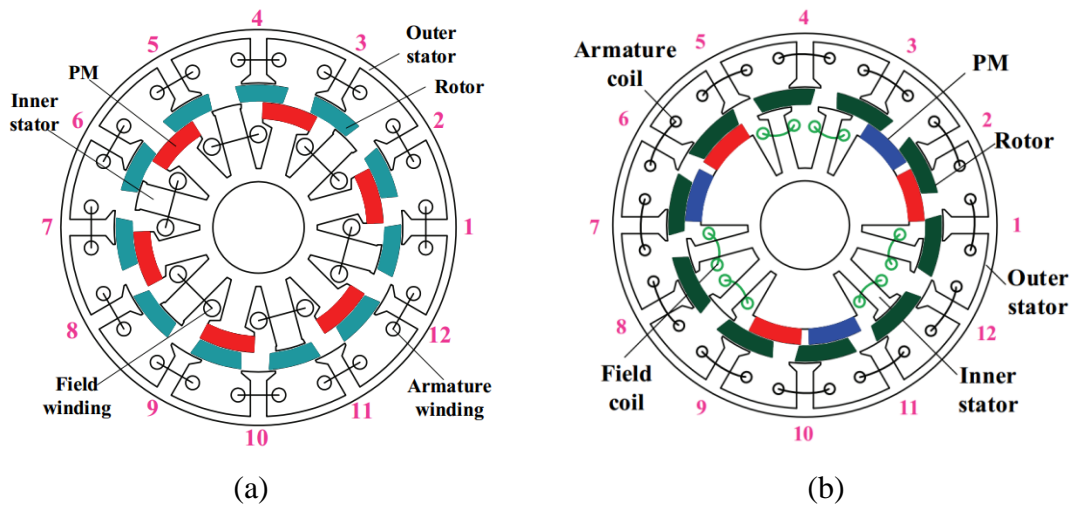
Fig. 1.15 Double-stator stator PM HEMs. (a) Series type [46]. (b) Parallel type [47].

SRM has been widely studied in literature due to its low cost, robust structure and good fault-tolerant ability [48-49]. However, the torque density of SRM is not comparable to that of traditional PM machines, due to its poor excitation ability and easy saturation feature. To improve the torque density of SRM, some PM-assisted SRMs is proposed [50-53], in which tangential PMs are introduced into stator slots, aiming to release the magnetic saturation of stator core and produce extra PM torque. As shown in Fig. 1.16, PMa-SRMs with segmented stator and segmented rotor are both investigated. It has been demonstrated that, with slot PM assistance, the torque density, efficiency and stator heat of SRM can be all improved, while the torque ripple issue still exists as well as the increased machine cost.

(a)   (b)
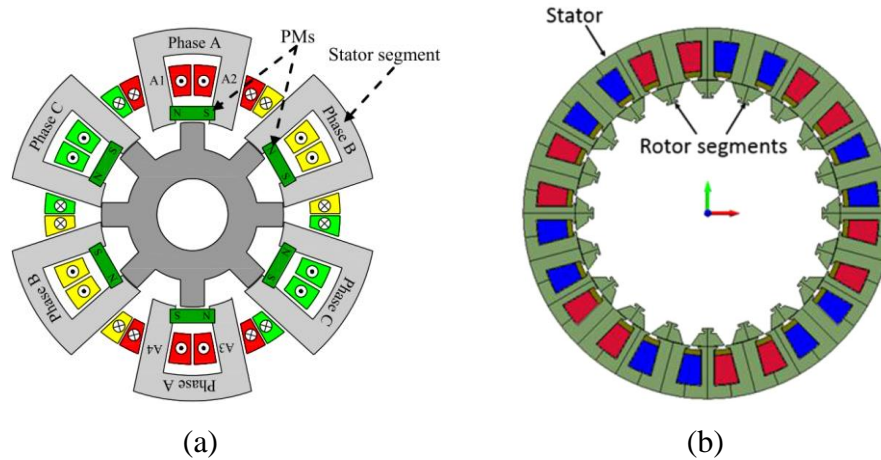
Fig. 1.16 (a) Segmented-stator PMa-SRM [50-52]. (b) Segmented-rotor PMa-SRM [53].

(a)   (b)
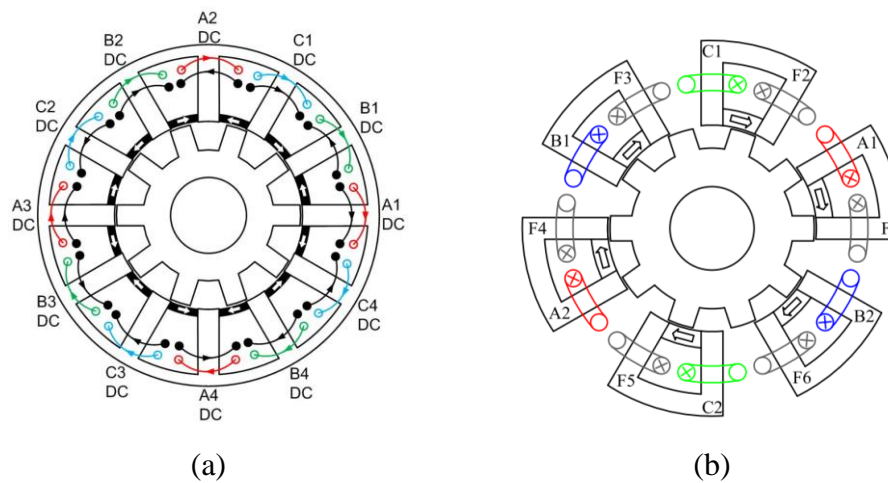
Fig. 1.17 PM-assisted variable flux reluctance machines [57-58].

Another reluctance machine design, namely variable flux reluctance machine (VFRM), which has uniformly wound AC armature coils and DC field coils in stator, becomes an emerging non-PM solution [54-56]. Compared to SRM, the main advantages of VFRM are small torque ripple and can be driven by traditional three-phase inverter. However, the torque density and efficiency of VFRM are relatively lower than those of SRM due to the introduction of extra DC field excitation. To boost the torque and efficiency performance of VFRM, tangentially-magnetized PMs are introduced into stator slots [57-58], as shown in Fig. 1.17, aiming to release magnetic saturation and produce PM torque.

1.2.3 Dual PM HEMs

Dual PM machine is an emerging topology for direct-drive applications, in which two sets of consequent-pole PMs are arranged at both stator and rotor side to achieve boosted air gap flux density and torque density [59-62]. A dual PM machine can be regarded as a combination of stator PM machine and rotor PM machine, respectively. Benefiting from the flux controllability of stator PM machine, the brushless hybrid structure, dual PM HEM can be simply constructed by introducing DC field coils in stator. Fig. 1.18(a) shows a typical dual PM HEM [63], in which two sets of PMs are mounted on stator teeth and rotor slots, respectively. The DC field coils are uniformly wound on the stator teeth to directly control the stator PM field. Good torque density and flux controllability can be both achieved in this new topology. However, the space conflict between DC coils and AC coils still exists. Besides, the DC field directly passes through the stator PMs, and thus increases the demagnetization risk and degrades the machine performance. Employing double-stator structure can release the space conflict between different excitation sources [64], as shown in Fig. 1.18(b), while its mechanical complexity and manufacturing cost are increased.

(a) (b)
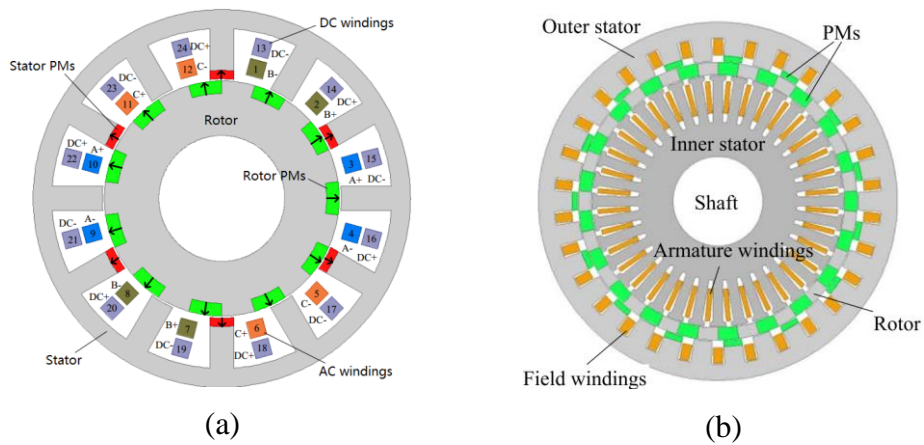
Fig. 1.18 Dual PM HEMs. (a) PMs mounted on both stator teeth and rotor [63].
(b) Double-stator structure [64].

1.3 REVIEW OF FLUX MODULATION MACHINES

The flux modulation theory was early proposed in the design of magnetics gears, which reveals that by the introduction of flux modulation poles, rich air gap harmonics can be generated and contribute to the torque boost effect. This emerging flux modulation theory breaks the design rule of traditional PM machines in which the pole pair number of stator winding and PM excitation must be same. Meanwhile, it allows more flexible configuration of excitation sources in the design of electrical machines and thus more possible slot pole combinations can be explored. Based on this flux modulation theory, a variety of new machine topologies are developed in the recent decades, including different kinds of magnetic-geared machines and Vernier machines, which can be all referred as FMMs. Compared to the traditional PM machines, FMMs have higher torque density arising from inherent magnetic gearing effect. Moreover, the cogging torque and torque ripple of FMMs are smaller than those of traditional PM machines, due to their multi-pole-pairs structure design, which makes FMMs potential for low-speed direct-drive applications.

1.3.1 Magnetic Gears and Its Integration into Machines

From a structure perspective, all the FMMs can be derived out from the coaxial magnetic gears (MG) with surface-mounted PM structure [66-69], as presented in Fig. 1.19. The MG consists of three parts, a low-speed outer PM rotor, middle modulation layer that consists of iron core segments, and a high-speed inner PM rotor. Two coaxial PM rotors have opposite rotation directions, and their rotation velocity ratio is inversely proportional to the ratio of PM pole pairs. Compared to the traditional mechanical gear box, MG adopts non-contact magnetic energy conversion, and thus has higher torque transmission ability, reduced acoustic noise, easy maintenance as well as overload protection.
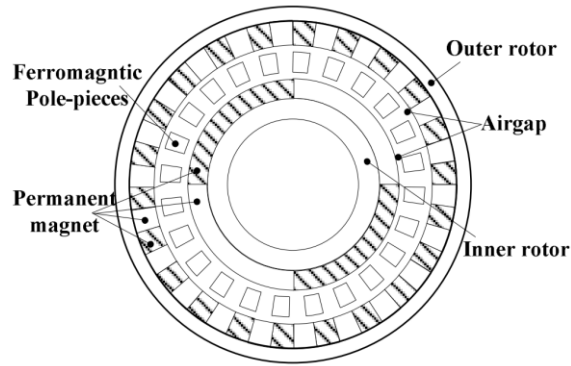
Fig. 1.19 Magnetic gear with surface mounted PMs [66-69].
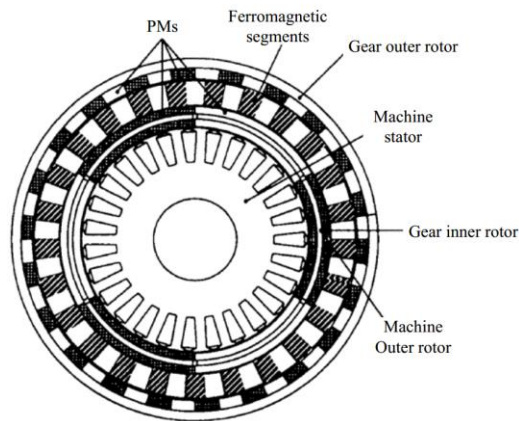
(a)
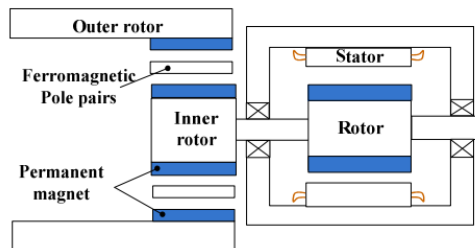
(b)

Fig. 1.20 (a) Radial MG integration [70-71]. (b) Axial MG integration [72].

By integrating the MG into traditional PM machines, the mechanical gear box can be eliminated, while maintaining the high torque transmission ability [70-72]. Fig. 1.20 shows two typical integration methods in both radial and axial directions. Compared to the axial integration, the radial integration has a more compact structure. However, it generates three air gaps, which greatly increases the manufacturing complexity and cost.

17

1.3.2 Magnetic Geared Machines

Fig. 1.21 shows a typical magnetic-geared machines (MGM) derived from MG, in which the low-speed PM rotor of MG is integrated into a machine stator with armature windings, while the modulation layer of MG becomes a low-speed rotor instead [73-74]. Compared to the traditional PM machines, this machine has higher torque density due to magnetic gearing effect. However, it has two air gaps and two mechanical ports rotating in opposite directions, making the design of bearing system very complicated.
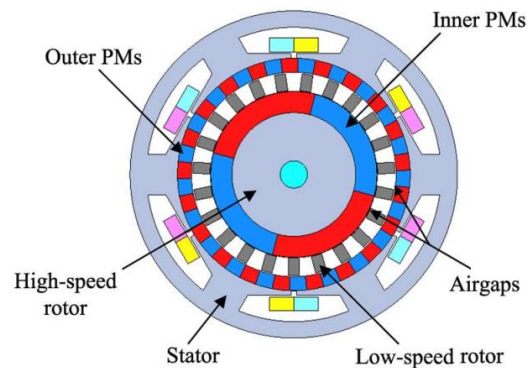
Fig. 1.21 "Pseudo" direct-drive magnetic geared PM machine [73-74].

Another simple approach to construct MGMs, is replacing the high-speed PM rotor by using rotating armature excitation [75-77]. As presented in Fig. 1.22, different MGMs with high-speed rotating armature excitation are developed, by changing the layout of PMs in the low-speed rotor, including the alternative structure, consequent-pole structure, and dual consequent-pole structure. These MGMs has two air gaps but only one mechanical output, thus are relatively easier to be manufactured. However, their torque density and power factor are lower than the above MGM with two counter-rotating mechanical ports

By replacing dual PM rotors of MG with rotating armature excitation, a novel non-PM dual-stator doubly-fed MGM is proposed [78-79], as that presented in Fig. 1.23. This MGM has two air gaps and only one mechanical port. By integrating magnetic gearing effect, this

machine can achieve higher torque density than traditional non-PM machines. However, it needs dual inverters to inject current excitation into inner outer armature windings using different operation frequency, making the control strategies relatively complicated.

(a)

(b)

(c)
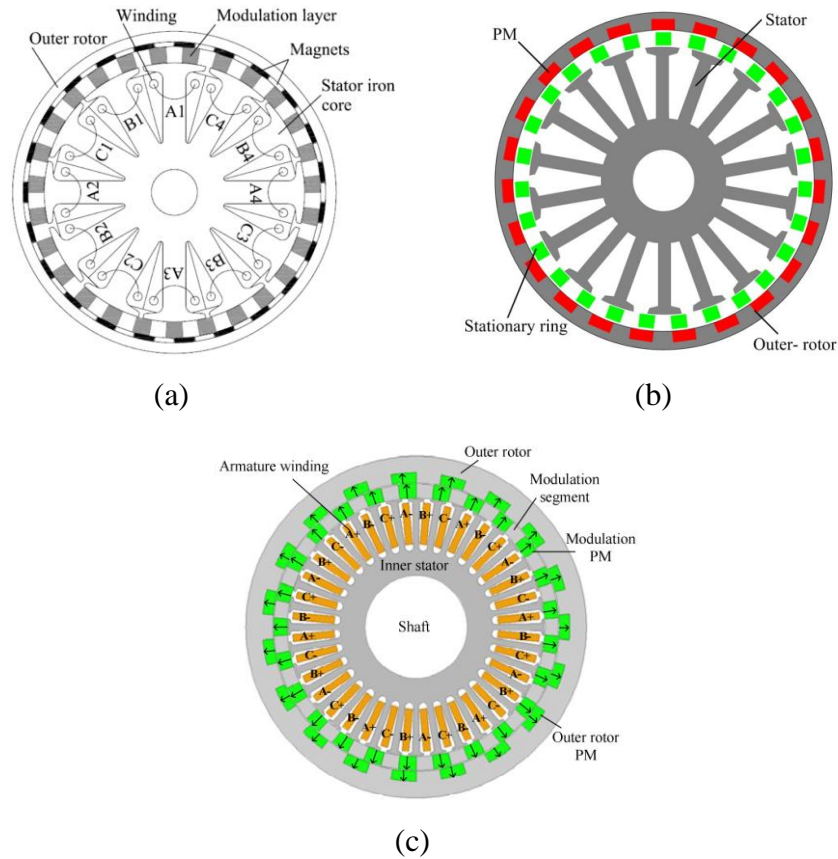
Fig. 1.22 MGMs with a single mechanical output. (a) Alternate PM structure [75]. (b) Consequent-pole PM structure [76]. (c) Dual-consequent-pole structure [77].
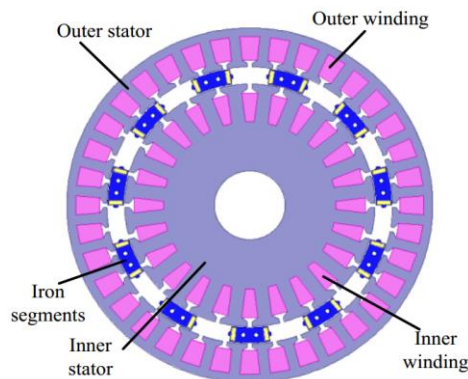
Fig. 1.23 Doubly-fed double-stator MGM [78-79].

1.3.3 Vernier Machines

Fig. 1.24 presents a typical Vernier machine (VM) with surface mounted PM structure. VM integrates magnetic gearing effect by stator teeth modulation of PM field, thus has higher torque density than that of traditional PM machines [80-85]. However, its power factor is relatively low due to large leakage flux and thus reduced air gap flux density. Moreover, the rich harmonics leads to increased core saturation and core loss. Therefore, the efficiency of VMs is not comparable to that of traditional PM machines.
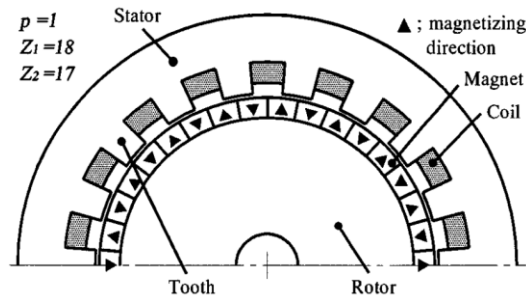
Fig. 1.24 Surface-mounted PM Vernier machine [80-85].

(a)   (b)
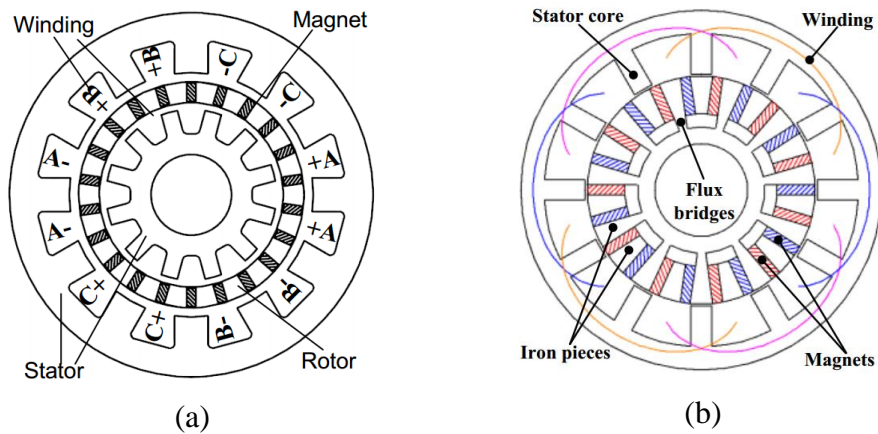
Fig. 1.25 Spoke-type PM Vernier machine. (a) Interlaced double-stator structure [86-87]. (b) Alternating flux barrier structure [88-89].

Due to the special slot pole combinations in VMs and associated long armature magnetic circuit, using spoke PM structures in VMs could reduce the magnetizing inductance and

degrade torque density. Fig.1.25 presents two improved topologies of VMs with spoke PM structures. One is the interlaced-double-stator structure, as presented in Fig. 1.25(a), which provides an effective flux return path for the modulated PM field, thus boosts its air gap flux density, torque density and power factor [86-87]. Another simplified solution is using alternating flux bridges, as shown in Fig. 1.25(b), which can reduce the loop reluctance of modulated PM field and thus boost the torque density and power factor [88-89].

1.4 RESEARCH CHALLENGES AND OBJECTIVES

The HEMs have been studied for decades, including topology innovation and analytical modeling. By reviewing the history of HEMs, some challenges can be concluded as

1) For rotor PM HEMs. The existing methods to realize brushless structure by using radial and axial combined magnetic circuit, usually leads to increased mechanical complexity and torque density sacrifice due to redundant air gap.

2) For stator PM HEMs. Due to the poor PM utilization factor, the torque density and efficiency of stator PM machines are not comparable to rotor PM machines. This drawback is inherited or even amplified in stator PM HEMs, especially considering the space conflict between DC field coils and AC armature coils in stator PM HEMs.

3) For dual PM HEMs. The PMs in stator usually contribute to a small part of torque generation compared to rotor PMs. Hence, in dual PM HEMs, the flux regulation ability by controlling stator PM field is limited, especially considering demagnetization risk.

How to increase torque density of HEMs while maintaining good flux regulation ability, is the main research topic of this thesis. Inspired by the development of FMMs, a new topology by integrating flux modulation effect in new HEMs, namely FMHEMs, has the potential to achieve both good torque density and flux regulation ability.

The research objectives of this thesis mainly consist of the following parts as

1) Propose novel FMHEM topologies.

2) Establish analytical methods for FMHEMs.

3) Electromagnetic design and analysis of FMHEMs.

4) Make prototypes and perform experimental tests.

5) Apply and evaluate FMHEMs.

1.5 THESIS OUTLINE

This thesis consists of six chapters. The first chapter introduces the research background and gives a literature review. The last chapter draws some conclusions and provides future works. The rest chapters are organized as follows.

In chapter two, a new hybrid excitation Vernier reluctance machine is proposed, in which consequent-pole PMs are artificially introduced into stator slots to generate flux modulation effect and interact redundant armature harmonics, so that the machine torque density is greatly improved compared to its non-PM counterpart. Moreover, the introduced consequent-pole slot PMs share a parallel magnetic circuit with armature excitation, thus providing bidirectional flux regulation ability as well as demagnetization withstand ability. The machine configuration and operation principle are introduced. The harmonics analysis is performed based on flux modulation theory. Both finite element simulation and protype tests are conducted to verify the proposed topology.

In chapter three, considering the space conflict between AC armature coils and DC field coils in the proposed hybrid excitation Vernier reluctance machine, the zero-sequence current control is applied to generate DC current component in AC armature coils, which can function as virtual DC field coils at design stage and contributes to improve torque

density and efficiency. The optimal injection ratio of zero-sequence current is evaluated, considering the influence of both dimension parameters and electrical parameters. The finite element analysis and protype tests verify the effectiveness of this improved topology.

In chapter four, a new hybrid excitation dual-PM Vernier machine is proposed. This machine adopts dual consequent-pole PMs arranged in both stator slots and rotor slots, thus contributes to boosted air gap flux density and increased torque density. Moreover, DC field excitation is introduced to provide an extra flux weakening variable by controlling saturation level of stator core, which can be coordinated with the traditional d-axis vector flux weakening to further extend the torque speed range. The machine structure and operation principle are introduced. Its performance is evaluated by both finite element simulation and protype experiments.

In chapter five, to address the issue of the parasitic stator DC saturation effect introduced by DC field excitation, an improved topology, namely relieving-DC-saturation hybrid excitation dual-PM Vernier machine is proposed. Especially, a constant flux bias is introduced by tangentially-magnetized stator slots PMs, thus to cancel the DC flux component excited by DC field excitation. In this way, the DC saturation effect in stator core is eliminated, which improves machine torque density and flux regulation ability.

CHAPTER 2. PROPOSED HYBRID EXCITATION VERNIER RELUCTANCE MACHINE WITH IMPROVED UTILIZATION OF REDUNDANT WINDING HARMOINCS

2.1 INTRODUCTION

Due to their wide speed range and robust rotor structure, reluctance machines have been widely studied in literature, including the switched reluctance machine (SRM), DC-excited doubly salient machine (DE-DSM), DC-excited flux switching machine (DE-FSM) and variable flux reluctance machine (VFRM) [90-93]. For SRM, it relies on the variation of self-inductance to produce reluctance torque and each phase can only work for half of electrical period, leading to severe torque ripple and mechanical vibration [94]. DE-DSM utilizes the multi-inductance between armature winding and field winding to produce effective torque, but its torque ripple is still unacceptable due to unipolar flux feature [95]. For DE-FSM and VFRM, their working principles are both based on flux modulation effect, and thus can be classified as DC-excited Vernier reluctance machines (DC-VRM) [96]. DC-VRM can obtain smooth torque when driven by sinusoidal armature current. However, DC-VRM still suffers from low torque density due to its poor excitation ability.

This chapter proposes a novel hybrid excitation Vernier reluctance machine (HE-VRM) with improved torque density and extended torque speed range. The key is based on the flux modulation effect to introduce an auxiliary stator-slot PM excitation and thus utilize the redundant armature winding harmonics to boost torque density. Meanwhile, this stator-slot PM excitation share a parallel flux path with DC field excitation and interact with different armature harmonics, thus providing bidirectional field regulation.

2.2 MACHINE STRUCTURE

The structure of the proposed HE-VRM is presented in Fig. 2.1, in which a 24-slot stator and a 22-pole rotor are adopted. The rotor consists of only iron cores. Two independent excitation sources are arranged at the stator side, one is the DC field excitation and the other is the stator-slot PM excitation. The pole pairs of two excitation sources are different with each other. All those DC-field coils are identically and alternately wounded on stator teeth to constitute a 12-pole-pair uniform exciting field. The PMs are mounted on the slot open of stator, and they are all radially magnetized in the same outward direction as denoted by arrows in Fig. 2.1. The armature winding uses a single-layer concentrated connection as presented in Fig. 2.2, which owns the advantages such as simplified wire wrapping, eliminated insulation and relatively higher space factor.
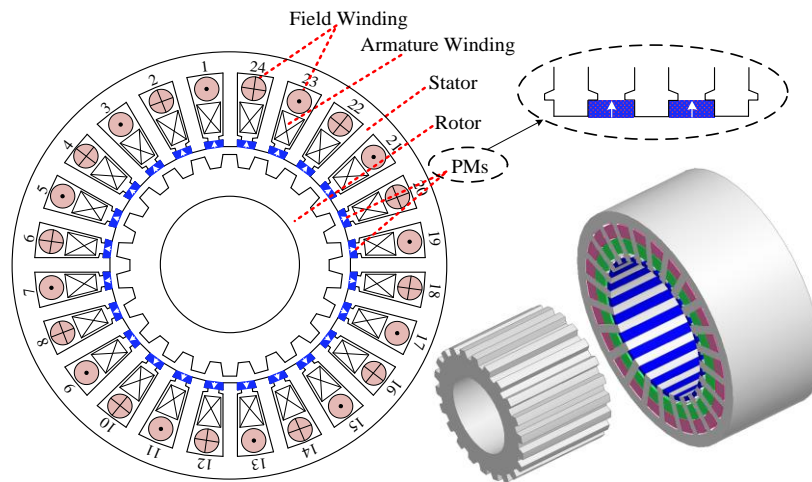
Fig. 2.1 Configuration of the proposed HE-VRM.
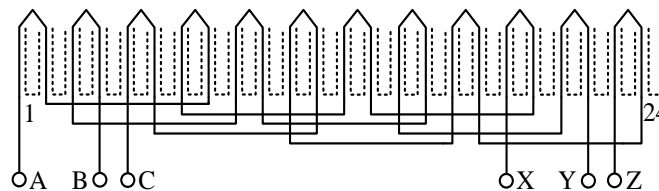
Fig. 2.2 Connection of armature winding.

The advantages of the proposed HE-VRM are summarized as

1) With such a passive rotor, the proposed machine still maintains a mechanical robustness, which can reduce the risk of PM damage, compared with rotor-excited machines.

2) Benefiting from the concentrated configuration, the winding ends for both field excitation and armature excitation are short, which can accordingly reduce copper loss, increase the machine axial length and boost its power density.

3) Compared with the existing DC-excited reluctance machines, the proposed new hybrid excitation design has distinctly improved torque density, due to slot PM assistance.

4) The DC field excitation and stator-slot PM excitation have different pole pair numbers and parallel magnetic circuits. Two excitation sources interact with different winding harmonics. Therefore, little demagnetization risk exists for stator-slot PMs during field regulation. Bidirectional flux regulation can be obtained by reversing the field excitation, which can lead to an extended speed range.

5) De-excitation operation can be achieved when this machine works as a generator under power device short-circuit situation. This can avoid a huge strike of short-circuit current in electrical system, which is extremely important for some safety-critical applications.

2.3 OPERATION PRINCIPLE

To clearly illustrate its operation principle, HE-VRM can be artificially split into two individual machines, one is a DC-excited reluctance machine and the other is the stator-slot-PM-excited reluctance machine. As shown in Fig. 2.3(a), the effective magnetic circuit for DC field excitation starts from a wounded stator tooth, then passes through the stator yoke and adjacent two stator teeth, and finally returns through the rotor yoke. Further, the effective magnetic circuit for PM excitation is given in Fig. 2.3(b). It starts from the stator

tooth, passing through a longer stator yoke part, then comes back through the rotor yoke. The flux distribution for two excitation sources are quite different due to their difference in pole pair numbers. In addition, the length of PM magnetic circuit is relatively longer than that of field excitation, especially in stator and rotor yoke. However, the effective flux of two excitation sources can still couple in armature winding as highlighted by circles, which means a hybrid magnetic circuit with both PM excitation and DC field excitation is established. Meanwhile, the DC field magnetic circuit doesn't pass through stator-slot-PMs, thus better flux regulation ability and less demagnetization risk can be achieved.

<div align="center">(a)   (b)</div>
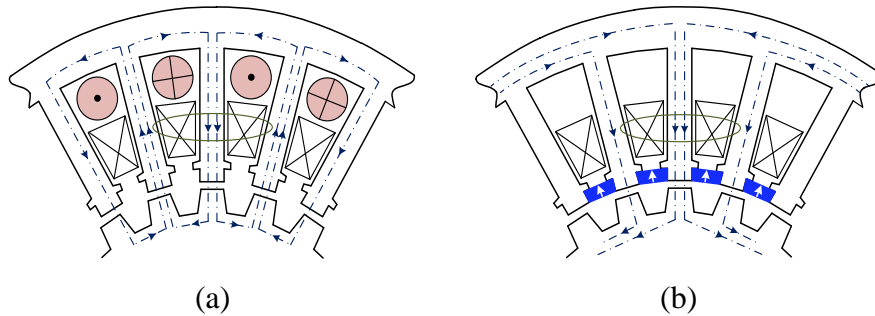
Fig. 2.3 Separation of the proposed topology and schematic magnetic circuits.
(a) DC-excited VRM. (b) Stator-slot-PM-excited VRM.

2.4 HARMONICS ANALYSIS

To more clearly reveal the torque generation mechanism of DC field excitation and stator-slot PM excitation, respectively, a simplified analysis is used in this part in which their mutual influence under saturation situation is not considered.

When only the DC field excitation is applied, considering all these field coils are symmetrically distributed in all stator slots, the magnetomotive force (MMF) excited by the field excitation can be regarded as a square wave with air-gap circumferential angle, its Fourier series expansion can be expressed as

$$F_{DC}(\theta) = \sum_{n=1,3,5...}^{\infty} \frac{4F_{dc}}{n\pi} \sin(np_{dc}\frac{\theta_s}{2})\cos(np_{dc}\theta) \qquad (2.1)$$

where F_{dc} is the MMF amplitude of a single DC coil, p_{dc} is the pole pair number of field excitation, θ_s is the arc of stator teeth.

The rotor adopts a salient-pole configuration, and thus the permeance at rotor side is not uniform, which can be also expanded as a Fourier series

$$\Lambda_r(\theta,t) = \Lambda_{r0} + \sum_{k=1}^{\infty} \frac{\Lambda_{r1}}{k\pi} \sin(kp_r\frac{\theta_r}{2})\cos\left[kp_r(\theta-\theta_0-\omega_r t)\right] \qquad (2.2)$$

where Λ_{r0} and Λ_{r1} are the average value and peak to peak value of the rotor permeance, respectively. p_r is the number of rotor poles, θ_r is the arc of rotor poles. ω_r is the rotor mechanical angular velocity. θ_0 is the initial mechanical angle.

Further, the air gap flux density excited by the DC field excitation can be obtained by multiplying (2.1) and (2.2)

$$\begin{cases} B_{DC}(\theta,t) = F_{DC}(\theta)\Lambda_r(\theta,t) = \dfrac{4F_{dc}\Lambda_{r0}}{\pi}\sum_{n=1,3,5}^{\infty}C_{n1}\cos(np_{dc}\theta) \\[2mm] + \dfrac{2F_{dc}\Lambda_{r1}}{\pi^2}\sum_{n=1,3,5}^{\infty}\sum_{k=1}^{\infty}C_{n1}C_{k1}\left[\cos(\varepsilon_1)+\cos(\varepsilon_2)\right] \\[2mm] C_{n1} = \dfrac{1}{n}\sin(np_{dc}\dfrac{\theta_s}{2}), C_{k1}=\dfrac{1}{k}\sin(kp_r\dfrac{\theta_r}{2}) \\[2mm] \varepsilon_1 = \left(np_{dc}-kp_r\right)\left[\theta+\dfrac{kp_r}{np_{dc}-kp_r}(\theta_0+\omega_r t)\right] \\[2mm] \varepsilon_2 = \left(np_{dc}+kp_r\right)\left[\theta-\dfrac{kp_r}{np_{dc}+kp_r}(\theta_0+\omega_r t)\right] \end{cases} \qquad (2.3)$$

It can be found the DC excited field has both stationary and rotating components. Further, their spatial orders, amplitudes, rotational velocities are summarized in Table 2.1. The stationary air gap harmonic components in Group I are generated by the original DC field excitation, while those rotating harmonic components in Group II and Group III are generated by the flux modulation effect of rotor slots.

TABLE 2.1 Excited Harmonics Components by the DC Field Excitation

Group	Spatial order	Amplitude	Rotating velocity
I	np_{dc}	$\dfrac{4F_{dc}\Lambda_{r0}}{\pi}C_{n1}$	0
II	$\|np_{dc}-kp_r\|$	$\dfrac{2F_{dc}\Lambda_{r1}}{\pi^2}C_{n1}C_{k1}$	$\dfrac{-kp_r\omega_r}{\|np_{dc}-kp_r\|}$
III	$np_{dc}+kp_r$	$\dfrac{2F_{dc}\Lambda_{r1}}{\pi^2}C_{n1}C_{k1}$	$\dfrac{kp_r\omega_r}{np_{dc}+kp_r}$

Remarks: The negative indication means opposite direction with rotor rotation

Then, assuming the only active excitation source is the stator-slot PM excitation, all the PMs are symmetrically arranged in the stator slots, each PM and its adjacent stator teeth constitutes a pair of magnetic poles. The corresponding MMF produced by stator-slot PM excitation can be written as

$$F_{PMs}(\theta) = \sum_{n=1,3,5...}^{\infty} \frac{4F_{PMs}}{n\pi}\sin(np_{PMs}\frac{\theta_s}{2})\cos(np_{PMs}\theta) \tag{2.4}$$

where F_{PMs} refers to the MMF amplitude of a single PM pole. p_{PMs} refers to the pole pair number of stator-slot PM excitation.

The permeance at rotor side for the stator-slot PM excitation is the same as in (2.2), therefore, the excited field can be derived by multiplying (2.2) and (2.4).

$$\begin{cases} B_{PMs}(\theta,t) = F_{PMs}(\theta)\Lambda_r(\theta,t) = \dfrac{4F_{PMs}\Lambda_{r0}}{\pi}\sum_{n=1,3,5}^{\infty}C_{n2}\sin(np_{PMs}\theta) + \\[2mm] \dfrac{2F_{PMs}\Lambda_{r1}}{\pi^2}\sum_{n=1,3,5}^{\infty}\sum_{k=1,3,5}^{\infty}C_{n2}C_{k1}\left[\cos(\varepsilon_3)+\cos(\varepsilon_4)\right] \\[2mm] C_{n2} = \dfrac{1}{n}\sin(np_{PMs}\dfrac{\theta_s}{2}) \\[2mm] \varepsilon_3 = \left(np_{PMs}-kp_r\right)\left[\theta+\dfrac{kp_r}{np_{PMs}-kp_r}(\theta_0+\omega_r t)\right] \\[2mm] \varepsilon_4 = \left(np_{PMs}+kp_r\right)\left[\theta-\dfrac{kp_r}{np_{PMs}+kp_r}(\theta_0+\omega_r t)\right] \end{cases} \tag{2.5}$$

TABLE 2.2 Excited Harmonics Components by the Stator-Slot PM Excitation

Group	Spatial order	Amplitude	Rotating velocity
I	np_{PMs}	$\dfrac{4F_{PMs}\Lambda_{r0}}{\pi}C_{n1}$	0
II	$\lvert np_{PMs}- kp_r \rvert$	$\dfrac{2F_{PMs}\Lambda_{r1}}{\pi^2}C_{n2}C_{k1}$	$\dfrac{-kp_r\omega_r}{\lvert np_{PMs}- kp_r \rvert}$
III	$np_{PMs}+ kp_r$	$\dfrac{2F_{PMs}\Lambda_{r1}}{\pi^2}C_{n2}C_{k1}$	$\dfrac{kp_r\omega_r}{np_{PMs}+kp_r}$

The excited field by stator-slot PMs also have stationary and rotating components, which are summarized in Table 2.2. Further, from (2.3) and (2.5), it can be found the pole pair number difference between the DC field excitation and stator-slot PM excitation results in different flux modulation effects with different spatial orders and rotational velocities of harmonic components. Based on the machine structure shown in Fig. 2.1, the pole pair numbers of these two excitation sources are governed by

$$\begin{cases} p_{dc}= \dfrac{N_s}{2} \\ p_{PMs} = N_s \end{cases} \tag{2.6}$$

where N_s refers to the number of stator teeth.

Lastly, the air gap field excited by the single-layer armature excitation is studied. The single-phase MMF distribution of a 24-slot single-layer non-overlapping armature winding can be separately expressed as

$$\begin{cases} F_A(\theta) = \displaystyle\sum_{n=1,3,5...}^{\infty} \frac{4N_c i_a}{n\pi}\sin(n\frac{N_s\theta_s}{24})\cos(n\frac{N_s}{12}\theta) \\ F_B(\theta) = \displaystyle\sum_{n=1,3,5...}^{\infty} \frac{4N_c i_b}{n\pi}\sin(n\frac{N_s\theta_s}{24})\cos\left[n\frac{N_s}{12}(\theta-\frac{2\pi}{3})\right] \\ F_C(\theta) = \displaystyle\sum_{n=1,3,5...}^{\infty} \frac{4N_c i_c}{n\pi}\sin(n\frac{N_s\theta_s}{24})\cos\left[n\frac{N_s}{12}(\theta-\frac{4\pi}{3})\right] \end{cases} \tag{2.7}$$

where N_c is the armature coil turns. i_a, i_b and i_c are the peak value of armature current.

Suppose a balanced three-phase sinusoidal current are applied for the armature terminal. The synthetic armature MMF can be deduced by spatially overlapping three single-phase excitations, which can be presented as

$$F_{ABC}(\theta,t) = \sum_{h=1,5,7...}^{\infty} \frac{6N_c I_{ac}}{n\pi} \sin(\frac{hN_s\theta_s}{24})\cos\left[\frac{hN_s}{12}(\theta-\omega_e t-\theta_e)\right] \tag{2.8}$$

The excited field by armature excitation is modulated twice by stator teeth and rotor slots, respectively. Considering the open-slot design at stator side, the stator permeance becomes not uniform, which can be expanded as

$$\Lambda_s(\theta) = \Lambda_{s0} + \sum_{k=1}^{\infty} \frac{\Lambda_{s1}}{k\pi} \sin(kN_s \frac{\theta_s}{2})\cos(kN_s\theta) \tag{2.9}$$

where Λ_{s0} refers to the average value of the stator permeance, and Λ_{s1} refers to its peak to peak value, respectively.

Correspondingly, the air gap harmonics components excited by the armature excitation can be obtained by multiplying (2.2), (2.8) and (2.9).

$$\begin{cases} B_{ABC}(\theta,t) = F_{ABC}(\theta,t)\Lambda_s(\theta)\Lambda_r(\theta,t) = \\ \dfrac{6N_c I_{ac}\Lambda_{s0}\Lambda_{r0}}{\pi} \displaystyle\sum_{h=1,5,7}^{\infty} C_h \cos\left[\dfrac{hN_s}{12}(\theta-\omega_e t-\theta_e)\right] + \\ \dfrac{3N_c I_{ac}\Lambda_{s1}}{\pi^2} \displaystyle\sum_{h=1,5,7}^{\infty}\sum_{k_2=1}^{\infty} C_h C_{k2}\cos(\dfrac{hN_s}{12}\pm k_2 N_s)\left[\theta - \dfrac{hN_s}{hN_s \pm 12k_2 N_s}(\omega_e t+\theta_e)\right] + \\ \dfrac{3N_c I_{ac}\Lambda_{r1}}{\pi^2} \displaystyle\sum_{n=1,5,7}^{\infty}\sum_{k_1=1}^{\infty} C_h C_{k1}\cos(\dfrac{hN_s}{12}\pm k_1 p_r)\left[\theta - \dfrac{hN_s}{hN_s \pm 12k_1 p_r}(\omega_e t+\theta_e)\right] + \\ \dfrac{6N_c I_{ac}\Lambda_{s1}\Lambda_{r1}}{\pi^3} \displaystyle\sum_{n=1,5,7}^{\infty}\sum_{k_1=1}^{\infty}\sum_{k_2=1}^{\infty} C_h C_{k1}C_{k2}\cos(\dfrac{hN_s}{12}\pm k_1 N_s \pm k_2 p_r)\left[\theta - \dfrac{hN_s(\omega_e t+\theta_e)}{hN_s \pm 12k_1 N_s \pm k_2 p_r}\right] \\ C_h = \dfrac{1}{h}\sin(h\dfrac{N_s}{24}\theta_s), \omega_e = N_{PMr}\omega_r \end{cases} \tag{2.10}$$

The whole excited field by armature excitation is concluded in Table 2.3, in which four fundamental harmonic groups are listed. The harmonics in Group I are excited by armature

excitation without any modulation effect. The Group II is the component modulated by the stator teeth. The Group III is the component modulated by the rotor slots. The Group IV is the component modulated by both the stator teeth and rotor slots. One can see, various harmonic components are generated by this single-layer concentrated armature excitation, which gives a precondition for a single armature winding to simultaneously interact with two excitation sources with different pole pair numbers.

TABLE 2.3 Excited Harmonics Components by the Armature Excitation

Group	Spatial order	Amplitude	Rotating velocity
I	$\dfrac{hN_s}{12}$	$\dfrac{6N_c I_{ac} \Lambda_{s0} \Lambda_{r0}}{\pi} C_h$	$\dfrac{hN_s}{12}\omega_e$
II	$\left\|\dfrac{hN_s}{12} \pm k_2 N_s\right\|$	$\dfrac{3N_c I_{ac} \Lambda_{s1}}{\pi^2} C_h C_{k2}$	$\dfrac{hN_s}{hN_s \pm 12k_2 N_s}\omega_e$
III	$\left\|\dfrac{hN_s}{12} \pm k_1 p_r\right\|$	$\dfrac{3N_c I_{ac} \Lambda_{r1}}{\pi^2} C_h C_{k1}$	$\dfrac{hN_s}{hN_s \pm 12k_1 p_r}\omega_e$
IV	$\left\|\dfrac{hN_s}{12} \pm k_2 N_s \pm k_1 p_r\right\|$	$\dfrac{3N_c I_{ac} \Lambda_{r1}\Lambda_{s1}}{2\pi^2} C_h C_{k1} C_{k2}$	$\dfrac{hN_s\omega_e}{hN_s \pm 12k_2 N_s \pm 12k_1 p_r}$

To produce effective electromagnetic torque, the harmonic components excited by this armature winding and excitation sources should have the same spatial order and rotating velocity. As for the 24-slot 22-pole HE-VRM, when $h=1, n=1, k=1$, the harmonic components in the group I generated by the armature excitation is synchronous with the group II generated by the stator-slot PM excitation. When $h=5, n=1, k=1$, the group I is synchronous with the harmonic group II generated by the DC field excitation. Similarly, the harmonic group II produced by the armature excitation are synchronous with group I excited by the stator-slot PMs as well as group I generated by the DC field excitation.

In general, rich armature harmonics can effectively interact with two different excitation sources, thus the proposed HE-VRM can be designed with good torque density.

2.5 DRIVE SYSTEM

The drive system for the proposed machine is presented in Fig. 2.4, which mainly consists of an input power source, a three-phase inverter for the armature terminal as well as an H-bridge converter for the field terminal. Besides, it should be pointed out, the field excitation should be bi-directionally regulated to satisfy different torque and speed requirements under different working conditions. Therefore, the asymmetric half-bridge converter used for most DC-excited machines is not suitable due to its unidirectional characteristic, and instead, a bi-directional H-bridge converter is used. The proposed design has two electrical ports with their control strategies illustrated by schematic signal flows. The vector control for the armature terminal is the same as that for most AC synchronous machines. As for the DC field terminal, a PWM control is adopted to provide a required field excitation according to the reference value at different speeds.
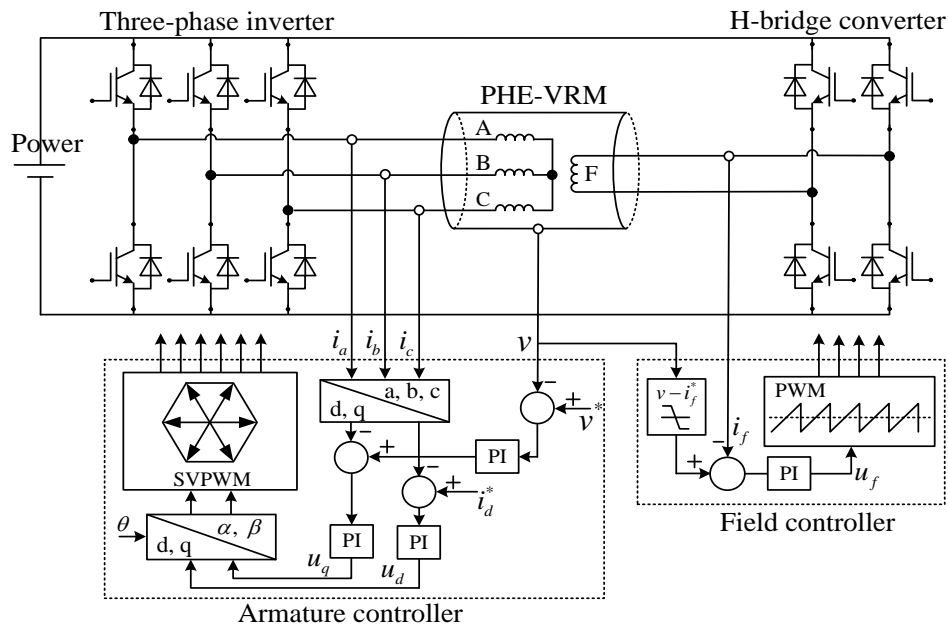
Fig. 2.4 Drive system of the proposed HE-VRM.
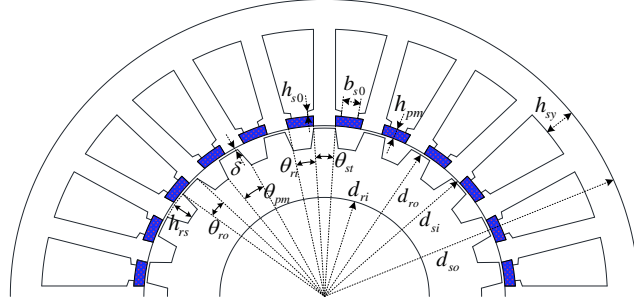
Fig. 2.5 Dimension parameters of the proposed HE-VRM.

TABLE 2.4 General dimension parameters of the proposed HE-VRM

Symbol	Parameter	Unit	Value
d_{so}	Outer diameter of stator	mm	120
d_{si}	Inner diameter of stator	mm	69
d_{ro}	Outer diameter of rotor	mm	68
d_{ri}	Inner diameter of rotor	mm	20
δ	Air gap length	mm	0.5
l	Stack length	mm	50
h_{sy}	Height of stator yoke	mm	5
θ_{st}	Arc of the stator teeth	°	7
θ_{pm}	Arc of the stator-slot-PMs	°	2
h_{pm}	Height of stator-slot-PMs	mm	8
θ_{ro}	Outer arc of the rotor poles	°	7
θ_{ri}	Inner arc of the rotor poles	°	10
h_{r0}	Height of rotor slots	mm	3.5
b_{s0}	Open width of stator slots	mm	3.2
h_{s0}	Height of stator shoes	mm	1

TABLE 2.5 Major Materials and Specifications

PMs		Steels	
Material	NdFeB35	Material	MG19_24
Remanence	1.2 T	Saturated point	1.8 T
Coercive force	915 kA/m	Mass density	7650 kg/m^3

2.6 FINITE ELEMENT ANALYSIS

2.6.1 Magnetic Field Distribution

To verify the feasibility of the proposed machine, a finite element model is built by using Maxwell. The dimension parameters are labeled in Fig. 2.5, with initial design values listed in Table 2.4. The materials are given in Table 2.5, along with major characteristics.

Firstly, the excited air gap flux density with each individual excitation source is calculated and presented in Fig. 2.6, with its corresponding harmonics distribution obtained by FFT analysis. When the stator-slot PMs are removed and only the DC field excitation is applied, the no load air gap field is given in Fig. 2.6(a) and the dominant harmonic components indicated are the 10th, 12th and 34th one. Further, with only stator-slot PMs active, the excited air gap field is plotted in Fig. 2.6(b) and the dominant harmonic components are the 2th, 24th and 46th one. Finally, with only armature excitation injected, corresponding excited field is plotted in Fig. 2.6(c). Due to single-layer non-overlapping connection, rich harmonics are produced by armature excitation. The calculated harmonics distribution agrees with the previous theoretical predication, as indicated Fig. 2.6, which verifies the validity of previous MMF-permeance analytical model.

To clearly describe the interaction between the armature field and two excitation sources, the frequency spectrum of armature harmonics is divided into five non-overlapping regions. It can be found, the armature field interacts with DC field excitation within the region II and IV, while it interacts with the stator-slot PM excitation within the region I, III and V. There is no overlap in the working regions between DC field and PM excitation due to their difference in pole pair numbers, which verifies that the introduced stator-slot PM excitation can effectively utilize the redundant winding harmonics to boost the torque density.
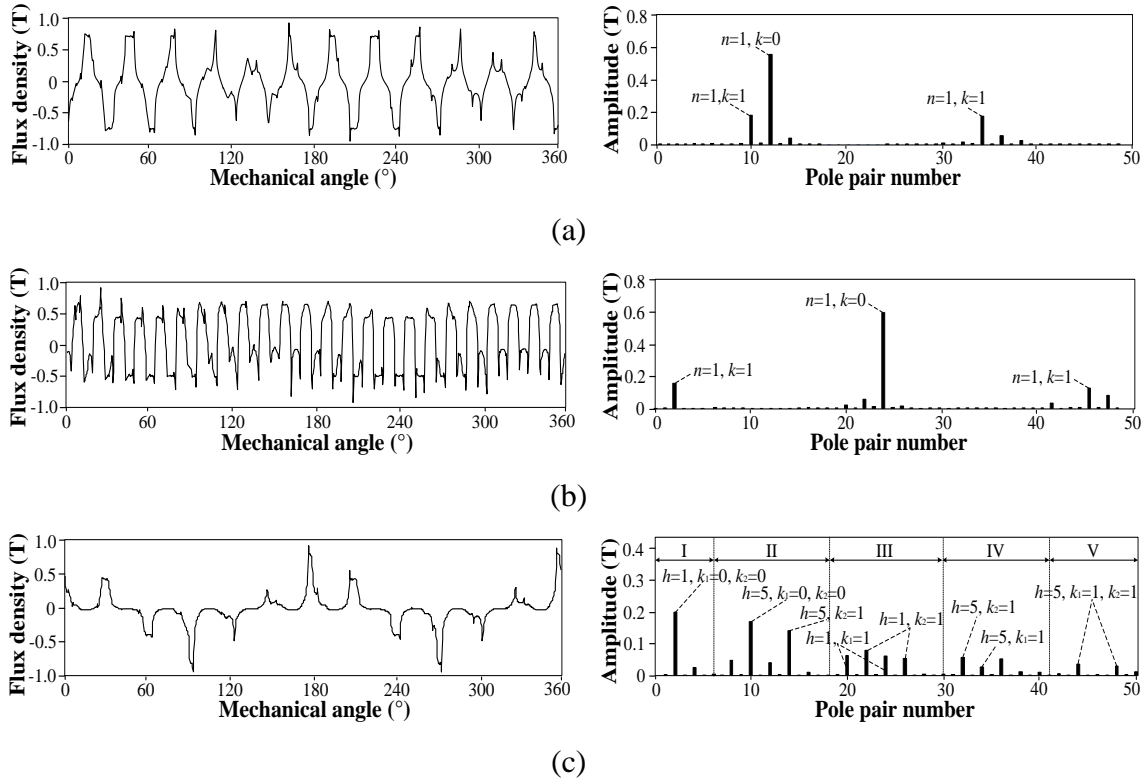
Fig. 2.6 Air gap flux density with individual excitation source. (a) Only DC field excitation. (b) Only stator-slot PM excitation. (c) Only armature excitation.
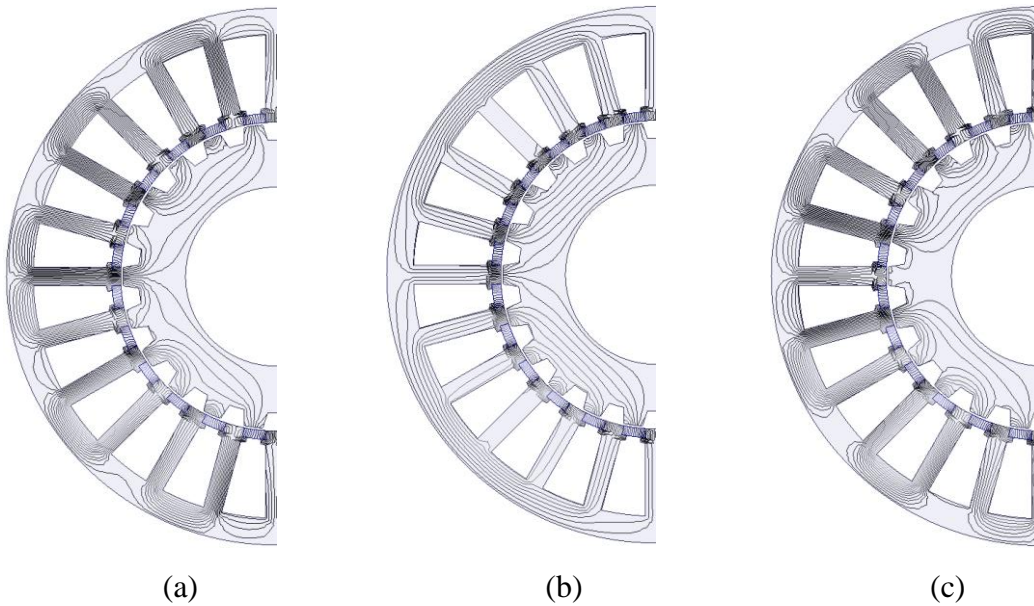
Fig. 2.7 Flux distribution. (a) Full level with 240A positive field MMF. (b) Half level with 0 field MMF. (c) Weak level with 240A negative field MMF.
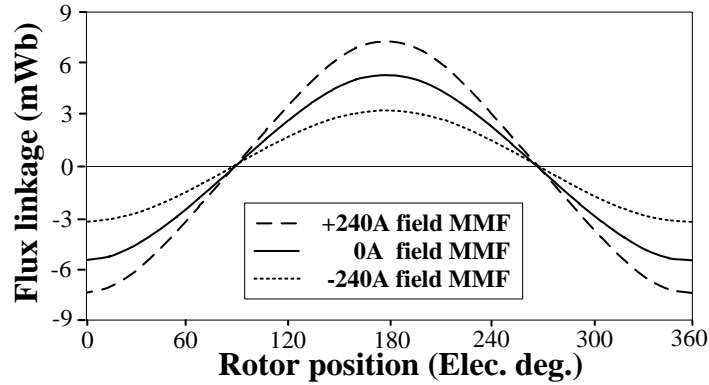
Fig. 2.8 Variation of no-load phase flux linkage.

2.6.2 Flux Regulation Ability

Further, the magnetic field distribution at different excitation status is plotted in Fig. 2.7. Due to the pole pair number difference of two excitation sources, the flux distribution at the stator side presents a significant shape change when a bidirectional field excitation is injected. Both flux enhancing and flux weakening operation can be realized by reversing the field current, which leads to a wide flux regulation range as plotted in Fig. 2.8.

2.7 DESIGN OPTIMIZATION AND COMPARATIVE STUDY

To fully evaluate the effectiveness of the proposed topology, a comparative study is carried out. Four different topologies are taken into consideration. One is the DC-excited design without any PMs as shown in Fig. 2.9(a), namely Model I. Fig. 2.9(b) shows an existing hybrid-excited design, in which PMs are placed on the stator teeth and share the same magnetic circuit with DC excitation, namely Model II. Another counterpart is presented in Fig. 2.9(c), in which PMs are arranged in slot opens and has the same magnetization mode as that in Model II, namely Model III. The last one in Fig. 2.9 (d) is the proposed machine in this paper, one can see, consequent-pole PMs are mounted on slot

opens which are all radially magnetized, namely Model IV. For a fair comparison, these four different models should be simultaneously optimized with the same outer dimension, stack length and air gap length as listed in Table 2.4. The maximum average torque is regarded as the optimization objective, when the torque ripple ratio less than 10% is regarded as the restricted condition. Four models are evaluated at the same rated point.
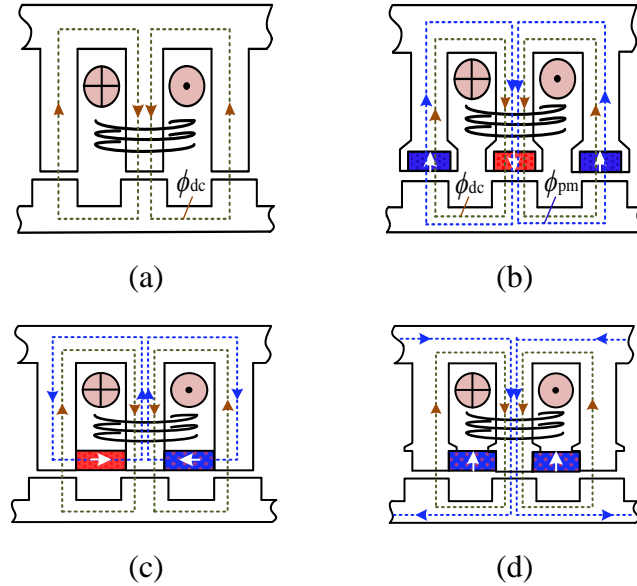
Fig. 2.9 Different topologies for comparison. (a) Model I, Only DC winding. (b) Model II, DC winding and stator-teeth PMs. (c) Model III, DC winding and tangentially-magnetized stator-slot PMs. (d) Model IV, proposed HE-VRM.

TABLE 2.6 Dimension Parameters to be Optimized for Four Models

Parameters	Model	Lower limit	Upper limit
Height of stator yoke (mm)	I, II, III, IV	4.5	9.5
Arc of the stator teeth (°)	I, II, III, IV	6.4	8.4
Outer arc of the rotor poles (°)	I, II, III, IV	6.4	8.4
Inner arc of the rotor poles (°)	I, II, III, IV	6.8	10.8
Height of rotor slots (mm)	I, II, III, IV	3.2	4.2
Height of stator-teeth PMs (mm)	II	0.2	2.2
Height of stator-slot PMs(mm)	III, IV	0.2	2.2

38
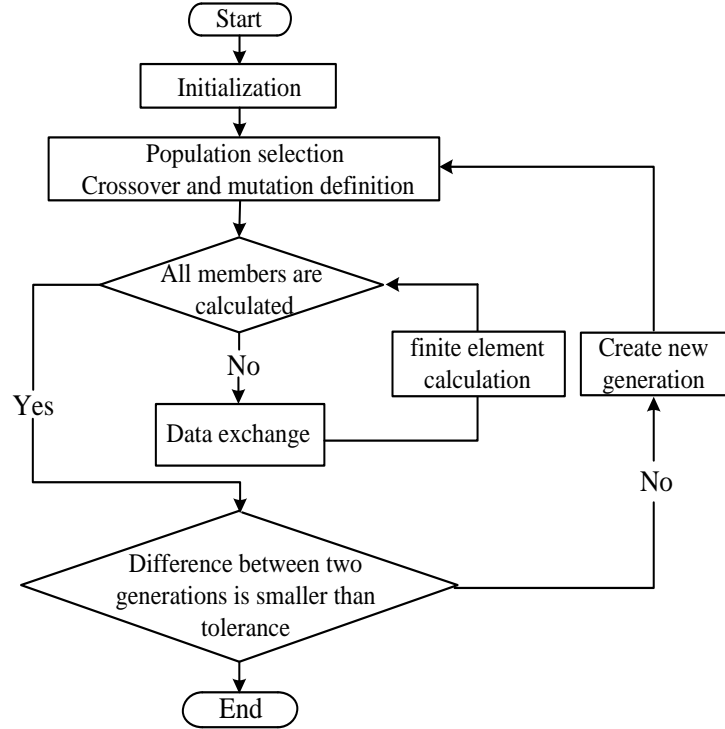
Fig. 2.10 Flowchart of the FEA and GA coupled optimization.

TABLE 2.7 Final Dimension Parameters for Four Models after Optimization

Parameters	Model I	Model II	Model III	Model IV
Height of stator yoke (mm)	4.7	5.4	5.2	6.5
Arc of the stator teeth (°)	6.5	6.7	6.6	7.1
Outer arc of the rotor poles (°)	6.5	6.6	6.9	6.8
Inner arc of the rotor poles (°)	6.9	6.8	7.1	6.9
Height of rotor slots (mm)	3.7	3.9	4.1	4.1
Height of stator-teeth PMs (mm)	-	1.3	-	-
Height of stator-slot PMs (mm)	-	-	2.1	1.8

2.7.1 Selection of Optimization Parameters

Different PM arrangements lead to different magnetic field distribution and saturation. Accordingly, influence of the same dimension parameters will also be much different in

these four models. For the proposed Model IV, some important dimension parameters are selected to be optimized based on the following considerations. The height of stator yoke part has an important influence on the loop flux reluctance especially for a relatively longer PM magnetic circuit caused by flux modulation effect. The arc of stator teeth is obviously an important design parameter. On the one hand, it defines the section area of flux flow, and on the other hand, it is inversely proportional to the stator-slot PM volume. The height of PM also needs to be optimized since it not only determines its MMF, but also affects the magnetic saturation. As for the rotor design, three parameters are taken into optimization, the outer arc of the rotor poles, the inner arc of the rotor poles and the depth of rotor slots. Their influence on torque performance is similar with that in other reluctance machines. Based on the above analysis, all the dimension parameters selected to be optimized in these four models are presented in Table 2.6, with optimization boundaries determined based on their spatial and electromagnetic constraints.

2.7.2 GA and FEA Combined Optimization

An intelligent optimization algorithm is used in this process, namely genetic algorithm (GA). GA has three operation factors, namely the reproduction, crossover and mutation. Reproduction generates the adaptive individual survival, when crossover and mutation are responsible for expanding the searching scope. In such a way, GA can find the optimal design by imitating natural selection effect. Further, a combined optimization between the Maxwell (a commercial finite element software) and GA is used to optimize the dimension parameters. To realize a combined analysis, an intelligent script is established for data communication between Maxwell and GA. The whole flow chart is given in Fig. 2.10. This method can reduce the time consumption since no manual adjustment is needed.

The optimization is performed with following considerations: a population of 25 elements, the maximum generation number of 30, crossover probability of 0.9 and mutation probability of 0.1, respectively. Fig. 2.11 presents the optimized elements of last two generations of four models, from which the final dimension parameters are selected and listed in Table 2.7. One can find, the proposed topology presents a much higher average torque than the other three existing designs, which can directly prove the advantage of this novel topology. Besides, the steady torque waveforms of the proposed design before and after optimization, are plotted in Fig. 2.12. With this combined optimization method, the machine torque performance can be effectively improved.
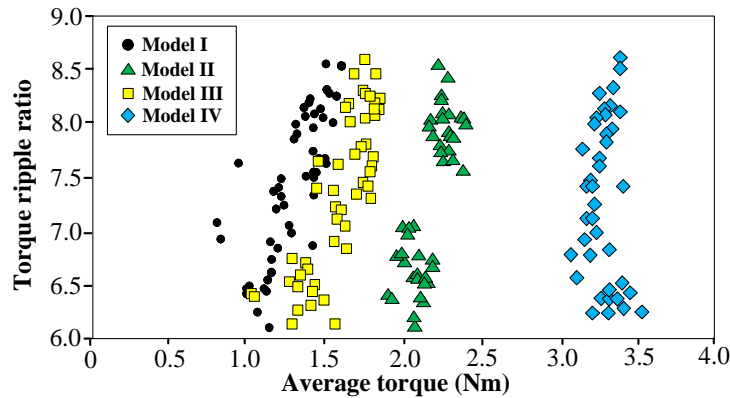
Fig. 2.11 Rated torque performance of last two generations.
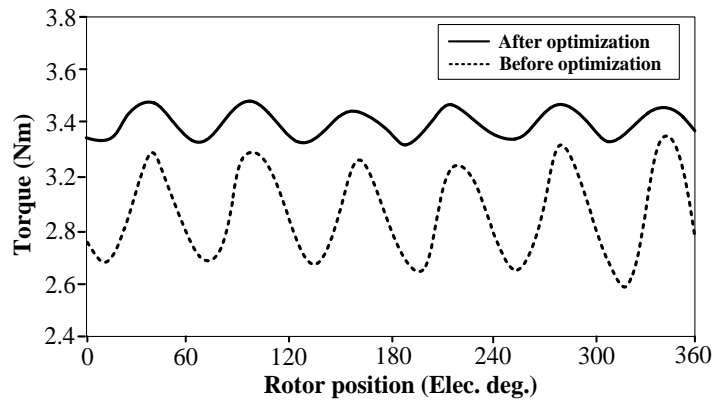
Fig. 2.12 Rated torque waveform of Model IV with and without optimization.

2.7.3 Comparative Study

After the design optimization, a comparative study is further performed between four Models in terms of overload capacity, core loss, PM loss and efficiency. Fig. 2.13 shows the output torque of four models with different total copper loss, including field copper loss and armature copper loss. In general, with the increase of copper loss, the output torque increases to a certain value until saturation occurs. One can find, the point of saturation is almost the same for Model I, II, and IV, and meanwhile, the proposed topology always presents a larger torque density than other models. The reason is that the proposed topology can effectively enhance the utilization factor of the redundant armature harmonics to boost torque density, while in other existing topologies, those redundant winding harmonics make little contribution to torque generation but still leads to a saturation. Meanwhile, it should be pointed out the Model III presents a better overload ability due to its anti-saturation feature, which means it is more suitable for large-current applications.
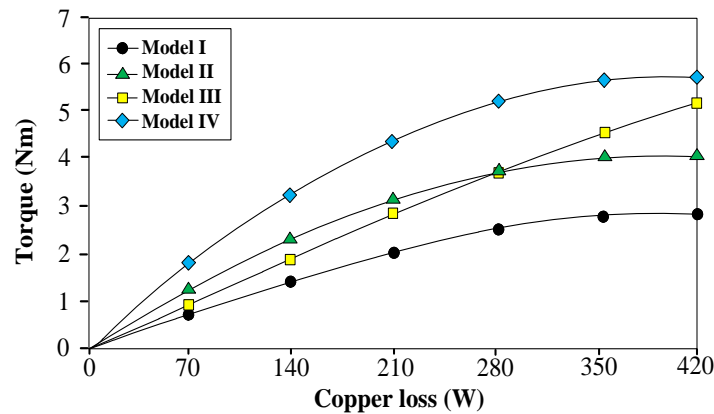
Fig. 2.13 Output torque with different copper loss.

Further, the core loss and PM eddy current loss at different speed is evaluated and plotted in Fig. 2.14 and Fig. 2.15, respectively. The proposed design has larger core loss and PM eddy current loss due to a relatively larger local leakage flux. However, the influence level

of core loss and PM eddy current loss is smaller than copper loss since the machine is designed within low speed region. Moreover, the efficiency at different speed is calculated in Fig. 2.16. One can find that the proposed solution can achieve higher overall efficiency compared to other three models, which is in line with its improvement in torque density.
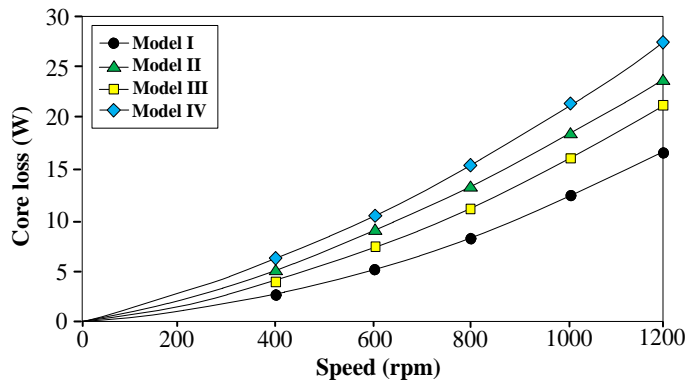
Fig. 2.14 Core loss at different speed, with copper loss 140W.
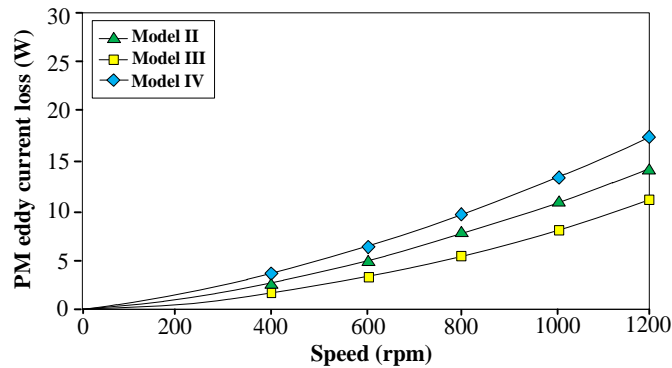
Fig. 2.15 PM eddy current loss at different speed, with copper loss 140W.
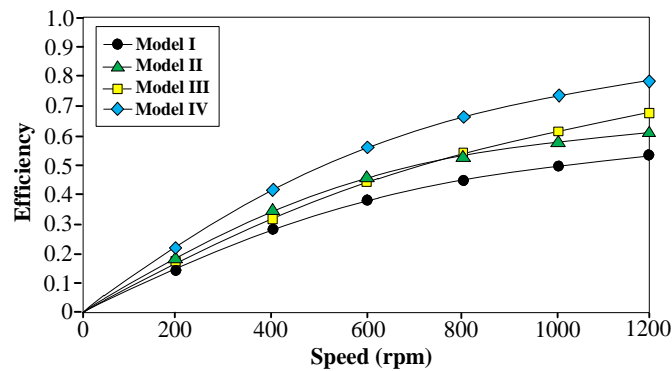
Fig. 2.16 Efficiency at different speed, with copper loss 140W.

TABLE 2.8 Inductance and Power Factor of Four Models at Rated Point

Parameters	Model I	Model II	Model III	Model IV
Inductance (mH)	1.2	0.6	1.1	1.2
Power factor	0.45	0.71	0.47	0.68

Finally, the self-inductance and power factor (PF) at rated working point are calculated and presented in Table 2.8. Model II owns the best PF performance due to a relatively weak armature reaction. The proposed design with slot PMs owns almost the same self-inductance compared with non-PM topology since slot PMs will not change armature magnetic circuit, but an improved PF can be still obtained in the proposed solution due to enhanced flux density. However, the PF of four Models is generally poor than that of conventional PM machines, which should be considered for improvement.

2.8 OTHER DESIGN CONSIDERATIONS

2.8.1 Mechanical Support for Slot PMs

In the proposed design, all the PMs are arranged in the stator slots, which is quite different from traditional design. Therefore, extra mechanical consideration is needed to avoid potential PM movement during a continuous rotational motion. In this chapter, additional pole shoes are integrated into the stator teeth to house slot PMs. With this design technique, the stator-slot PMs can be well mounted and fixed. Meanwhile, the influence of this design on the electromagnetic performance should be evaluated. Two main parameters are considered, the height of stator shoes and its open width as denoted in Fig 2.17. The height of stator shoes should be small to minimize the reduction of the winding window area and it is fixed at 1mm in this paper. Then, the influence of open width on machine torque performance is analyzed in Fig. 2.18. One can see, this extra pole shoes generally

provides a positive effect on the torque density and ripple performance, which is mainly due to the reduction of PM reluctance. Therefore, this mechanical design technique is proved to be an effective approach to achieve both PM support and enhanced torque performance in the proposed machine.
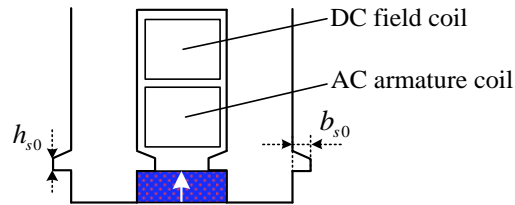
Fig. 2.17 Model of stator slot with extra pole shoes to house PMs.
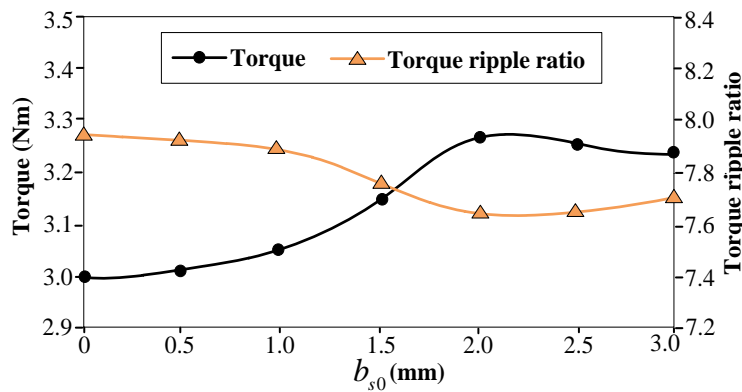
Fig. 2.18 Influence of extra pole shoes.

2.8.2 Slot Area Ratio

The design procedure for hybrid-excited machine is usually different from traditional PM machines due to the existence of extra field terminal. Meanwhile, toque density, efficiency and speed range all need to be considered. In the proposed hybrid topology, one key parameter which should be clearly defined is the slot area ratio between the field coil, armature coil and PM. Firstly, without considering PMs, the influence of slot area ratio between field coil and armature coil is given in Fig. 2.19. When the slot area ratio equals

to one, the torque density and efficiency excited by DC and armature excitation reach the maximum value. Further, the influence of slot PMs is evaluated and plotted in Fig. 2.20. On one side, with the increasing of slot PMs, the torque density increases until saturation occurs. On the other side, the speed range, which is defined as the ratio between maximum speed and base speed, will decrease with the boosting of remanent PM voltage.
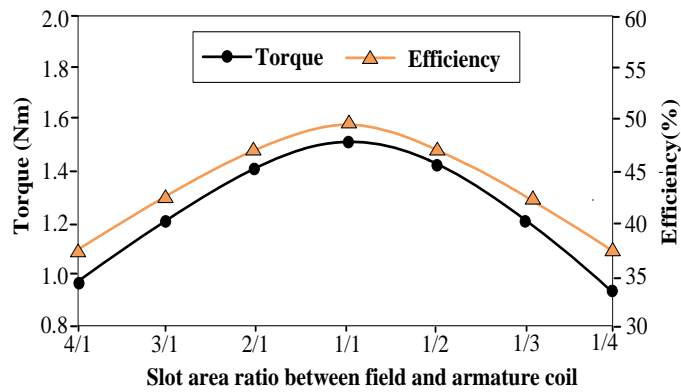
Fig.2.19 Influence of slot area ratio between field and armature coil without PMs.
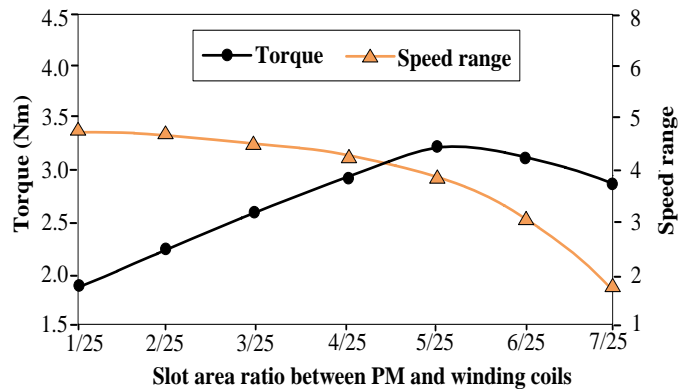
Fig.2.20 Influence of slot area ratio between PM and winding coils.
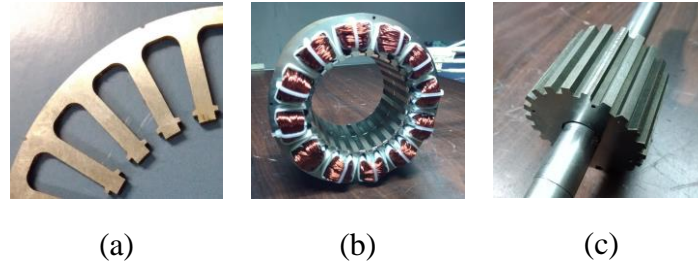
Fig. 2.21 Protype details. (a) Stator lamination. (b) Stator assembly. (c) Rotor assembly.
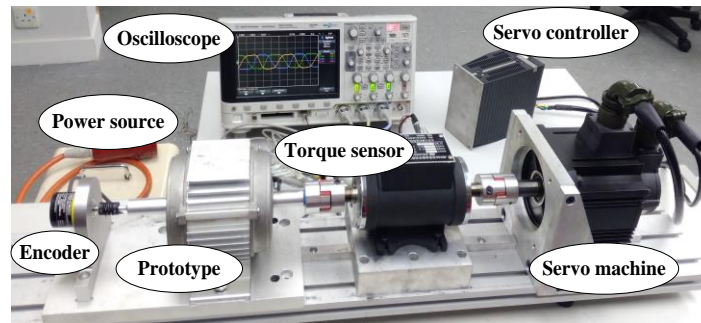
Fig. 2.22 Experimental platform based on the assembled prototype.

2.9 EXPERIMENTAL VERIFICATION

To verify the feasibility of the proposed machine, a prototype is manufactured and tested. Fig. 2.21 (a) presents the extra stator pole shoes designed for slot PM mechanical support. Fig. 2.21(b) and Fig. 2.21(c) presents the whole stator and rotor component, respectively. Further, a test bed is established based on assembled prototype as shown in Fig. 2.22.

The no load back EMF is measured and presented in Fig. 2.23, at 1000rpm without DC field excitation. One can see, the tested back EMF basically agrees with the finite element predication, although its amplitude is a little smaller which is mainly due to the fabrication tolerance such as an inconsistent magnetization of PMs. Further, the amplitude of back EMF with different field current is collected and plotted in Fig. 2.24. It can be found, by injecting a bidirectional DC field excitation, the amplitude of back EMF can be effectively enhanced or weakened as predicated by finite element analysis.
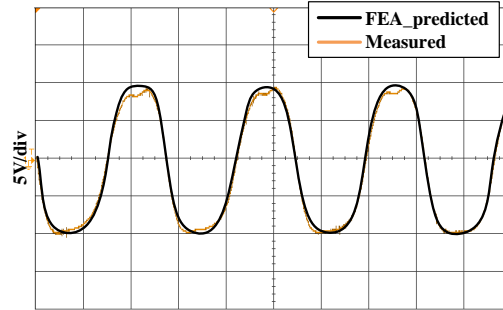
Fig. 2.23 Back EMF without field excitation, at speed 1000 rpm.
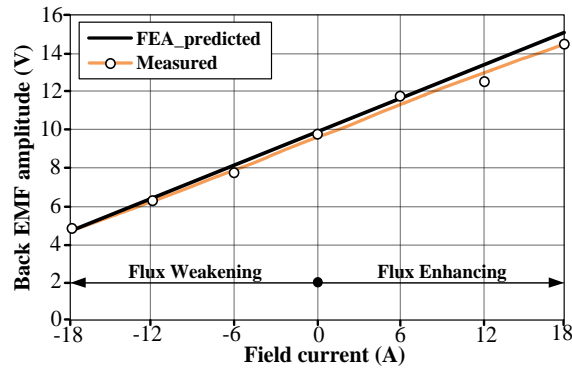
Fig. 2.24 Flux regulation capacity.
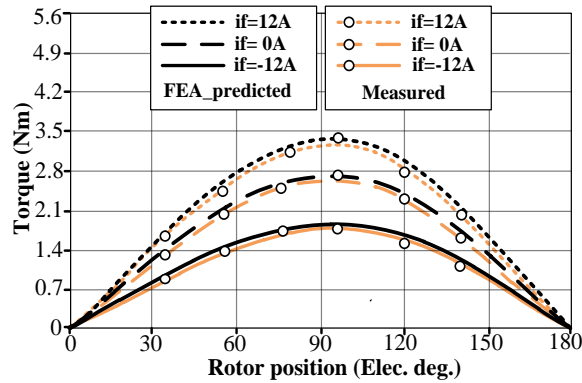
Fig. 2.25 Torque against the electrical angle with 12A armature current.

The torque-angle curve is presented in Fig. 2.25, by injecting constant DC current into the armature winding and fixing the rotor at different positions. It can be seen the output torque can be smoothly regulated with different field excitation. Certain reluctance torque can be observed, which makes the best vector control angle not located at 90°. The dynamic torque performance with different current excitation is also tested as shown in Fig. 2.26.
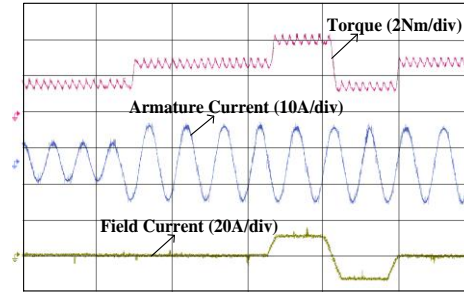
Fig. 2.26 Dynamic performance with different armature and field excitation.
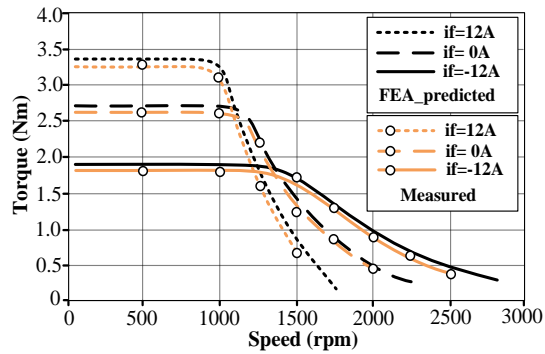
Fig. 2.27 Torque speed curves with different DC field excitation.
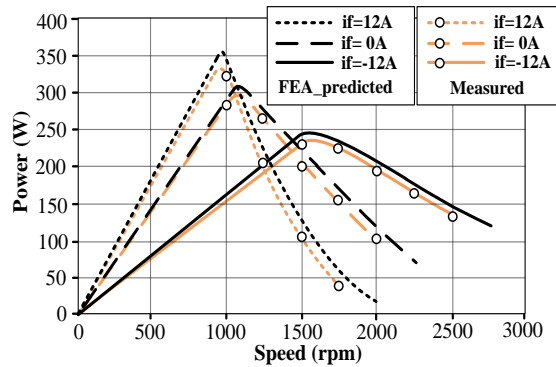
Fig. 2.28 Power speed curves with different DC field excitation.

Lastly, the torque-speed curves and power-speed curves with respect to different field excitation are presented in Fig. 2.27 and Fig. 2.28, respectively, under the limit of 80V DC bus voltage. It can be found the positive field excitation leads to an enhanced torque and power in the low-speed region, while the negative field excitation provides a higher torque and power in the high-speed region. Therefore, by adjusting field excitation at different speeds, acceptable torque and power density can be also obtained in wide speed range.

49

2.10 CONCLUSION

This chapter proposes a novel parallel hybrid excitation Vernier reluctance machine with merits of improved torque density and bidirectional flux regulation ability, which provides a potential solution for electric vehicle propulsion. The key is based on the flux modulation principle to introduce consequent-pole slot PMs and utilize redundant air gap harmonics of a single-layer concentrated armature winding, thus to boost torque density. Two excitation sources with different pole pair numbers are effectively coupled with parallel magnetic circuit. The machine structure, operation principle and harmonics analysis are introduced, along with its electromagnetic performance evaluated by finite element analysis. Besides, a design optimization and comparative study is performed between the proposed topology and existing counterparts in terms of their torque density, overload ability, core loss, eddy current loss and efficiency, which proves the progress of torque density improvement of the proposed topology. Some design guidelines for this new topology are also provided, including the mechanical support for PMs and slot area ratio between the DC field coil, AC armature coil and PMs. A prototype is manufactured, and relevant tested results agree well with finite element predictions, which verifies the effectiveness of this new solution. However, it should be pointed out, in the proposed topology, the auxiliary rare-earth slot PMs will inevitably increase cost burden, which needs to be improved, and for instance, a ferrite-magnet-assisted solution may be an alternative solution.

CHAPTER 3. PROPOSRED HYBRID EXCITATION VERNIER RELUCTANCE MACHINE WITH ENHANCED ZERO SEQUENCE CURRENT INJECTION

3.1 INTRODUCTION

In Chapter 2, a new parallel hybrid excitation Vernier reluctance machine (HE-VRM) is proposed, which utilizes both DC wound source and slot PM source to achieve enhanced torque density. However, the space conflict between DC coils and AC coils still exists in the proposed topology. This leads to the reduction of torque density and efficiency.

Inspired by the integrated design of AC and DC windings based on zero-sequence current control, as reported in [97-101], this chapter proposes an improved topology of HE-VRM by integrating AC and DC windings. This improved machine utilizes zero-sequence current to function as the DC field excitation and establish a parallel magnetic field with the slot PM source. In this way, enhanced torque performance and flexible flux control can be achieved by adjusting zero-sequence current excitation.

3.2 MACHINE STRUCTURE

Fig. 3.1 presents the configuration of the improved HE-VRM with integrated AC and DC windings. Compared to the topology in Chapter 2, the slot pole combination, rotor structure, PM magnetization and arrangement all keep the same. The only difference is involved in the winding arrangement as shown in Fig. 3.2. In this topology, the integrated AC and DC winding are split into two sub three-phase groups, which are then fed by dual inverters with connected neutral point as shown in Fig. 3.3, thus to simultaneously function as DC field winding and AC armature winding.
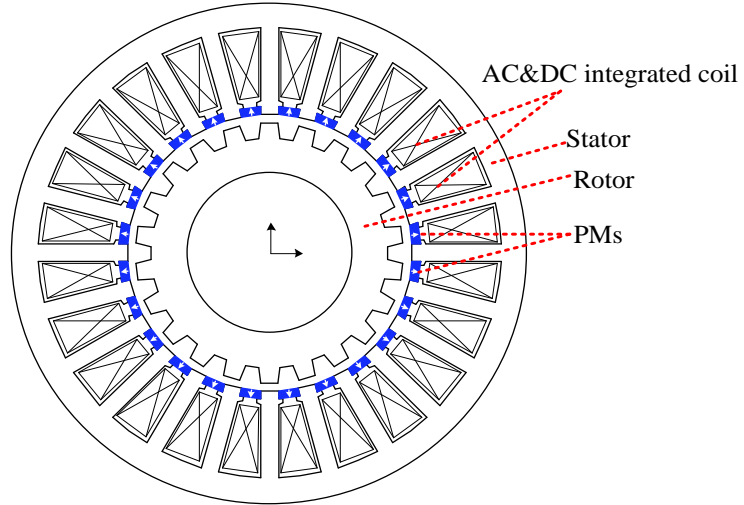
Fig. 3.1 Structure of the proposed VRM with integrated AC and DC coils.
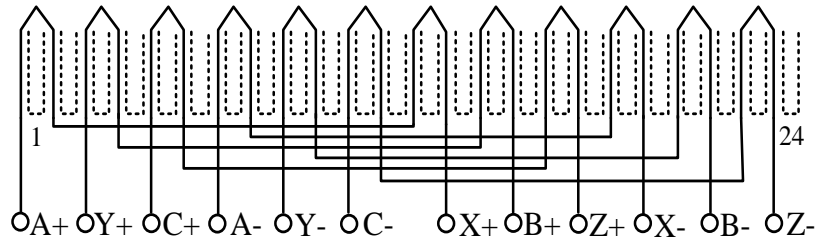
Fig. 3.2 Connection of integrated AC and DC winding.
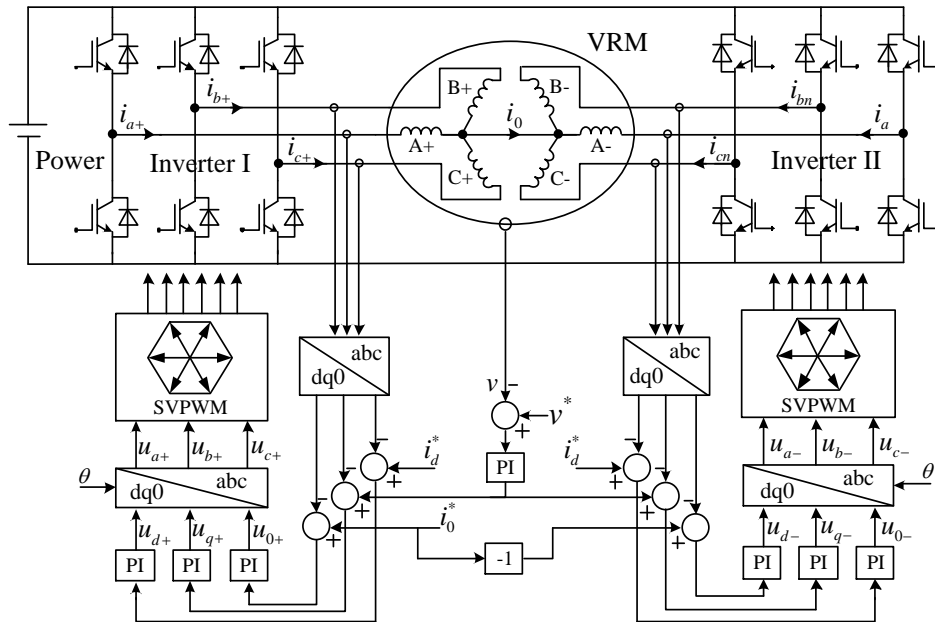
Fig. 3.3 Dual-inverter drive control for the proposed VRM.

Compared to the previous HE-VRM with separated AC and DC winding, the features of this new topology with integrated winding design can be listed as follows.

For machine design. (1) The slot area is enlarged for both AC armature excitation and DC field excitation. Therefore, smaller copper loss will be consumed when applying the same current, leading to machine efficiency improvement. (2) Under the same thermal limit, larger current excitation can be injected into the AC and DC integrated windings. This contribute to enhanced torque density.

For drive circuit. (1) More power devices are used, and the current scale of each power device should be increased due to the overlap of AC and DC current. (2) The voltage scale of power device is the same as that in previous separated design. (3) The over-modulation risk may occur with zero sequence current injection.

In general, this integrated design of AC and DC windings, gives a potential for machine itself to be designed with higher efficiency and higher torque density. with some sacrifice in the cost of drive circuit and complexity of control strategy. In this chapter, the influence of this integrated design on drive system is considered acceptable. Further, more efforts will be provided in machine design for electromagnetic performance boost.

(a)   (b)
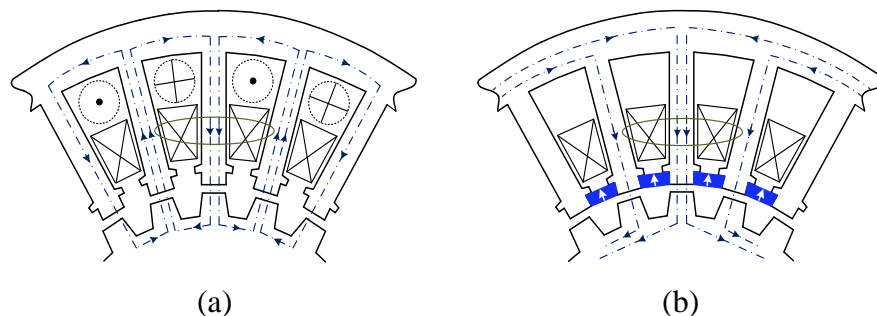
Fig. 3.4 Separation of the proposed topology and schematic magnetic circuits.
(a) DC-current-excited VRM. (b) Stator-slot-PM-excited VRM.

3.3 OPERATION PRINCIPLE

The operation principle of this new HE-VRM, can be illustrated by splitting it into two individual machines as shown in Fig. 3.4. One is a DC-current excited VRM and the other is a stator-slot-PM-excited VRM. As presented Fig. 3.4(a), in DC-VRM, excitation field is established by the DC current component in the integrated winding under zero-sequence current control. This can be considered as inserting a virtual DC field winding at stator side. With the variation of rotor permeance, pulsating armature flux is generated in DC-VRM, which contributes to reluctance torque generation. For stator-slot-PM-excited VRM, each slot PM and adjacent core form a pair of magnetic poles, as shown in Fig. 3.4(b), and this PM excitation field at stator side is modulated by the rotor permeance to interact with the armature winding. The torque capacity produced by slot PMs is theoretically better than DC current source for its bipolar flux feature. Besides, the flux linkage of two excitation sources can effectively overlap in armature winding, leading to torque density boost.

The features of this new HE-VRM can be summarized as

1) With a passive rotor, this new VRM maintains a good mechanical robustness, which can reduce the risk of PM damage compared with rotor-PM-excited machines.

2) Due to a non-overlapping design, the winding ends are short, and thus the end copper loss and material cost are both reduced.

3) Torque components excited by the zero-sequence current and slot PMs can effectively overlap, thus providing torque density boosting effect.

4) The magnetic return paths of zero-sequence current and slot PMs are in parallel. Hence, bidirectional zero-sequence current can be applied for wide-speed-range flux regulation. Besides, little demagnetization risk exists for slot PMs.

3.4 INTEGRATED CURRENT INJECTION

Based on the distribution principle and polarities of DC coils and AC coils in the common slots, the injected current into two sub-phase groups can be expressed as

$$
\begin{cases}
i_{A+} = i_{ac} \cdot \sin(\theta_e) + i_{dc} \\
i_{B+} = i_{ac} \cdot \sin(\theta_e - 2\pi/3) + i_{dc} \\
i_{C+} = i_{ac} \cdot \sin(\theta_e + 2\pi/3) + i_{dc} \\
i_{A-} = i_{ac} \cdot \sin(\theta_e) - i_{dc} \\
i_{B-} = i_{ac} \cdot \sin(\theta_e - 2\pi/3) - i_{dc} \\
i_{C-} = i_{ac} \cdot \sin(\theta_e + 2\pi/3) - i_{dc}
\end{cases}
\tag{3.1}
$$

where i_{A+}, i_{B+}, i_{c+} are the current flowing from the inverter I, and i_{A-}, i_{B-}, i_{c-} are the current flowing from the inverter II. i_{ac} is the amplitude of AC current component. i_{dc} is DC current component, which functions as the virtual DC field winding in the proposed DE-VRM. θ_e is the rotor electrical angle, which can be calculated as

$$
\theta_e = N_r \theta_r + \alpha
\tag{3.2}
$$

where N_r refers to the number of rotor PM pole pairs, θ_r refers to the mechanical angle, and α is the initial electrical angle.

By using Clarke and Park transformer matrix, the current excitation under αβ0 and dq0 coordinate systems, can be written as follows, taking current of inverter I as an example.

$$
\begin{bmatrix} i_{\alpha+} \\ i_{\beta+} \\ i_{\alpha\beta0+} \end{bmatrix} = \sqrt{\frac{2}{3}}
\begin{bmatrix}
1 & -\dfrac{1}{2} & -\dfrac{1}{2} \\
0 & \dfrac{\sqrt{3}}{2} & -\dfrac{\sqrt{3}}{2} \\
\dfrac{1}{\sqrt{2}} & \dfrac{1}{\sqrt{2}} & \dfrac{1}{\sqrt{2}}
\end{bmatrix}
\begin{bmatrix} i_{A+} \\ i_{B+} \\ i_{C+} \end{bmatrix}
\tag{3.3}
$$

$$
\begin{bmatrix} i_{d+} \\ i_{q+} \\ i_{0+} \end{bmatrix} =
\begin{bmatrix}
\cos\theta_r & -\sin\theta_r & 0 \\
\sin\theta_r & \cos\theta_r & 0 \\
0 & 0 & 1
\end{bmatrix}
\begin{bmatrix} i_{\alpha+} \\ i_{\beta+} \\ i_{\alpha\beta0+} \end{bmatrix}
\tag{3.4}
$$

55

By substituting Eq. (3.1) into Eq. (3.3) and Eq. (3.4), the relationship between the zero-sequence current from the inverter I and DC current can be derived as

$$i_{0+} = \sqrt{3}i_{dc} \tag{3.5}$$

Similarly, the relationship between the zero-sequence current from the inverter II and DC current can be expressed as

$$i_{0-} = -\sqrt{3}i_{dc} \tag{3.6}$$

Based on Eq. (3.5) and (3.6), it can be found i_{dc} is proportional to the zero-sequence current flowing from inverter I to inverter II through the neutral path, which means DC current component can be effectively regulated at the armature terminal by means of controlling zero-sequence current excitation.
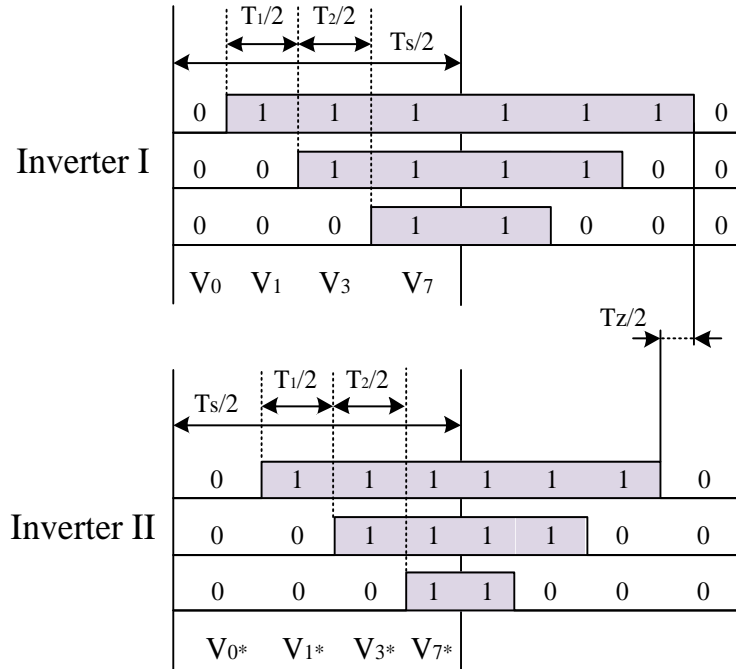
Fig. 3.5 Switching on-time of dual inverters and corresponding voltage vectors.

To generate zero-sequence current excitation, the zero-sequence voltage should be established by space vector pulse width modulation (SVPWM). In the traditional three-

phase inverter to drive a Y-connected machine. The zero-sequence voltage is established by utilizing space vector V_0 and V_7, which functions to shorten the switching-on time of either upper or lower power devices. To avoid the floating voltage of neutral point, V_0 and V_7 are divided evenly to achieve symmetrical SVPWM.

In the proposed machine driven by dual inverters, the zero-sequence voltage can be established by synchronously modifying the switching-on time of dual inverters as shown in Fig. 3.5 based on the reference value of zero-sequence voltage obtained the PI controller, which functions to minimizes the error between ideal zero-sequence current and feedback value. The modified switching-on time of dual inverters can be expressed as

$$\begin{cases} T_{a1} = T_1 + T_z, \ T_{b1} = T_2 + T_z, \ T_{c1} = T_0 + T_z \\ T_{a2} = T_1 - T_z, \ T_{b2} = T_2 - T_z, \ T_{c2} = T_0 - T_z \end{cases} \tag{3.7}$$

where T_{a1}, T_{b1}, T_{c1} are the switching-one time of three legs in inverter I, and T_{a2}, T_{b2}, T_{c2} are those of inverter II, respectively. T_1, T_2 are the calculated time of two effective space vectors in corresponding sectors. T_z is the reference voltage obtained by PI controller.

3.5 INDUCTANCE AND TORQUE EQUATION

In the proposed new HE-VRM, the self-inductance of each sub-phase can be expressed as follows, using A+ as an example

$$L_{A+} = L_{dc} + \sum L_n \cdot \sin(nN_r\theta_r + \alpha), \ n = 1, 2, 3... \tag{3.8}$$

where L_{dc} is the constant self-inductance component, and L_n is the amplitude of the nth harmonic self-inductance component.

Considering the counter-cyclical characteristic in the 24-slots and 22 pole-pairs design, the self-inductance of sub-phase A- is delayed by 180° electrical angle than that of A+. Accordingly, self-inductance of A- can be written as

$$L_{A-} = L_{dc} + \sum L_n \cdot \sin(nN_r\theta_r + n\pi + \alpha), \ n = 1, 2, 3... \tag{3.9}$$

Further, with a single-layer concentrated winding connection, little mutual-inductance exists between two sub-phase groups, thus the excited flux by i_0 can be expressed as

$$\phi_{A\_i0} = L_{A+} \cdot i_{dc} + L_{A-} \cdot (-i_{dc}) = 2i_{dc} \sum L_n \sin(nN_r\theta_r + \alpha), \ n = 1, 3, 5... \tag{3.10}$$

It is shown although DC biased self-inductance and even-order harmonic self-inductance exist in each sub-phase, their effects on excited flux are cancelled for counter-cyclical characteristic. The final flux linkage generated by i_0 contains the fundamental component and all odd-order harmonics components.

The torque component excited by i_0 can be deduced as

$$T_{i0} = \frac{m \cdot N_r \cdot \phi_{A\_i0} \cdot i_{ac}}{2} \tag{3.11}$$

where m is the number of phases. Neglecting saturation effect, the torque excited by both slot PMs and i_0 can be written as

$$T_e = T_{PM} + T_{i0} = \frac{m \cdot N_r \cdot \left(\phi_{A\_PM} + \phi_{A\_i0}\right) \cdot i_{ac}}{2} \tag{3.12}$$

where φ_{A_PM} and T_{PM} are the flux linkage and torque excited by stator slot PMs, similar with those in the conventional PM machines.

3.6 SLOT POLE COMBINATION

3.6.1 Influence on Drive Circuit Selection

The feasible slot pole combinations in the proposed topology can be expressed as

$$\begin{cases} N_s = 2mj, \ j = 1, 2, 3... \\ N_r = N_s \pm 2k, \ k = 1, 2, 3... \end{cases} \tag{3.13}$$

where N_s is the number of stator slots. The odd pole pairs are not considered considering

the influence of unbalanced magnetic pull. Further, according to the flux modulation mechanism, N_r should be in close to N_s to achieve a relatively high pole ratio and torque density. Hence, using a 24-slot stator, four potential slot pole combinations are studied in this paper, that are 24/20, 24/22, 24/26 and 24/28, separately. The slot angle with different slot pole combinations can be deduced as

$$\gamma = \frac{360°}{N_s} N_r \qquad (3.14)$$

The electrical angle difference $\Delta\theta_e$ between every two sub-phases can be calculated as

$$\Delta\theta_e = (h\gamma) \bmod (360°) \qquad (3.15)$$

where h is the interval number of slots between two sub-phases.

TABLE 3.1 Electrical Angle Difference between Two Sub-Phases

N_s	24	24	24	24
N_r	20	22	26	28
γ	300	330	330	300
$\Delta\theta_e$	0	180	180	0

As listed in Table 3.1, 24/20 and 24/28 cases have the same $\Delta\theta_e$ of 0°, while 24/22 and 24/26 cases have the same $\Delta\theta_e$ of 180°. Based on the coil distribution in the proposed machine, in 24/20 and 24/28 cases, polarities of virtual DC coil and AC armature coil are consistent, while these are opposite in 24/22 and 24/26 cases. Therefore, for 24/20 and 24/28 cases, the drive circuit to inject zero-sequence current can be simplified as presented in Fig. 3.6, in which every two sub-phases are positively connected and fed by common DC current flowing into the neutral point of splitting capacitors. It is shown the drive circuit for 24/20 and 24/28 cases is simpler compared to that of 24/20 and 24/28 cases.
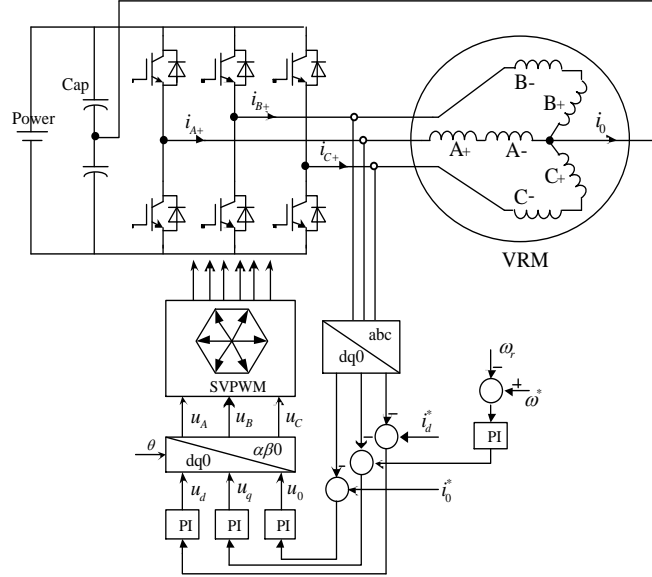
Fig. 3.6 Drive system for 24/20 and 24/28 design cases.

TABLE 3.2 Initial Dimension Parameters of the Proposed Machine

Symbol	Parameter	Unit	Value
d_{so}	Outer diameter of stator	mm	120
d_{si}	Inner diameter of stator	mm	69
d_{ro}	Outer diameter of rotor	mm	68.5
d_{ri}	Inner diameter of rotor	mm	20
δ	Air gap length	mm	0.5
l	Stack length	mm	50
h_{sy}	Height of stator yoke	mm	Variable
θ_{st}	Arc of stator teeth	°	Variable
θ_{pm}	Arc of slot PMs	°	Variable
h_{pm}	Height of slot PMs	mm	Variable
θ_{ro}	Outer arc of rotor poles	°	Variable
θ_{ri}	Inner arc of rotor poles	°	Variable
h_r	Height of rotor slots	mm	Variable
b_{s0}	Open width of stator slots	mm	3
h_{s0}	Height of stator shoes	mm	1

TABLE 3.3 Major Materials and Specifications

PMs		Steels	
Material	NdFeB35	Material	MG19_24
Remanence	1.2 T	Saturated point	1.8 T
Coercive force	915 kA/m	Mass density	7650 kg/m^3

TABLE 3.4 Torque Performance with Different Slot Pole Combinations

Number of stator slots	24	24	24	24
Number of rotor pole pairs	20	22	26	28
Height of stator yoke (mm)	5	5	5	5
Arc of stator teeth (°)	7	7	7	7
Height of slot PMs (mm)	2	2	2	2
Outer arc of rotor pole (°)	9	8	6.8	6.5
Inner arc of rotor pole (°)	10	9	8	7
Height of rotor slot (mm)	4	4	4	4
Cogging torque (Nm)	0.82	0.22	0.21	0.63
Rated torque (Nm)	4.41	4.23	4.11	3.92

3.6.2 Influence on Torque Performance

As is well known, slot pole combination usually has a leading influence on machine performance. In the proposed design, slot PM is the dominant source for torque generation. Hence, for the initial selection process, zero-sequence current is not applied.

Finite element simulation is adopted by using the commercial software Maxwell. The design values of some general dimension parameters are listed in Table 3.2. The materials of PM and steel, as well as their main specifications, are given in Table 3.3. The rotor parameters are optimized for each slot pole combination, thus to achieve best torque performance, and the stator parameters are set unchanged to ensure the same PM usage.

The design values after optimization are presented in Table 3.4. It is shown, 24/20 case has the largest rated torque, but its cogging torque is also distinct. When the ratio of cogging torque to rated torque is considered as the comparison indicator, 24/22 case is recommended. It should be pointed out, performance of 24/26 and 24/28 combinations is generally not comparable to that of 24/20 and 24/22 cases, which is caused by their increased PM leakage flux with reduced pole pitch.

In general, from a perspective of machine design, 24/22 case can achieve smaller cogging torque ratio than 24/20 case, while from a perspective of drive circuit, 24/22 case needs one more inverter for zero-sequence current injection compared to 24/20 case, which increases the system cost. In this paper, the machine performance is determined to have a higher design priority than system cost, and thus 24/22 case is selected to be further studied, while in cost-limited applications, 24/20 case is recommended.

3.7 FINITE ELEMENT ANALYSIS

3.7.1 No-load Flux Distribution

Firstly, the no-load sub-phase flux linkage of 24/22 design is calculated and plotted in Fig. 3.7, with corresponding harmonics distribution presented in Fig. 3.8. It can be noticed, when excited by only i_0 of 6A, the flux linkage generated in each sub-phase winding is unipolar and biased, while that excited by slot PMs is bipolar and alternating. Although rich flux harmonics exist in each sub-phase winding, the DC biased component and all even-order harmonics are cancelled due to counter-cyclical feature.

Then, the no-load flux distribution under different excitation status is plotted in Fig. 3.9. The main flux is denoted in blue, while the leakage flux in black. From Fig. 3.9(a), it can be seen, the main flux of i_0 will not pass through slot PMs. Meanwhile, the leakage flux of

i_0 starts from the wounded stator tooth, then passing through stator pole shoes and finally comes back from stator yoke. The leakage flux of slot PMs mainly forms its loop around stator pole shoes as shown in Fig. 3.9(b). Further, when two excitation sources are both active as given in Fig. 3.9(c), the main flux of i_0 and slot PMs can overlap together, while their leakage flux around stator pole shoes can be cancelled to some extent.

The back emf of synthetic phase A is calculated and plotted in Fig. 3.10. It can be noticed, the back emf excited by i_0 and slot PMs are entirely in phase and thus they can effectively overlap together and contribute to boosted voltage.
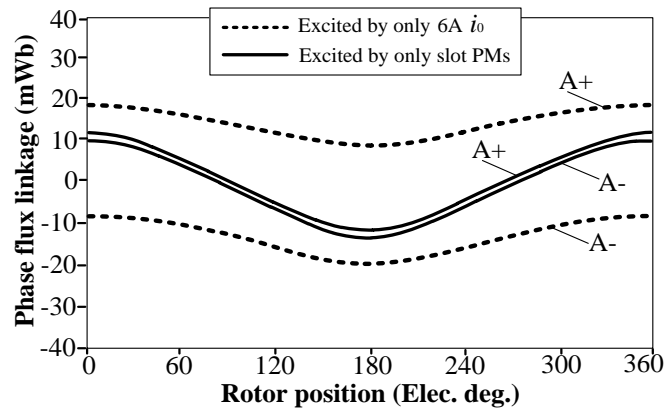
Fig. 3.7 No-load sub-phase flux linkage.

(a)

(b)
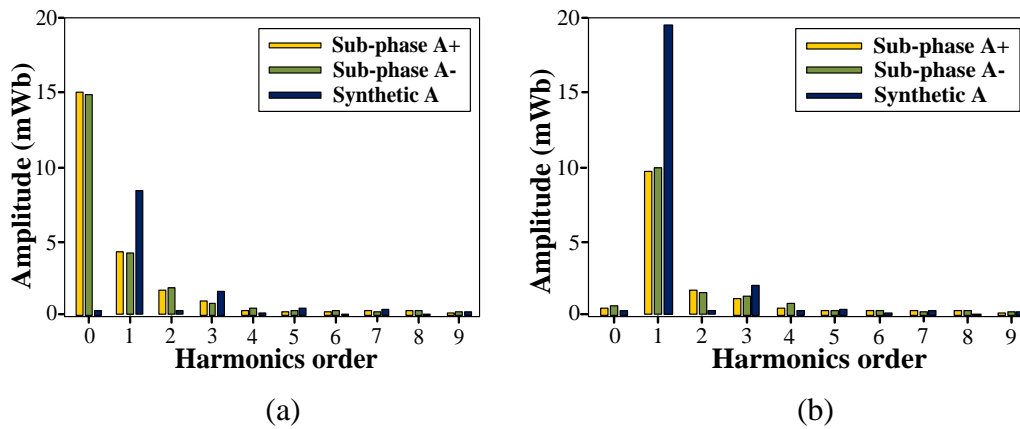
Fig. 3.8 Harmonics in sub-phase flux linkage (a) Only 6A i_0. (b) Only slot PMs.

(a)   (b)   (c)
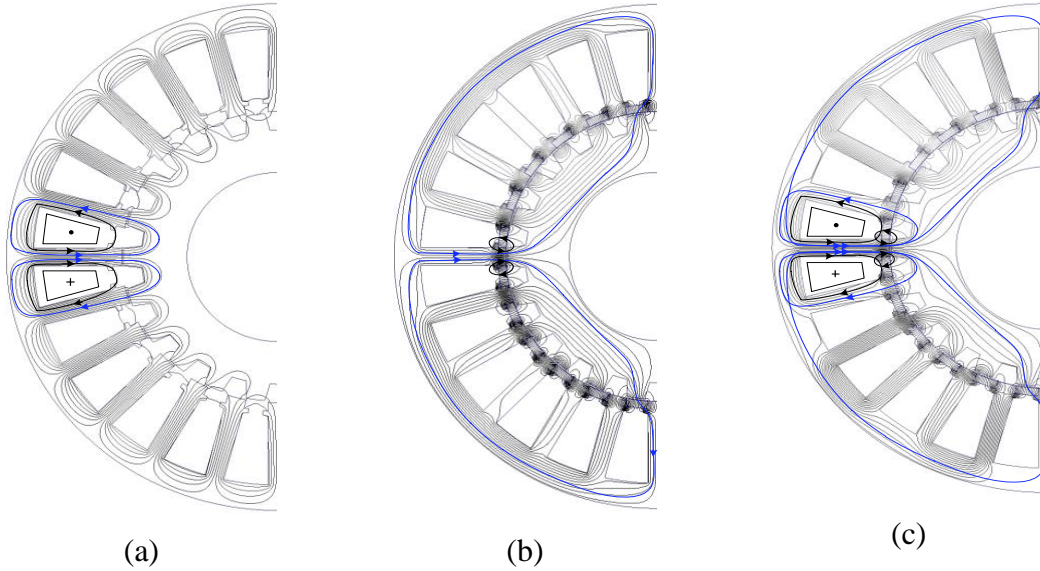
Fig. 3.9 Exciting field. (a) Only 6A i_0. (b) Only slot PM. (c) Slot PM and 6A i_0.
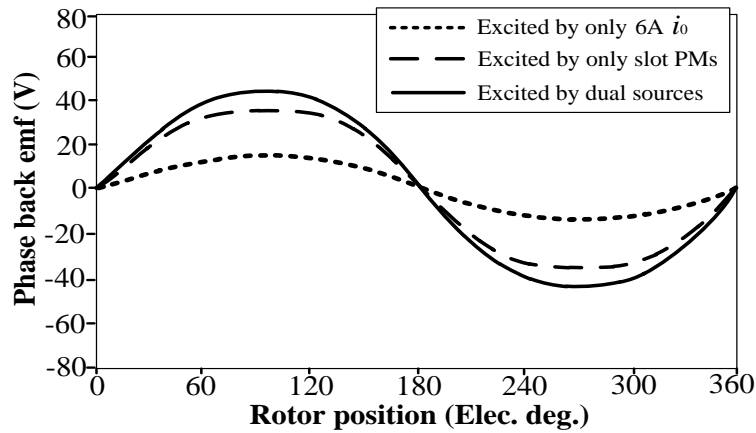
Fig. 3.10 No-load back emf of synthetic phase A.

3.7.2 Injected Current and Steady Torque

Fig. 3.11 presents the injected current excitation into integrated winding. Sub-phase A+ and sub-phase A- share the same AC current component with 5A amplitude and same electrical angle. However, sub-phase A+ has positive DC current of 3.5A under 6A i_0 control, while A- has negative DC current of 3.5A. Steady torque at different excitation status is calculated and presented in Fig. 3.12. It can be noticed, both slot PMs and i_0 can

contribute to the steady torque generation. The synthetic average torque is boosted when dual excitation sources are both active, and the torque ripple ratio is mitigated to some extent, benefiting from the reduction of slot PM leakage when i_0 is applied. This torque improvement proves the validity of the proposed topology.
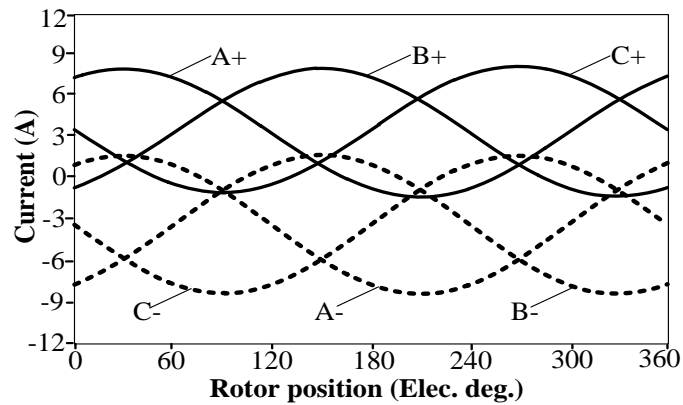
Fig. 3.11 Integrated AC and DC current excitation.
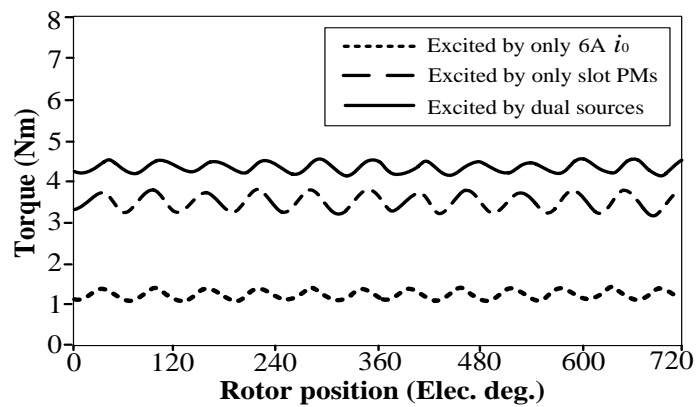
Fig. 3.12 Steady torque components.

3.7.3 Flux Regulation Ability

As presented in Fig. 3.13, the flux linkage excited by i_0 is in parallel with that produced by slot PMs. Meanwhile, its polarity depends on the direction of i_0, which means, by controlling the flowing direction and amplitude of i_0, the synthetic flux linkage at armature

terminal can be flexibly strengthened or weakened. This contributes to effective flux control for the speed extension. The no-load back emf curve is collected in Fig. 3.13, which proves that flux can be bidirectionally regulated by i_0.
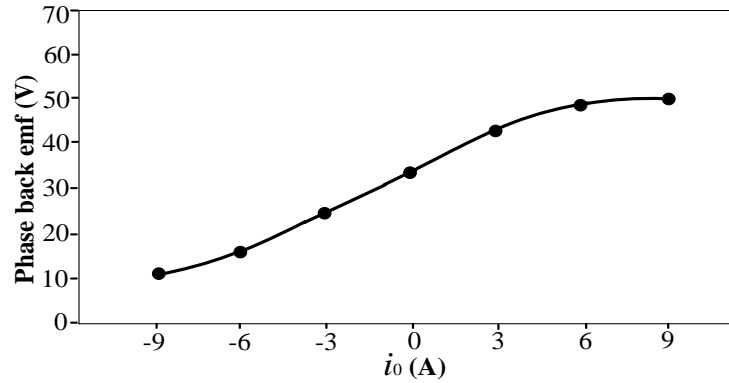
Fig. 3.13 No-load phase back emf with different zero-sequence current.
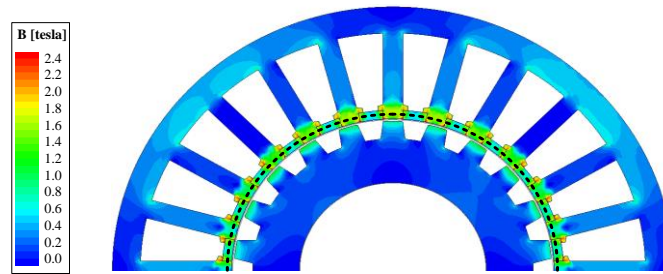
Fig. 3.14 Observation line for flux density distribution.
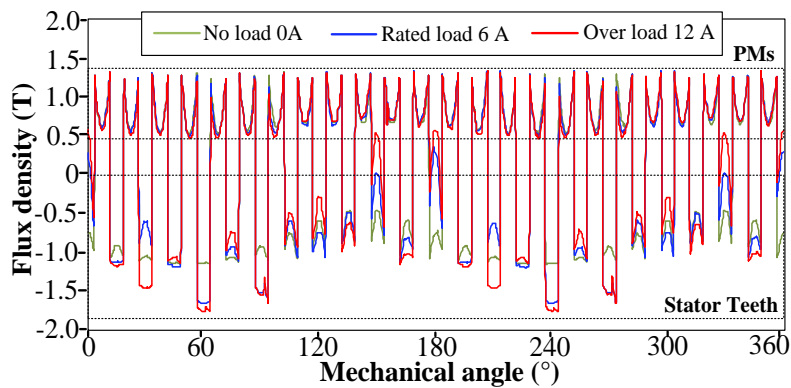
Fig. 3.15 Flux density at different load condition.

3.7.4 Demagnetization Risk

To evaluate the PM demagnetization risk, an observation line is selected across the central line of PMs as shown in Fig. 3.14. Then, PM flux density at different load conditions is calculated in Fig. 3.15. It is shown, with load changing, the working point of PMs keeps almost constant, while flux density in stator teeth changes distinctly. This is because PMs are placed in slots, and thus flux linkage of armature current will not pass through PMs, which contributes to parallel magnetic circuit. Hence, if the cooling condition is allowed, PM demagnetization by load can be avoided in the proposed machine.

3.7.5 Power Factor

The power factor of the proposed machine at rated condition is evaluated by measuring the phase angle difference of on-load current and voltage. The power factor of the proposed machine at rated condition is about 0.62, which is not so good due to large magnetizing inductance, similar with that in other flux-modulated machines. Further, the influence of i_0 injection on power factor is evaluated as shown in Fig. 3.16. It is shown injecting positive i_0 can increase power factor slightly, benefiting from the enhanced air gap flux density.
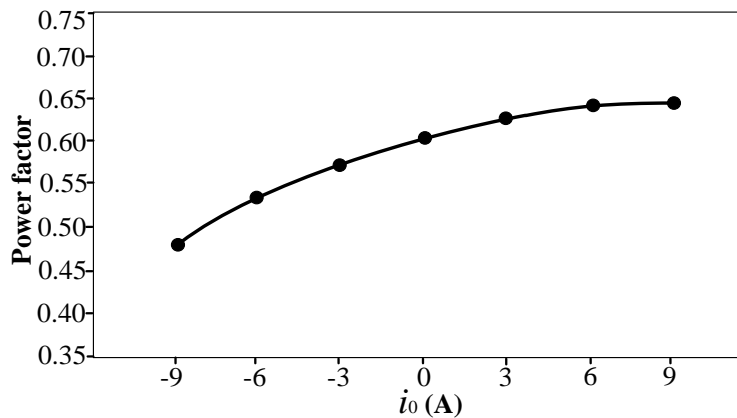
Fig. 3.16 Power factor with different zero-sequence current.

3.8 DESIGN OPTIMIZATION AND COMPARATIVE STUDY

In the proposed machine, three control variables, i_d, i_q and i_0, should be considered at armature terminal. i_d is usually applied for reluctance torque generation based on saliency effect. In the proposed design, saliency effect is not distinct with 24-slot 22-pole-pairs combination and thus i_d is maintained at zero. Then, i_q and i_0 are combined for torque generation. The electrical load for each phase winding can be expressed as

$$i_{rms} = \sqrt{\left(i_q^2 + i_0^2\right)/3} \tag{3.16}$$

To evaluate the machine performance with different i_q and i_0 combination, the ratio of i_0 can be further defined as

$$k_{i0} = i_0 / \sqrt{i_q^2 + i_0^2} \tag{3.17}$$

when the ratio of i_0 is zero, there will be only i_q injection, which is similar with that in traditional surface-mounted PM machines. In the following, the influence of leading design parameters is assessed with different i_q and i_0 combination.

3.8.1 Parameter Analysis

Under different current density, the influence of ratio of i_0 on machine performance is analyzed, including the average torque, torque ripple, core loss and PM eddy current loss. As shown in Fig. 3.17(a), with increasing of current density from 5 to 7 A/mm^2, the optimal ratio of i_0 to achieve the highest torque increases from 9% to 18% approximately. Two reasons account for this trend. On one hand, torque excited by i_0 has a square relationship to current value, while that excited by slot PMs is linearly related. On the other hand, the torque component of slot PMs will be closed to saturation point with the increase of current

density, thus larger ratio of i_0 can work for torque generation. Under 7A/mm^2 current density, the average torque with optimal i_0 ratio is 8% higher than that with only i_q injected. Further, it can be seen in Fig. 3.17(b), (c) and (d), i_0 injection shows a positive influence on the torque ripple reduction and loss distribution.
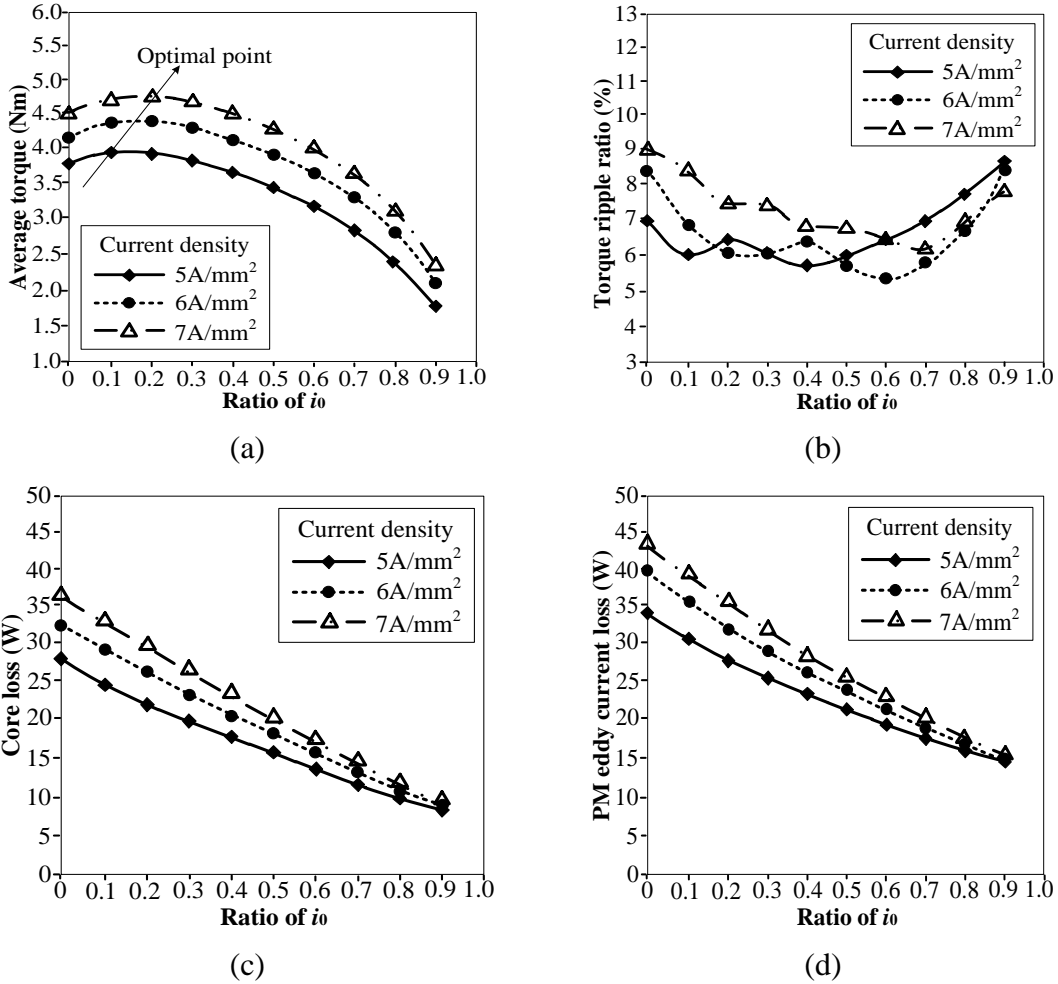
Fig. 3.17 Influence of current density with different ratio of i_0. (a) Average torque. (b) Torque ripple ratio. (c) Core loss. (d) PM eddy current loss.

The influence of PM height with different ratio of i_0, is also evaluated in Fig. 3.18. The current density is fixed at 5 A/mm^2. With the increase of PM height, the optimal ratio of i_0 to achieve the highest torque shows decrease trend. Meanwhile, the PM height has a larger

influence on eddy current loss than core loss. Further, the influence of air gap length with different ratio of i_0 is studied as shown in Fig. 3.19. The current density is set at 5 A/mm^2. With the decrease of air gap length, the optimal ratio of i_0 increases accordingly. This is because the excitation ability of i_0 is more sensitive to the air gap reluctance than that of PMs. From Fig. 3.17, 3.18 and 3.19, it can be concluded, regardless of design parameters, injecting i_0 always presents a positive influence on the reduction of torque ripple and loss distribution, benefiting from the reduction of PM leakage to some extent.
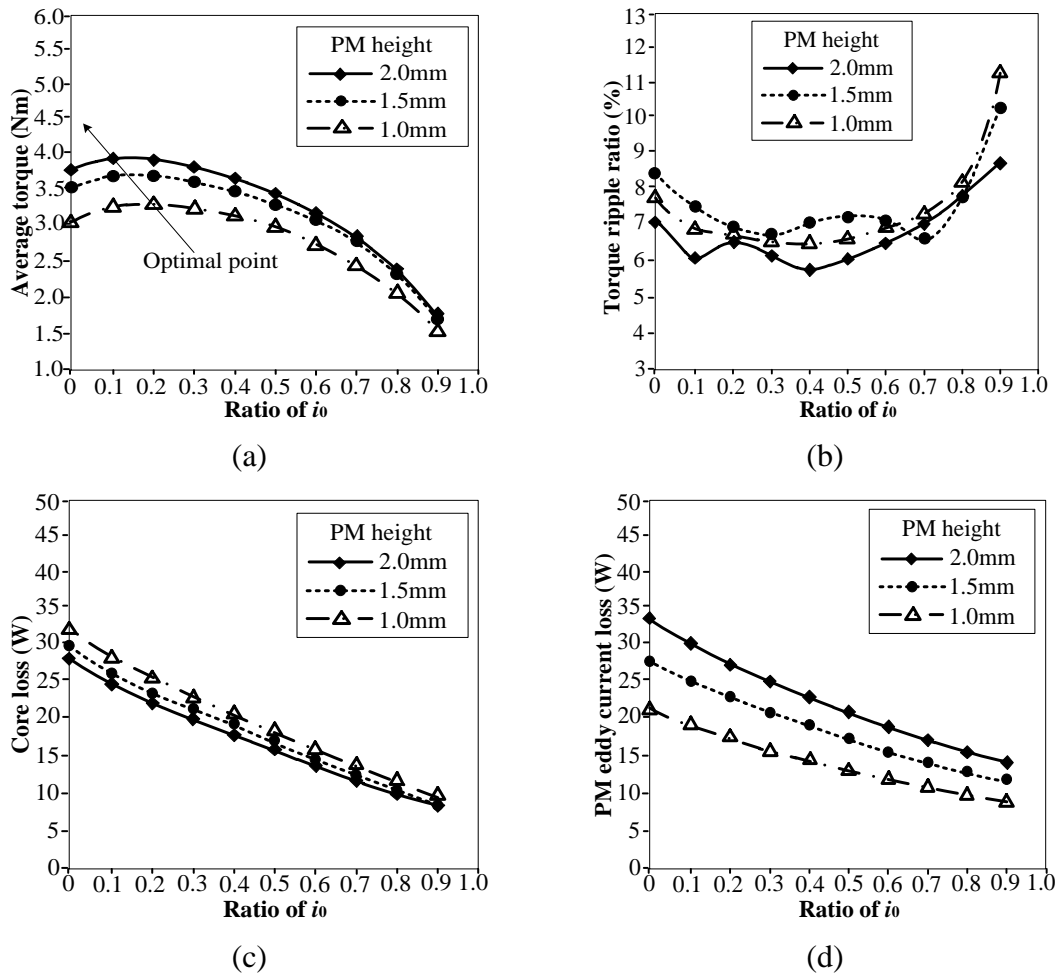
Fig. 3.18 Influence of PM height with different ratio of i_0. (a) Average torque. (b) Torque ripple ratio. (c) Core loss. (d) PM eddy current loss.
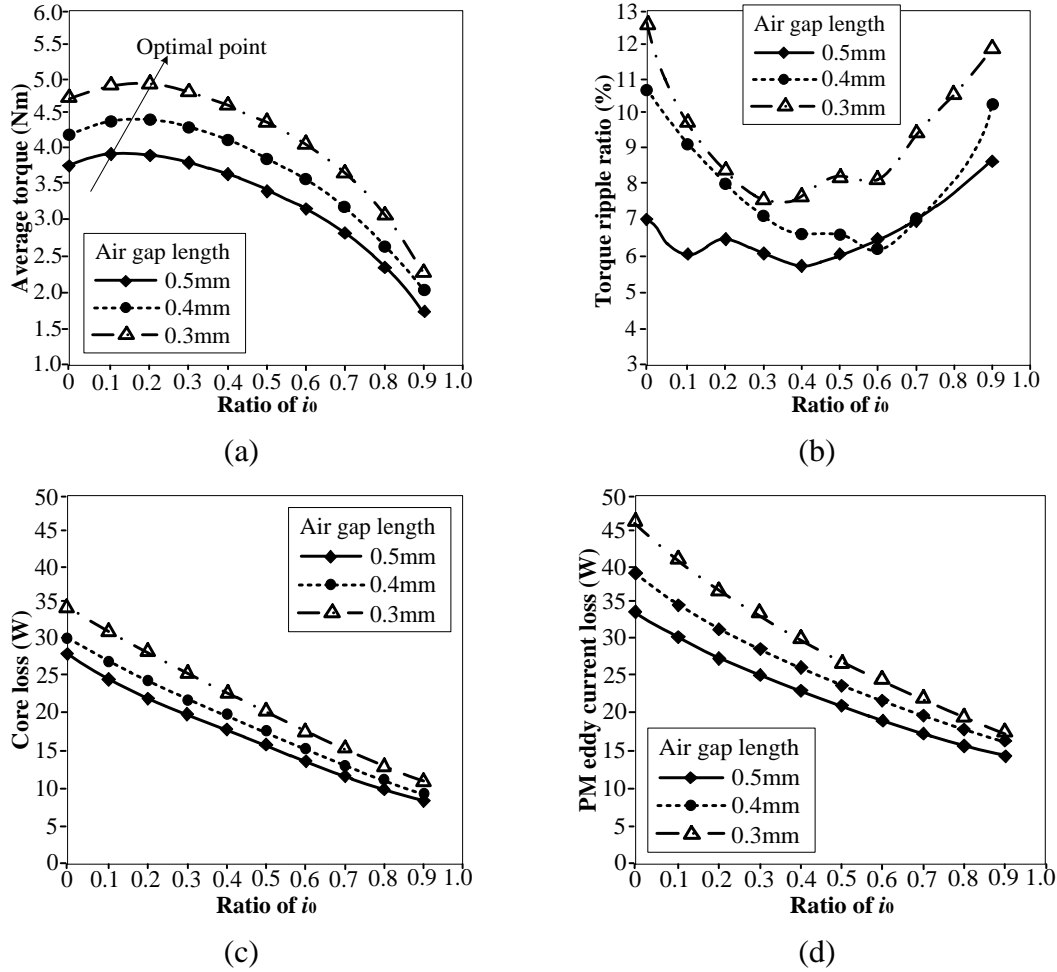
Fig. 3.19 Influence of air gap length with different ratio of i_0. (a) Average torque. (b) Torque ripple ratio. (c) Core loss. (d) PM eddy current loss.

3.8.2 Design Optimization

An intelligent optimization algorithm, namely genetic algorithm (GA) is adopted. GA has three operation factors, reproduction, crossover and mutation. Reproduction generates most adaptive individuals, when crossover and mutation mainly expand searching scope. The GA is initialized as, a population of 25 elements, maximum generation number of 20, crossover factor of 0.8 and mutation factor of 0.2. Fig. 3.20 illustrates the optimization flowchart. The maximum torque and efficiency are two optimization objectives. Torque ripple ratio less than 10% is considered as the optimization restriction.
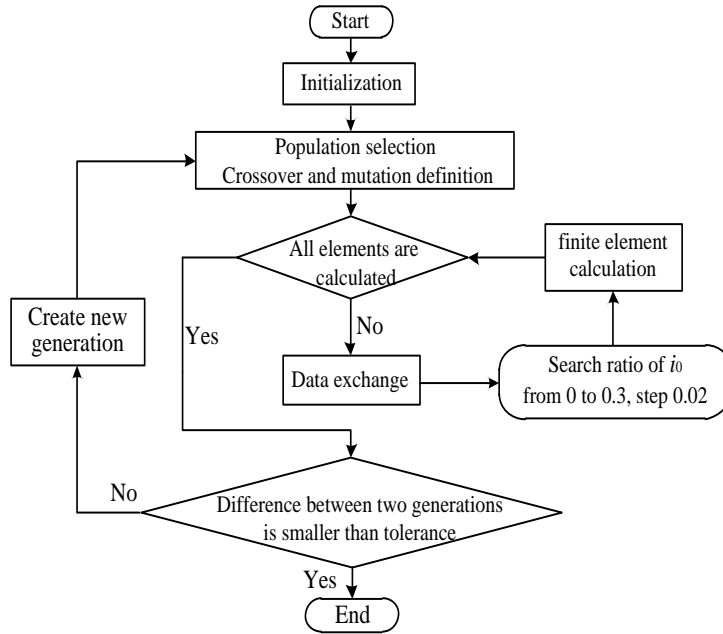
Fig. 3.20 Flowchart of the GA and Maxwell coupled optimization.
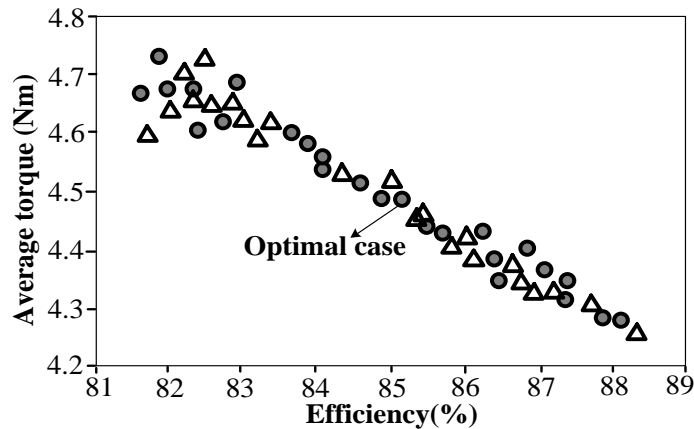
Fig. 3.21 Optimization results of last two generations.

During this optimization, the air gap length is fixed at 0.5mm and the current density is fixed at 7A/mm^2. The optimal ratio of i_0 is searched for all the elements in each generation. Further, optimization results of last two generations are given in Fig. 3.21. The optimal solution is defined as in which the product of toque and efficiency arrives the maximum value. The final parameters are listed in Table 3.5. After optimization, about 4.5 Nm average torque and 84% efficiency is achieved under 16% i_0 injection.

TABLE 3.5 Dimension Parameters, Boundary Limits and Optimal Values

Parameters	Lower limit	Upper limit	Optimal
Height of stator yoke (mm)	4.5	9.5	6.2
Arc of stator teeth (°)	6.5	8.5	7.3
Height of slot PMs (mm)	1.5	3.5	2.2
Outer arc of rotor pole (°)	6.5	8.5	6.8
Inner arc of rotor pole (°)	6.5	10.5	8.2
Height of rotor slot (mm)	3.5	4.5	4.2

3.8.3 Comparative Study

A performance comparison is given between three topologies as presented in Fig. 3.22. One design is the existing VRM with separated AC and DC field windings. Another is the proposed VRM equipped with integrated AC and DC windings. The other is the traditional SPM excited by alternating rotor PMs. The interior PM machine is considered for this comparison, since IPM machine is usually designed at high speeds with less pole pairs, while my proposed topology is designed with multi pole pairs for low-speed direct drive. It not reasonable to compared to two machines with different speeds and pole pair designs. For a fair comparison, the machine dimensions, materials types, rotor pole pairs, PM volume and the whole copper loss are all kept the same. Each design is optimized by GA and Maxwell combined method to achieve optimal torque and efficiency performance.

The design parameters and calculated performance for three topologies are listed in Table 3.6. It is shown the proposed VRM with integrated AC and DC windings can achieve higher torque and efficiency compared to the existing topology with extra DC field winding. Compared to traditional SPMs, the torque and efficiency of the proposed design are slightly lower, while its flux weakening ability is much better. Moreover, in the proposed machine,

PM demagnetization risk is avoided due to the unique PM arrangement in slots. Its rotor mechanical strength is also improved. It can be concluded that the proposed machine has a better robustness than the traditional SPMs.

(a)   (b)   (c)
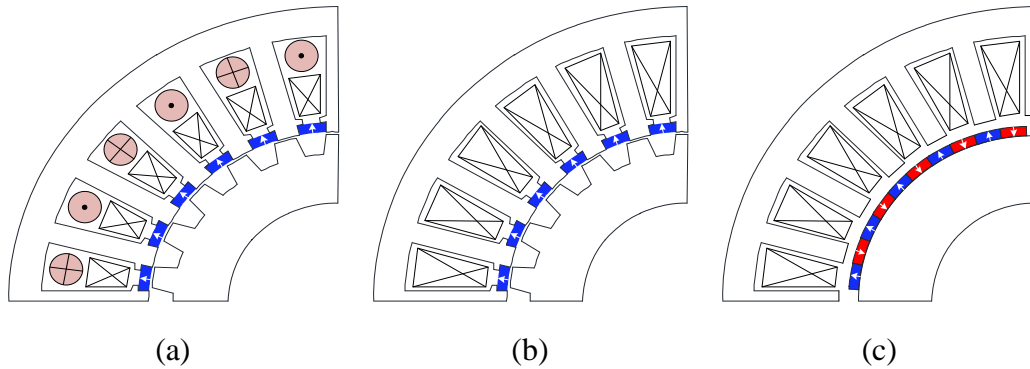
Fig. 3.22 (a) Existing VRM with separated AC and DC coils [22]. (b) Proposed VRM with integrated AC and DC coils. (c) Traditional SPM.

TABLE 3.6 Performance Comparison for Three Machines

Parameters	Unit	Existing	Proposed	SPM
Outer diameter	mm	120	120	120
Stack length	mm	50	50	50
Air gap length	mm	0.5	0.5	0.5
Stator slot number	-	24	24	24
Rotor pole pairs	-	22	22	22
PM volume	mm^3	10500	10500	10500
AC copper loss	W	20	34	40
DC copper loss	W	20	6	-
Rated torque	Nm	3.4	4.6	5.1
Rated Efficiency	%	78	85	88
Flux weakening	-	Good	Good	Poor
PM demagnetization	-	No	No	Yes
Rotor robustness	-	Good	Good	Poor

(a)   (b)   (c)
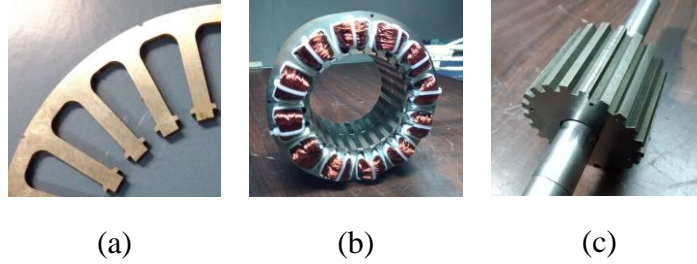
Fig. 3.23 Protype details. (a) Stator lamination. (b) Stator assembly. (c) Rotor assembly.
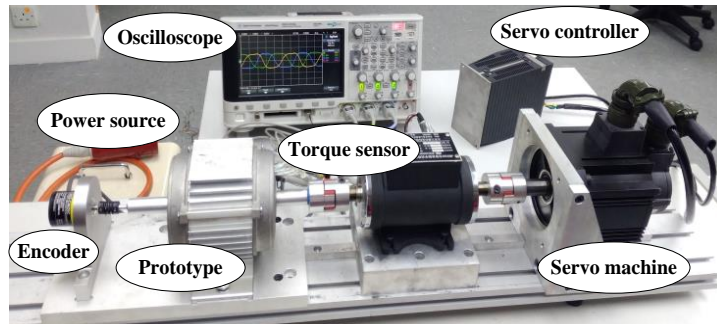
Fig. 3.24 Experimental platform based on the assembled prototype.

3.9 EXPERIMENTAL VERIFICATION

To verify the feasibility of the proposed machine, a prototype is manufactured as shown in Fig. 3.23. The prototype parameters are in line with finite element modeling, as listed in Table 3.2. Fig. 3.24 shows the experimental platform, which consists of the prototype, a servo motor, torque sensor, DC power source, drive controller and oscilloscope.

The no-load back emf at speed 1000 rpm is collected against different i_0 and plotted in Fig. 3.25(a), which proves bidirectional flux regulation ability of i_0. By injecting constant current into the armature winding and testing torque value at different rotor positions, torque angle curve is obtained as given in Fig. 3.25(b). The errors between tested results and finite element prediction are acceptable considering manufacturing tolerance.

The on-load experiments are conducted with different current control strategies. When there is only i_q current injected into the armature winding, steady current and output torque

are plotted in Fig. 3.26(a). It can be found, fed by dual independent inverters, good current control effect can be achieved for each sub-phase, and steady torque can be generated. After that, combined i_q and i_0 are injected into the armature winding. The synthetic value of two current components keeps unchanged compared with that when only i_q is injected. The optimal ratio of i_0 is achieved by searching the point at which output torque arrives the maximum value. Fig. 3.26(b) shows the steady current and torque waveforms with 15% injection ratio of i_0. The output torque is enhanced by about 10% compared to that with only i_q injection, thus proving the torque boost effect of i_0 and i_q combined control.
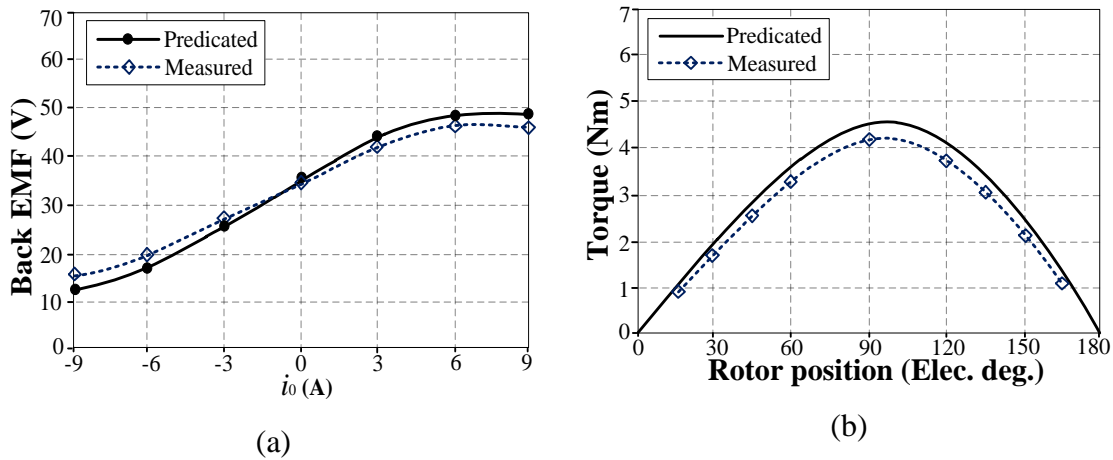
Fig. 3.25 (a) Back emf curve against i_0 . (b) Static torque angle curve.
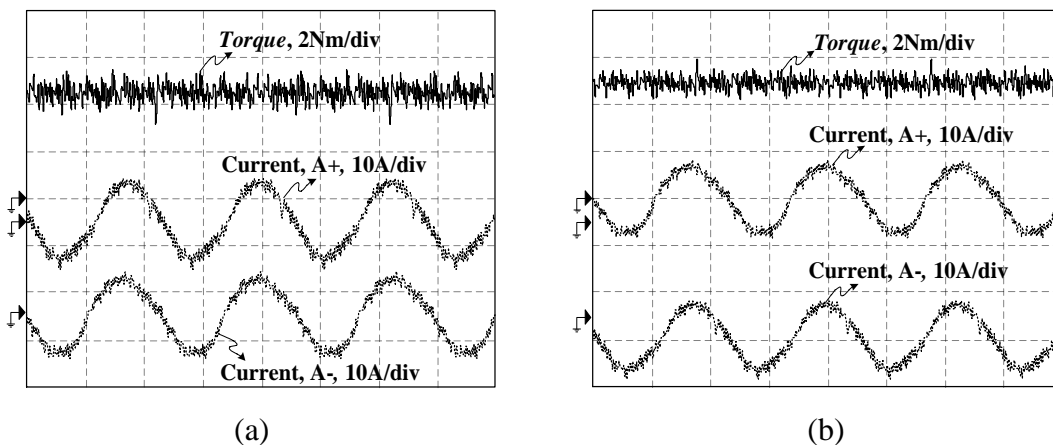
Fig. 3.26 Steady current and torque. (a) Without i_0. (b) With 15% i_0.
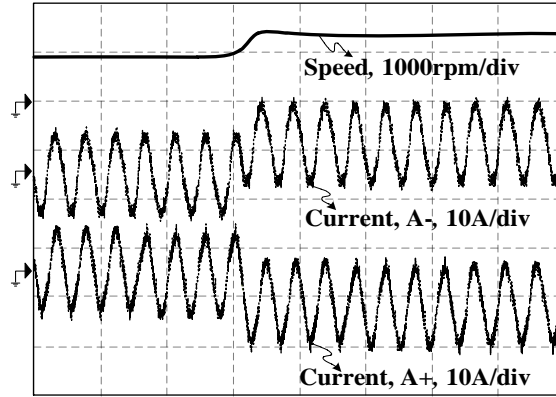
Fig. 3.27 Flux weakening operation by negative i_0 injection.

|(a)|(b)|
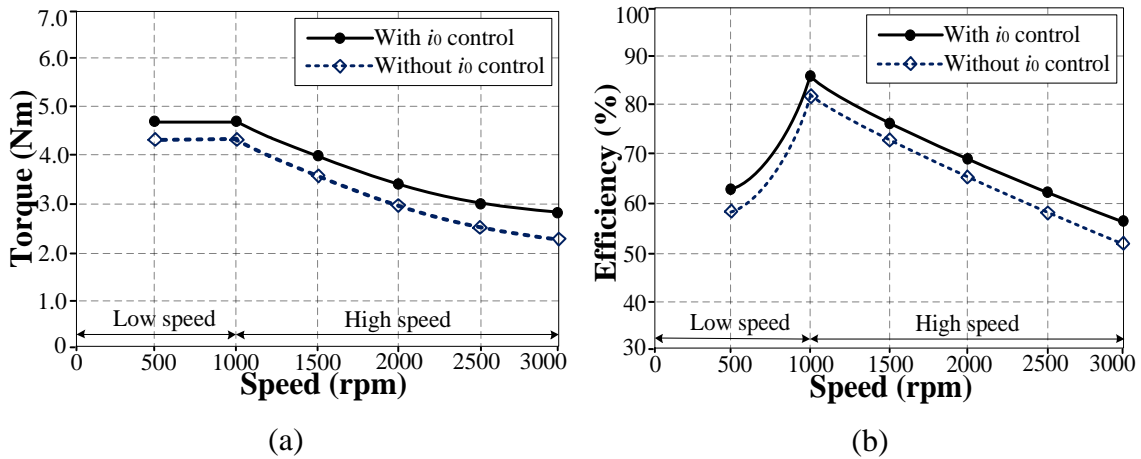
Fig. 3.28 (a) Torque speed curves. (b) Efficiency speed curves.

The flux weakening is performed at the base speed 1000 rpm. As presented in Fig. 3.27, with negative i_0 injection, flux weakening effect and speed extension are achieved.

Finally, the torque-speed curves are evaluated with different control strategies. The voltage restriction of DC supply is 160V. When the machine operates under the base speed, the constant torque control is applied with optimal i_0 injected. When it runs over the base speed. Flux weakening operation is applied for speed extension. Two flux weakening strategies are considered in this paper. One is by applying negative i_d for flux weakening, similar with that in conventional PM machine. The other is by applying both i_d and i_0 for combined flux weakening operation. The i_d directly control the PM magnetic field, while

77

the i_0 gives parallel flux component. The tested torque and efficiency are given in Fig. 3.28. It can be found higher torque and efficiency can be achieved in the whole speed region with extra i_0 control. The efficiency improvement is due to torque boost effect as well as loss mitigation with extra i_0 control. In general, the proposed machine achieves improved performance with i_0 control in both low-speed and high-speed regions.

3.10 CONCLUSION

This chapter proposes an improved design of new hybrid excitation Vernier reluctance machine with integrated AC and DC winding by utilizing the zero-sequence current control. This new machine employs slot PMs as the dominating source for torque generation based on the flux modulation mechanism. Further, the zero-sequence current excitation is injected into armature winding to function as extra DC field source and establish a hybrid magnetic circuit without the need of DC field winding. Meanwhile, zero-sequence current excitation can serve as an additional control variable for flux weakening and speed extension. In this chapter, the machine configuration, operation principle and its integrated current injection method are introduced in detail. The feasibility of the proposed machine is verified by both finite element analysis and prototype tests. It reveals that, under a fixed current density and thermal limit, with 10% to 20% of zero-sequence current injection, the proposed machine can achieve about 10% torque density boost and 30% torque ripple reduction. Meanwhile, core loss and PM eddy current loss can be distinctly mitigated with zero-sequence current injection due to leakage flux reduction, leading to efficiency increase. However, with the use of dual inverters, the increased complexity of drive circuit and control strategy are disadvantageous. Future works, for instance, developing fault-tolerant ability under this drive structure, could help to balance the system cost and performance.

CHAPTER 4. PROPOSED HYBRID EXCITATION DUAL PM MACHINE BASED ON TRIPLE FLUX MODULATION AND ARMATURE HARMONICS DIVERSITY

4.1 INTRODUCTION

Dual-PM-excited machine is a relatively new solution, which integrates consequent-pole PM sources at both stator and rotor to achieve enhanced torque density. Besides, benefiting from the controllability of stator PMs, brushless flux weakening operation can be achieved. Therefore, hybrid excitation dual PM machine is a promising solution for electric vehicles. Due to the co-existence of dual PM sources, the design of PM layout becomes very flexible. The existing literature usually adopts PMs alternately mounted on stator teeth to form a consequent-pole stator PM source, which results in a weak torque generation at stator side due to its biased flux feature. Besides, the flux weakening mechanism by controlling stator PMs, brings a contradiction between the flux weakening range and demagnetization risk, considering the relatively weak power contribution of stator PM source.

This chapter presents a new parallel hybrid excitation dual PM machine with enhanced torque density and improved flux weakening capability. The key is to artificially construct the harmonics diversity with a single-layer concentrated armature winding in the stator and simultaneously couple triple flux modulation effect. Enhanced torque density is obtained in this new topology due to the symmetrical flux modulation effect between dual PM sources. Moreover, benefiting from a parallel excitation characteristic of hybrid magnetic circuit, the demagnetization risk is significantly mitigated for stator PM source and thus an extended speed range by flux weakening operation can be obtained.
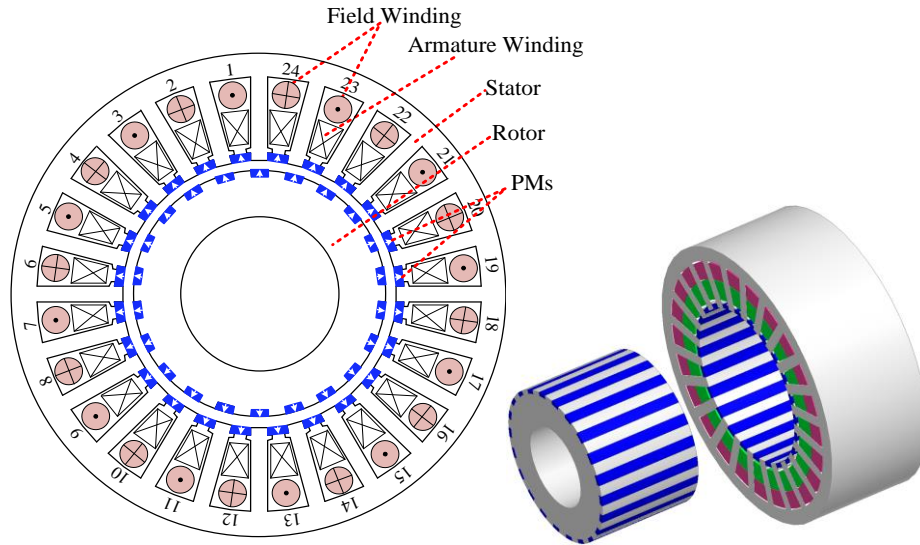
Fig. 4.1 Configuration of the proposed HE-DPMM.
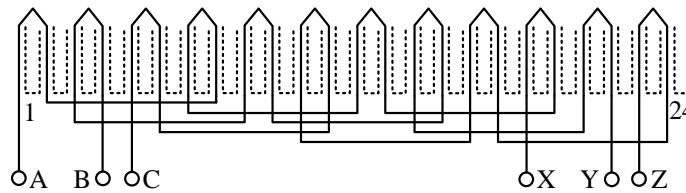
Fig.4.2 Connection of armature winding.
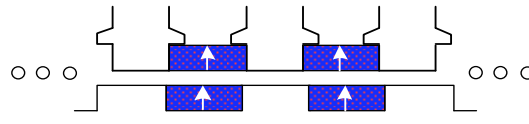
Fig.4.3 Illustration of PM magnetization modes.

4.2 MACHINE STRUCTURE

Fig. 4.1 presents the configuration of the proposed topology. This machine consists of a 24-slot stator and a 22-pole rotor. Two sets of windings are arranged in the stator slots, named as AC armature winding and DC field winding, respectively. The DC field coils are uniformly wound on stator teeth with alternate polarities. The connection of AC armature winding is presented in Fig. 4.2. Each slot opening at stator side is mounted with PM and

the rotor employs a consequent-pole structure. Both stator-slot PMs and rotor PMs are radially magnetized in the same outward direction, as highlighted in Fig. 4.3.

The merits of proposed machine can be summarized as

1) The AC armature winding and DC field winding both adopt a single-layer centralized configuration, which leads to relatively shorter ends, reduced materials, eliminated layer insulation and thus higher space factor.

2) Dual PM sources provide symmetrical flux modulation effect, which significantly boosts the air gap flux density as well as machine torque density.

3) The DC field excitation and stator-slot PM excitation have parallel magnetic circuits, and the demagnetization risk exists for stator-slot PMs can be avoided.

4) De-excitation operation can be achieved when this machine works as a generator under power device short-circuit situation. This can avoid a huge strike of short-circuit current in electrical system, which is extremely important for some safety-critical applications.

4.3 OPERATION PRINCIPLE

There are three excitation sources in the proposed machine, and they have entirely different pole pair numbers (PPN). Based on the machine structure, PPN for each source can be expressed as

$$\begin{cases} p_{DC}=N_s/2 \\ p_{PMs}=N_s \\ p_{PMr}=N_r \end{cases} \tag{4.1}$$

where p_{DC} is the PPN of DC field excitation, p_{PMs} is the PPN of stator-slot PM excitation, p_{PMr} is the PPN of rotor PM excitation, N_s is the number of stator teeth, and N_r is the number of rotor salient poles, respectively.

(a)

(b)

(c)
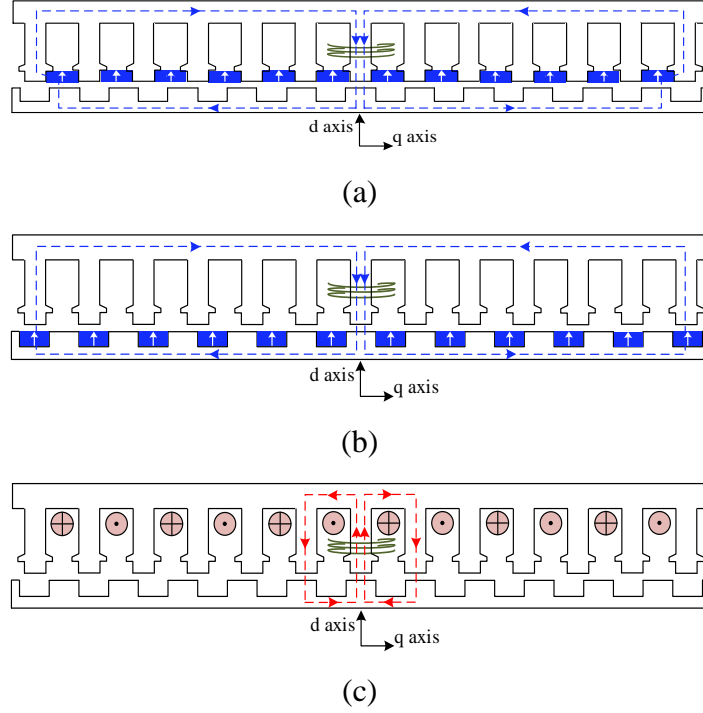
Fig. 4.4 Schematic magnetic circuit of individual excitation source. (a) Stator-slot PM excitation. (b) Rotor PM excitation. (c) DC field excitation.

In this proposed topology, there are altogether three kinds of flux modulation effect as described in Fig. 4.4. Firstly, each slot PM and adjacent stator teeth constitute a pair of magnetic poles. This uniform excitation field at stator side is modulated by rotor salient poles and then interact with armature winding. Secondly, each rotor PM and adjacent salient pole form a pair of magnetic poles. This uniform excitation field at rotor side is modulated by stator teeth and then interact with armature winding. Thirdly, all DC field coils, which are identically wounded at stator side, constitute a uniform excitation field, further modulated by rotor salient poles and then interact with armature winding.

Based on the flux modulation theory, PPN of excited harmonics components by different excitation sources are governed by

$$PPN_{m,k} = \left| mp_s \pm kp_r \right|, \ m = 1,3,5...,k = 0,1,2,3... \tag{4.2}$$

where p_s is the PPN of each excitation source, p_r is the number of corresponding modulation unit. Based on Equ.(4.2), the excited harmonics by three excitation sources can be deduced as given in Table 4.1. Moreover, their dominant harmonic components are further presented in Table 4.2. When m=1, k=0, the excited components are produced by excitation sources without any flux modulation effect; when m=1, k=1, the excited components are the dominant harmonics generated by flux modulation effect. It can be noticed, with a stator slot PM arrangement, two PM sources have entirely symmetric flux modulation effect, which can provide enhanced air gap flux density and torque density.

As is well reported in the existing literature, to transmit the maximum electromagnetic torque in flux modulated machines, the PPN of armature winding is governed by

$$p_a = |p_s - p_r| \tag{4.3}$$

Due to the co-existence of triple flux modulation effect in the proposed topology, the design of armature winding becomes a key issue, since the armature winding must be able to interact with three excitation sources effectively at the same time. The effective PPN of armature winding designed for each excitation source can be deduced as

$$\begin{cases} p_{\text{a\_to\_PMs}} = |N_s - N_r| \\ p_{\text{a\_to\_PMr}} = |N_s - N_r| \\ p_{\text{a\_to\_DC}} = |N_s/2 - N_r| \end{cases} \tag{4.4}$$

It can be found, the winding design of stator slot PMs and rotor PMs are consistent due to symmetrical flux modulation effect, while the winding design for DC field source is different. Therefore, it is necessary to find an unconventional armature winding design to interact with three excitation sources simultaneously.

TABLE 4.1 Flux Modulation Effect of Three Excitation Sources.

Excitation source	Modulation unit	PPN of excitation source	Number of modulation unit	Excited harmonics
Slot PM	Rotor poles	N_s	N_r	$|mN_s \pm kN_r|$
Rotor PM	Stator teeth	N_r	N_s	$|mN_r \pm kN_s|$
DC source	Rotor poles	$N_s/2$	N_r	$|mN_s/2 \pm kN_r|$

TABLE 4.2 Dominant Harmonics Excited by Three Excitation Sources.

Excitation source	m=1, k=0	m=1, k=1	
Slot PM	N_s	$N_s + N_r$	$|N_s - N_r|$
Rotor PM	N_r	$N_s + N_r$	$|N_s - N_r|$
DC source	$N_s/2$	$N_s/2 + N_r$	$|N_s/2 - N_r|$
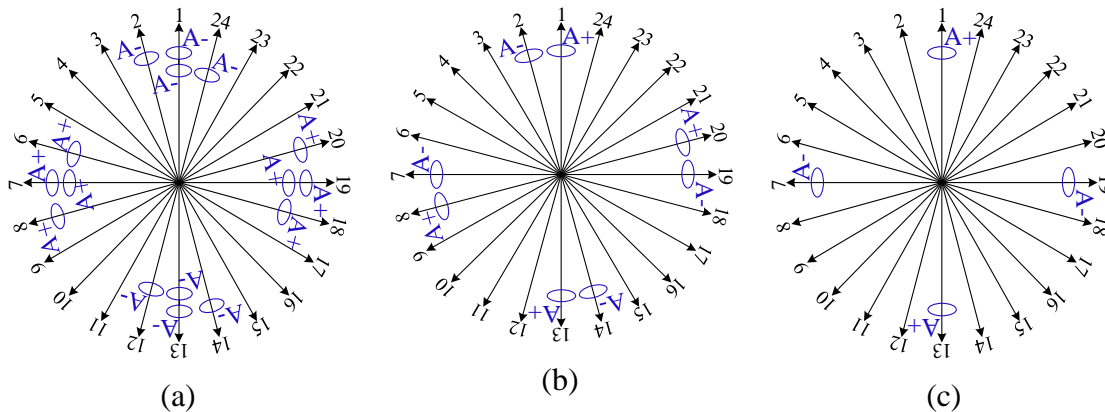
Fig. 4.5 Armature winding design. (a) 2-pole-pair distributed design. (b) 10-pole-pair concentrated design. (a) 2-pole-pair concentrated design.

In the proposed machine, a single-layer concentrated armature winding is utilized to couple triple flux modulation effect. To illustrate its reasonability, three possible winding designs are compared. For 24-slot 22-pole design case, 2-pole-pair distributed armature winding, 10-pole-pair double-layer concentrated winding, and 2-pole-pair single-layer concentrated winding are considered, as presented in Fig. 4.5.
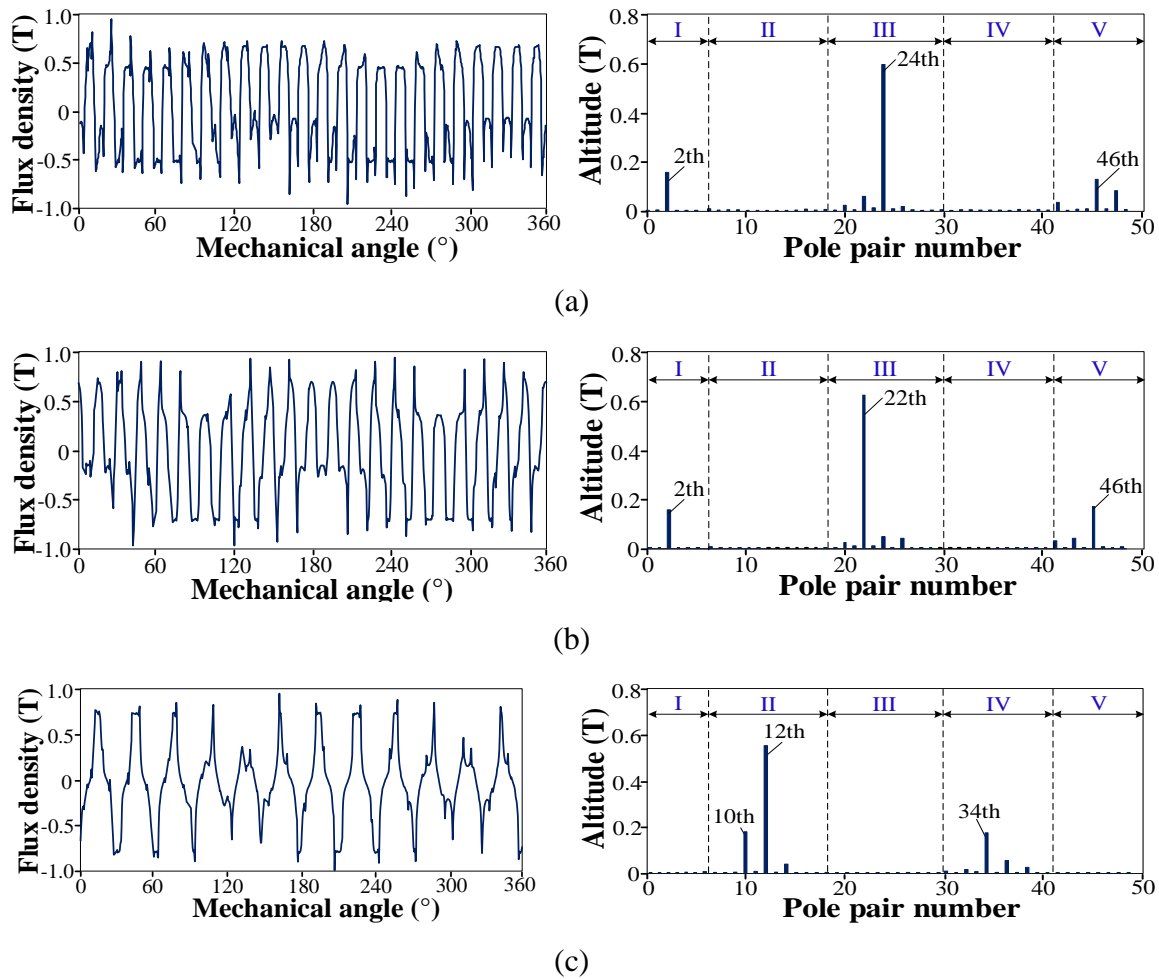
Fig. 4.6 Excited flux density by excitation sources and corresponding harmonics distribution. (a) Slot PM source. (b) Rotor PM source. (c) DC field source.

The excited air gap flux density by three excitation sources and three different armature windings, are predicted by finite element analysis and presented in Fig. 4.6 and Fig. 4.7, respectively. It is shown the 2-pole-pair distributed winding can only be synchronous with dual PM sources within harmonics region I, III and V, and the 10-pole-pair double-layer concentrated winding can only be synchronous with the DC field source within harmonics region II and IV. However, the 2-pole-pair single-layer concentrated armature winding can be synchronous with both dual PM sources and DC field source, benefiting from its harmonics diversity, thus it is adopted in the proposed machine.
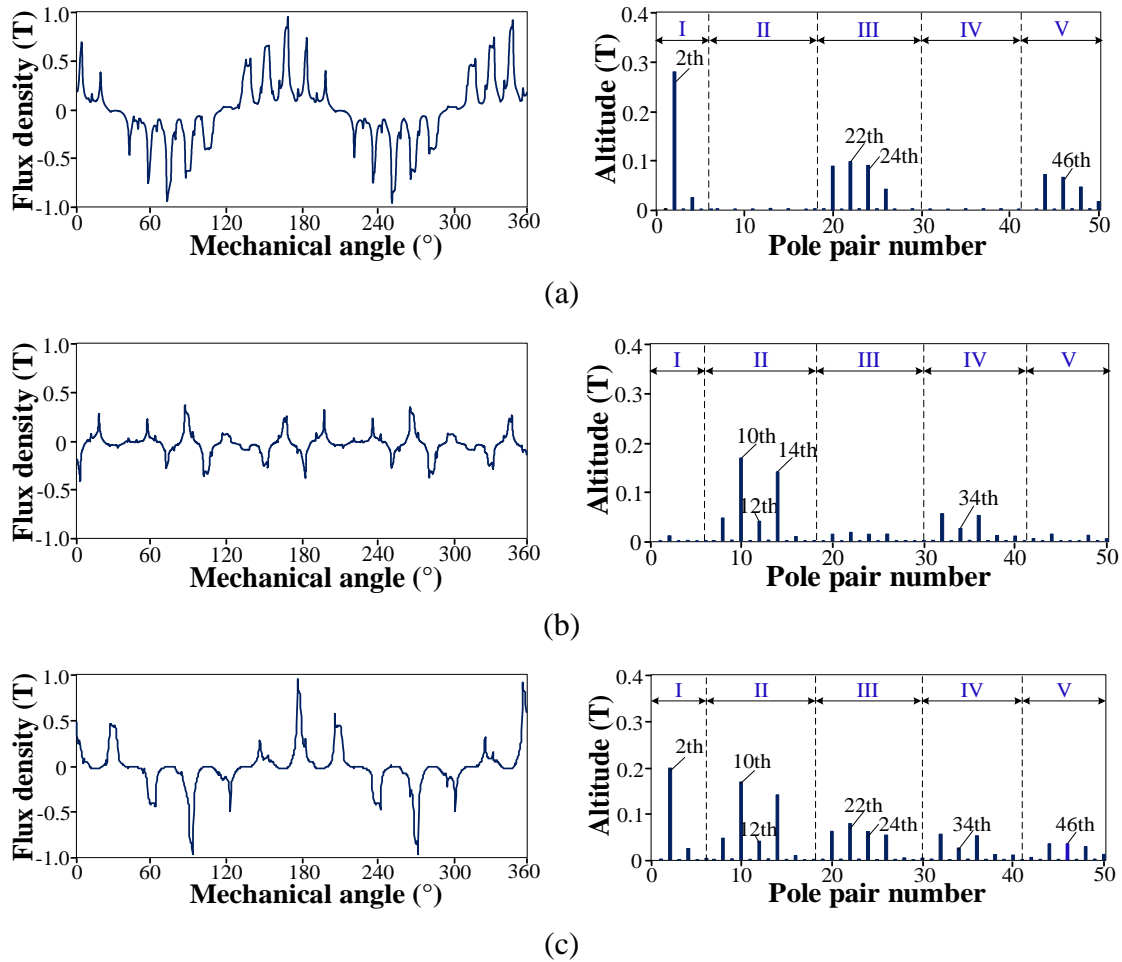
Fig. 4.7 Excited flux density by armature windings. (a) 2-pole-pair distributed. design (b) 10-pole-pair concentrated design. (c) 2-pole-pair concentrated design.

It should be pointed out, torque generation with 2-pole-pair single-layer concentrated armature winding may be relatively sacrificed compared to that of 2-pole-pair distributed winding, caused by reduced winding factor. However, extra DC flux weakening ability is equipped with this concentrated winding. Therefore, not only i_d armature current, but also DC field current can be used for enhanced flux weakening operation.

4.4 TORUQE COMPONENT QUATIFICATION

To quantitatively investigate the torque component produced by each air gap harmonic, the winding factor can be calculated as

$$\begin{cases} k_{pn} = \cos(\varepsilon_n/2) \\ k_{dn} = \dfrac{\sin(m\gamma_n/2)}{m\sin(\gamma_n/2)} \\ k_{wn} = k_{pn}k_{dn} \end{cases} \tag{4.5}$$

where k_{pn} is the pitch factor. k_{dn} is the distribution factor. k_{wn} is the winding factor. m is the coil number per pole per phase. γ_n is the slot angle. ε_n is the angle by which coils are short-pitched. For each harmonic, γ_n and ε_n can be calculated by

$$\begin{cases} \gamma_n = \dfrac{360}{N_s} PPN_{m,k} \\ \varepsilon_n = 180 - \gamma c \end{cases} \tag{4.6}$$

where c is the coil pitch value. Further, the induced back EMF by each harmonic component can expressed as

$$E_{phn} = \frac{4.44DLT_{ph}}{60}(B_n k_{wn}\omega_n) \tag{4.7}$$

where D is the diameter of air gap circumference. L the stack length. T_{ph} is the turn number of one phase winding, B_n is the amplitude of nth harmonic flux density. ω_n is the rotational speed of nth harmonic component.

The final amplitude of back EMF can be deduced as

$$E_{ph} = \sqrt{\sum E_{phn}^2}, \; n{=}1,2,3...... \tag{4.8}$$

Based on the above analytical method, contribution of each harmonic on back EMF can be calculated as listed in Table 4.3 and Table 4.4, respectively, in which the amplitude of each EMF component can be characterized by the product of B_n, k_{wn} and ω_n, considering the proportional relation as shown in Equ.(4.7).

TABLE 4.3 Harmonics Contribution on Back EMF of Stator PMs

Order	PPN	B_n	k_{wn}	ω_n	EMF (*)
p_s	24	0.58	0	0	0
$|p_s\text{-}p_k|$	2	0.13	0.26	$11\omega_r$	$0.372\omega_r$
p_s+p_k	46	0.11	0.26	$0.48\omega_r$	$0.014\omega_r$
$3p_s$	72	0.10	0	0	0

TABLE 4.4 Harmonics Contribution on Back EMF of Rotor PMs

Order	PPN	B_n	k_{wn}	ω_n	EMF (*)
p_s	22	0.65	0.26	ω_r	$0.169\omega_r$
$|p_s\text{-}p_k|$	2	0.14	0.26	$11\omega_r$	$0.401\omega_r$
p_s+p_k	46	0.16	0.26	$0.48\omega_r$	$0.019\omega_r$
$3p_s$	66	0.11	0	ω_r	0

It can be found, the contribution of harmonics excited by flux modulation effect, are basically balanced for dual PM sources. However, for stator PMs, its fundamental harmonic and third-order harmonic cannot generate effective back EMF due to zero winding factor and zero rotation speed, while for rotor PMs, its fundamental harmonic can also make contribution to back EMF generation. Therefore, it is revealed that rotor PMs essentially have a stronger ability to generate back EMF than stator PMs.

4.5 FINITE ELEMENT ANALYSIS

To verify the validity of the proposed design, a finite element model is established. Some general dimension parameters of the proposed topology are denoted in Fig. 4.8, including the machine outer diameter, stack length, air gap length, and other dimension parameters. Their corresponding design values are given in Table 4.5.
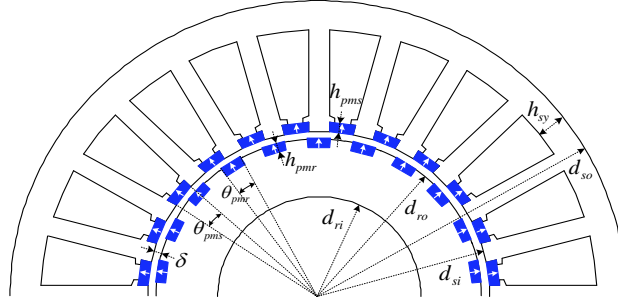
Fig. 4.8 Some general dimension parameters.

TABLE 4.5 General Dimension Parameters of the Proposed Machine

Symbol	Parameter	Unit	Value
d_{so}	Outer diameter of the stator	mm	120
d_{si}	Inner diameter of the stator	mm	69
d_{ro}	Outer diameter of the rotor	mm	68.5
d_{ri}	Inner diameter of the rotor	mm	20
δ	Air gap length	mm	0.5
l	Stack length	mm	50
h_{sy}	Height of stator yoke	mm	5
h_{pms}	Height of stator-slot PM	mm	1.8
h_{pmr}	Height of rotor PM	mm	2.2
θ_{pms}	Arc of stator-slot PM	°	8
θ_{pmr}	Arc of rotor PM	°	8

4.5.1 Flux Distribution and Torque Performance

In the proposed topology, the stator PMs are arranged in the slot openings. Usually, such a high-reluctance design is not able to produce effective torque. Therefore, in the existing solutions, stator PMs are usually arranged with convention modes such as mounting on the stator teeth. In this paper, a fair comparison is performed between the proposed topology with stator-slot PMs and the existing topology with stator-teeth PMs in terms of their torque

density. Two machines share the same design except for arrangement modes of stator PMs. The no-load flux distribution excited by only stator PMs and rotor PMs for two machines, are presented in Fig. 4.9 and Fig. 4.10, respectively. One can see, in the existing topology, the no-load flux distribution excited by dual PM sources are entirely different, while in the proposed design, they are almost the same due to symmetrical flux modulation effect.

(a)   (b)
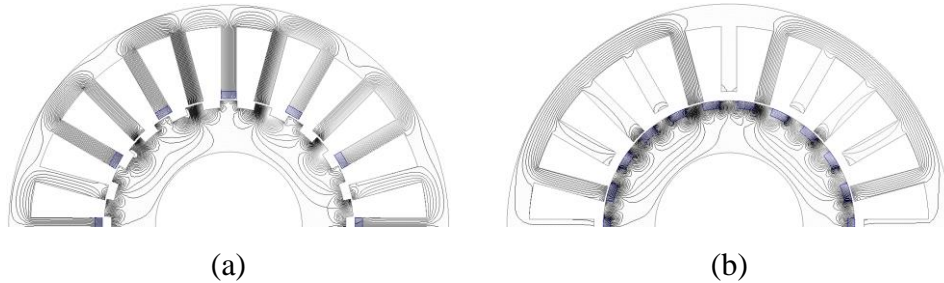
Fig. 4.9 No-load flux distribution of the existing topology with stator-teeth PMs. (a) Excited by stator-teeth PMs. (a) Excited by rotor PMs.

(a)   (b)
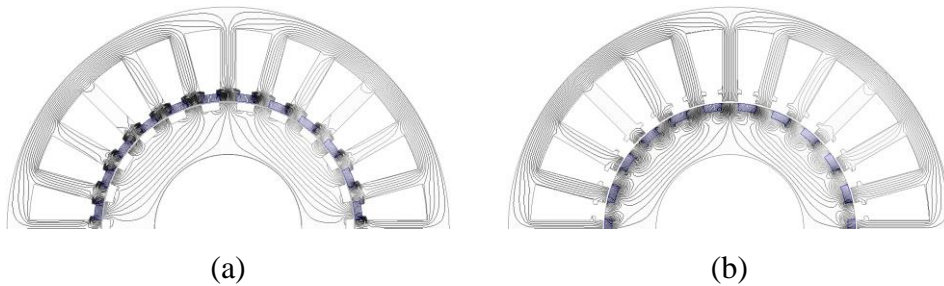
Fig. 4.10 No-load flux distribution of the proposed topology with stator-slot PMs. (a) Excited by stator-slot PMs. (a) Excited by rotor PMs.

Further, four finite element models with different PM volumes are built as in Fig. 4.11. Models in Fig. 4.11(a) and (b) have the same PM volume at both stator and rotor sides. Their steady torque is calculated as given in Fig. 4.12(a) and (b), respectively. It can be found, the torque components excited by rotor PMs are almost the same in two different topologies. However, the torque component excited by stator PMs in the proposed topology, is 20.2% larger than that in the existing topology, due to symmetrical flux modulation effect. Therefore, the proposed topology owns a 13.4% higher synthesis torque density.

Then, models in Fig. 4.11(c) and (d) doubles the stator PM volume and corresponding steady torque is calculated in Fig. 4.12(c) and (d), respectively. It can be found, in the existing topology, when the stator PM volume is doubled, the torque component excited by stator-teeth PMs is instead reduced from 1.68Nm to 1.59Nm, while that in the proposed topology is slightly increased from 2.02Nm to 2.45Nm. Therefore, the stator PMs in existing topology is more easily to be saturated, compared to the propose topology.

(a)　　　　　　(b)　　　　　　(c)　　　　　　(d)
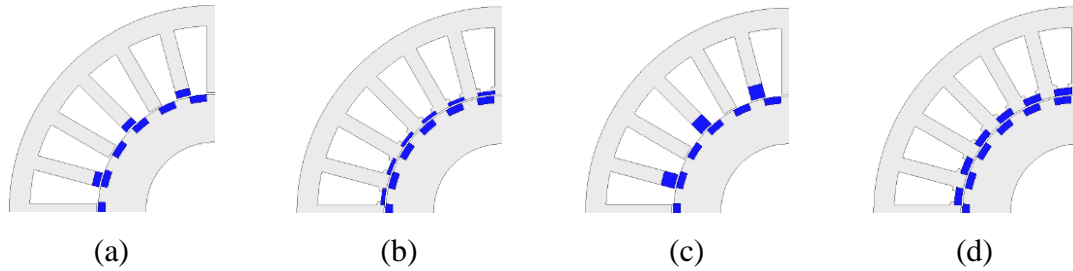
Fig. 4.11 (a) Existing, stator PM 5057 mm^3, rotor PM 10595 mm^3. (b) Proposed, stator PM 5057 mm^3, rotor PM 10595 mm^3. (c) Existing, stator PM 10114 mm^3, rotor PM 10595 mm^3. (d) Proposed, stator PM 10114 mm^3, rotor PM 10595 mm^3.

(a)　　　　　　　　　　　　　(b)

(c)　　　　　　　　　　　　　(d)
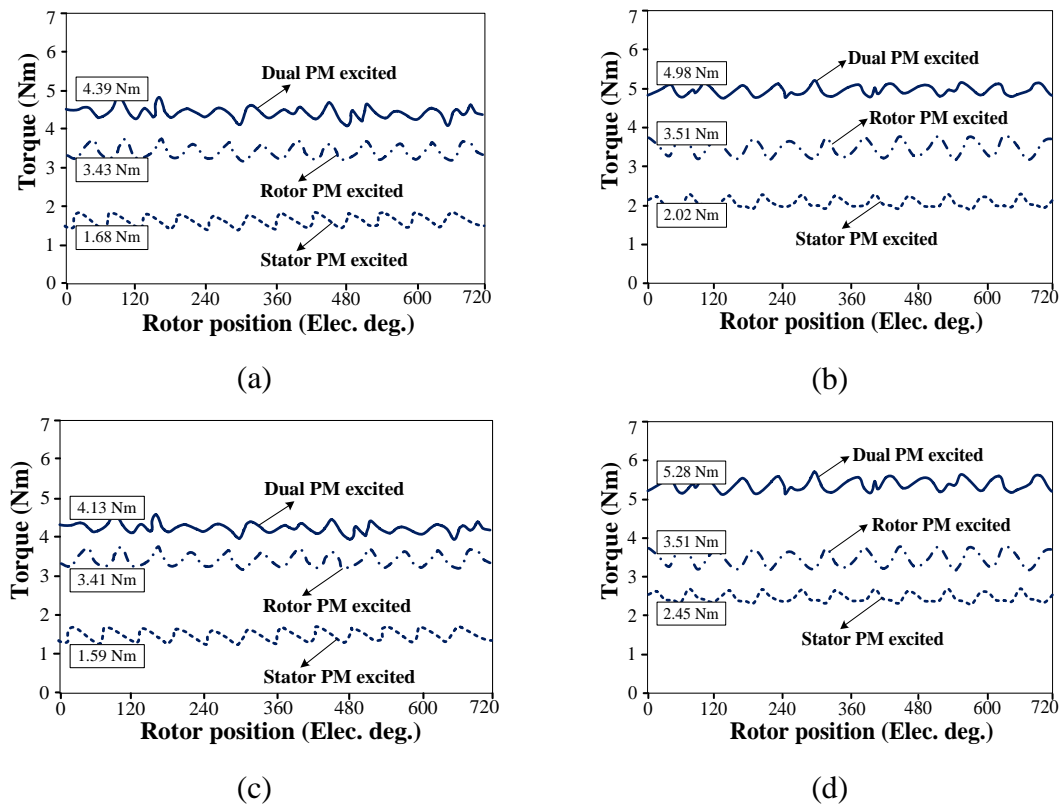
Fig. 4.12 Steady torque of above four models with 6A/mm^2 current density.
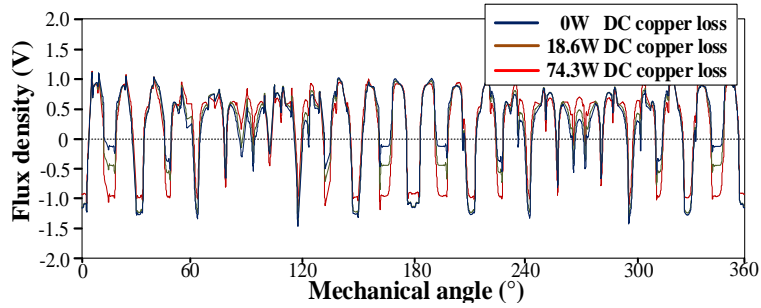
(a)
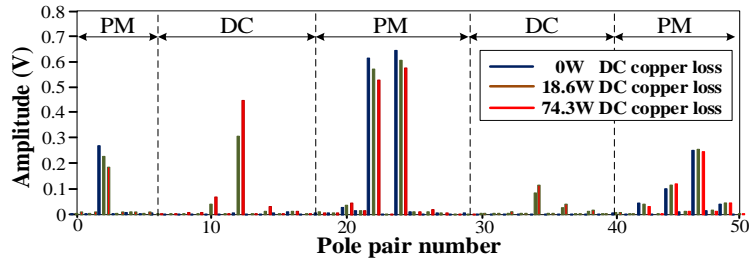
(b)

Fig. 4.13 (a) No-load air gap flux density against different DC field excitation. (b) Variation of harmonics distribution.
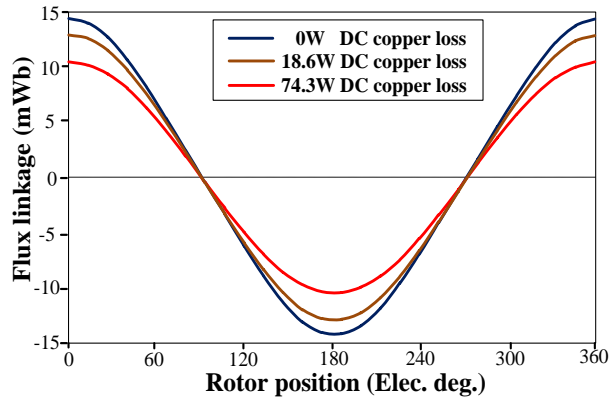
Fig. 4.14 On-load armature flux with 18.6W AC copper loss.

4.5.2 Flux Weakening Effect

To verify its flux regulation ability, the dual-PM-excited air gap flux density during field current regulation is calculated and presented in Fig. 4.13, with its harmonics distribution obtained by using FFT analysis. One can see, by injecting different DC field current,

altitudes of the air gap harmonics in different working regions can be continuously regulated, and correspondingly, an effective flux regulation can be achieved at armature terminal as shown in Fig. 4.14, in which the AC current density is fixed at 6A/mm^2, while DC current density varies from 0 to 6, and then to 12A/mm^2. Little phase shift or distortion exists during field current regulation. It is proved this single-layer concentrated winding not only interact with dual PM sources for the torque contribution, but also can effectively couple DC field source to provide additional flux weakening ability.

4.5.3 Demagnetization Risk

PM demagnetization is one of the leading restrictions for flux weakening and overload operations. In general, the working point of rare earth PMs is influenced by both current demagnetizing force and temperature. When current density increases, the working point of PMs will decrease until a knee point at which irreversible demagnetization occurs. The knee point for NdFeB35 type PMs is 0.33T at 160°C.

In this thesis, two working conditions are considered for most possible demagnetization risk. Firstly, when a 2-times overload torque is needed at the rated speed, in which the current density of AC armature excitation increases from 6A/mm^2 to 12A/mm^2 and DC field excitation maintains at zero since no flux weakening is needed, corresponding flux density distribution is calculated and presented in Fig. 4.15. It can be noticed that the most possible demagnetization position for the proposed topology, is located at the rotor PM side as cycled in Fig. 4.15(a), while in the existing topology as given in Fig. 4.15(b), both stator and rotor PM suffer from demagnetization risk. Further, when the machine operates over rated speed and a flux weakening operation is applied, in which the AC armature excitation is 6A/mm^2 and the DC field excitation is 12A/mm^2 for deep flux weakening,

corresponding flux density is calculated and presented in Fig. 4.16. It can be seen, for the proposed topology, the most demagnetization position still locates at rotor PM side, while for the existing topology, the stator PMs are most likely to be demagnetized.

In general, in the proposed topology, demagnetization risk for stator PMs is effectively mitigated and thus only rotor PM is needed to consider demagnetization during design stage. The reason is that in the proposed topology, stator PMs are arranged in the slots, thus armature flux will not directly pass through slot PMs, which is different from that in the existing topology with PMs mounted on the stator teeth.

(a)   (b)
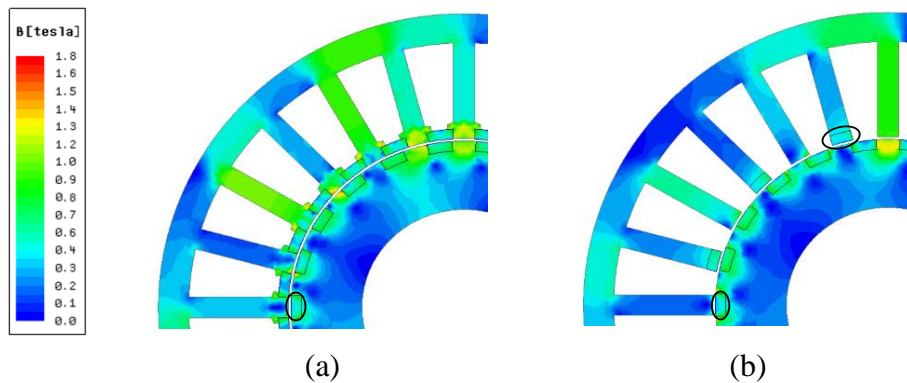
Fig. 4.15 Flux density at 200% overload condition, AC current density 12A/mm^2 and DC current density 0A/mm^2. (a) Proposed topology. (b) Existing topology.

(a)   (b)
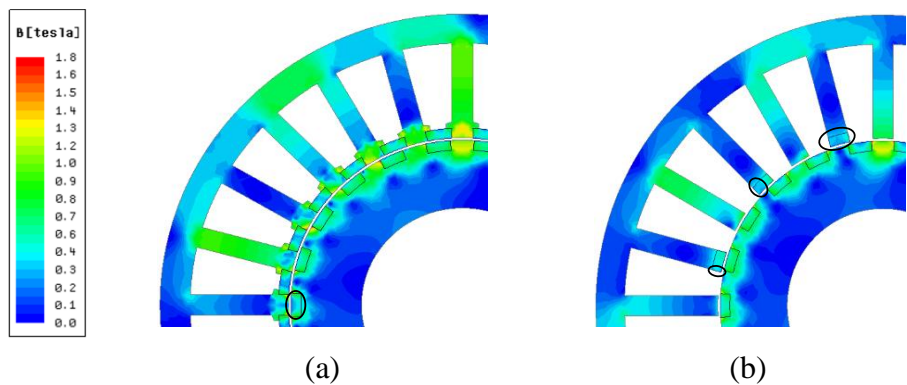
Fig. 4.16 Flux density at deep flux weakening status, AC current density 6A/mm^2 and DC current density 12A/mm^2. (a) Proposed topology. (b) Existing topology.
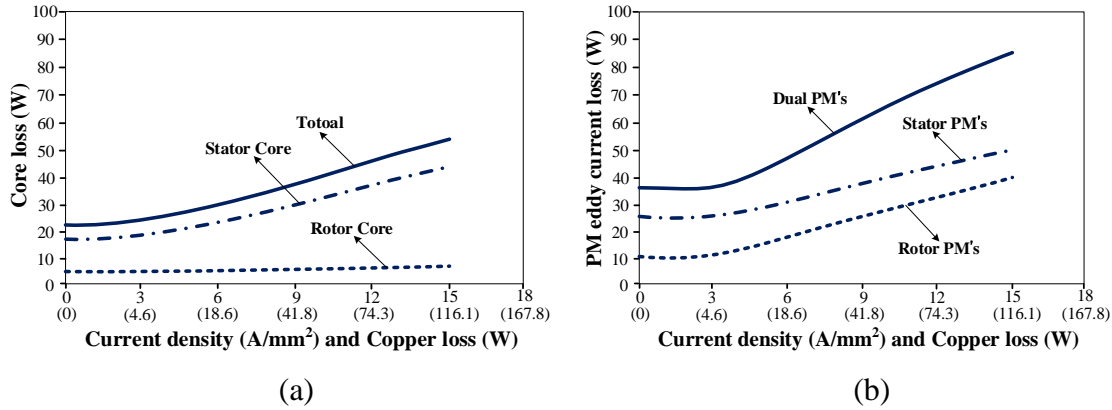
Fig. 4.17 Loss at speed 1000rpm. (a) Core loss. (b) PM eddy current loss.
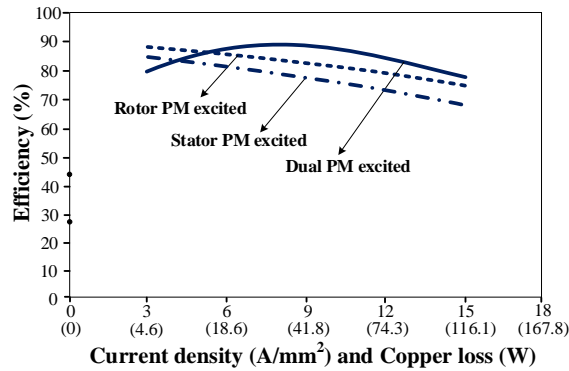
Fig. 4.18 Efficiency at different excitation status at speed 1000rpm.

4.5.4 Loss and Efficiency

Further, the loss distribution and efficiency are evaluated for the proposed topology at rated speed 1000rpm. As presented in Fig. 4.17(a), although the proposed topology uses a consequent-pole rotor structure, the rotor core loss is still much smaller than stator core loss, which is similar with traditional PM machines. With the increasing of armature current density, the stator core loss and total core loss almost linearly increases. The reason is this consequent-pole rotor structure leads to a relatively larger magnetizing inductance, hence the changing of current density has a greater influence on the working point of core components. The eddy current loss for both stator and rotor PMs are further calculated and

plotted in Fig. 4.17(b). It can be noticed that the total PM eddy current loss is even larger than total core loss at the same condition. The stator-slot PMs has larger eddy current loss that of rotor PMs. The reason is that stator PMs are placed at slot openings, which leads to a larger variation of its working point from open circuit situation to active situation. Finally, the rated efficiency is evaluated at different excitation status as shown in Fig. 4.18. With a single PM source active, the rotor-PM-excited topology has a higher efficiency than stator-PM-excited topology regardless of load conditions. When dual PM sources are both active, efficiency is reduced at light-load condition due to enlarged core loss and PM eddy current loss. However, better efficiency is observed when current density exceeds 5.5A/mm^2 for the proposed topology compared to single-excited design.

4.5.5 Power Factor

Power factor (PF) is one of the leading factors to determine the capability of inverter, which can be defined as

$$PF = \frac{E_0^2}{\sqrt{E_0^2 + X_q^2 I_q^2}} = \frac{1}{\sqrt{1 + (\frac{X_q I_q}{E_0})^2}} \tag{4.9}$$

where E_0 refers to the no-load phase induced voltage, X_d refers to the q-axis synchronous reactance, and I_d is the q-axis current.

By measuring the phase difference between induced voltage and load current, PF of the proposed machine is evaluated under different excitation status as presented in Fig. 4.19. It can be seen, with the increase of armature current, PF accordingly declines due to the enhancement of armature reaction. In general, the PF performance at dual-PM-exited status, is better than that at only rotor-PM-exited or stator-PM-exited status. The reason is the introduction of stator PM source into slot openings, contributes to a higher induced voltage

E_0 , while X_q maintains unchanged since slot PMs will not change armature reaction. However, PF of this new topology is still not comparable to that of industrial PM machines for relatively large X_q caused by flux modulation mechanism.
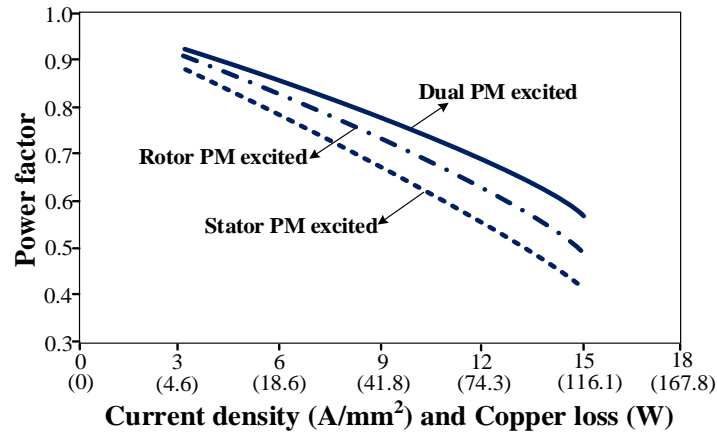
Fig. 4.19 Power factor at different excitation status.

4.6 DESIGN GUIDELINE

4.6.1 Slot Pole Combination

The slot pole combination usually has a leading influence on machine performance. In flux-modulated machines, the number of rotor pole pairs is usually chosen to be close to the stator teeth number to achieve a relatively big pole ratio and torque density. In this paper, four slot pole cases, 24/20, 24/22, 24/26 and 24/28, are considered for optimization and comparison. Some design parameters and comparative results are given in Table 4.6. It can be found, although the 24-slot 20-pole case provides the largest rated torque, its cogging torque is much larger than other three cases. If the cogging torque to rated torque ratio is determined as the comparison index, the 24-slot 22-pole case is the optimal solution, whose cogging torque ratio is only about 3.8%.

TABLE 4.6 Comparison of Different Slot Pole Combinations

Number of stator slots	24	24	24	24
Number of rotor poles	20	22	26	28
PPN of field excitation	12	12	12	12
PPN of stator-slot PMs	24	24	24	24
PPN of rotor PMs	20	22	26	28
PPN of armature windings	8	10	14	16
Wingding factor	0.866	0.966	0.966	0.866
Cogging torque (Nm)	0.74	0.21	0.23	0.64
Rated torque (Nm)	5.93	5.52	5.11	4.96
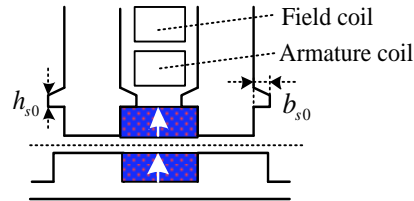
Fig. 4.20 Model of one stator slot with pole shoes for PM support.
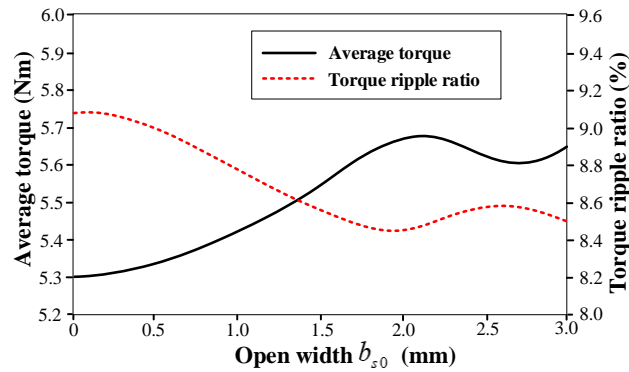
Fig. 4.21 Influence of open width of extra pole shoes on torque performance.

4.6.2 Mechanical Support for Slot PMs

One of the features in the proposed design is the use of stator-slot PMs, which accordingly brings a mechanical issue to house them and avoid possible movement with a continuous rotation. In this chapter, as shown in Fig. 4.20, extra pole shoes are designed

with each stator tooth to provide a mechanical support for slot PMs. With this design technique, the stator PMs can be simply mounted and fixed in slot openings, similar with the process of mounting PMs in rotor slots. Further, the influence of this extra mechanical design on machine electromagnetic performance is also evaluated. The height of pole shoes is fixed as 1mm in this paper. Then, the open width parameter is analyzed and its effect on torque performance is presented in Fig. 4.21. One can see, this extra pole shoe generally provides a positive effect on torque density enhancement and ripple ratio mitigation. The reason is that extra pole shoes provides a certain reluctance reduction for slot PM magnetic circuit. Therefore, in general, design of extra pole shoes is proved to be an effective approach to provide both slot PM support and torque performance improvement.

(a)   (b)
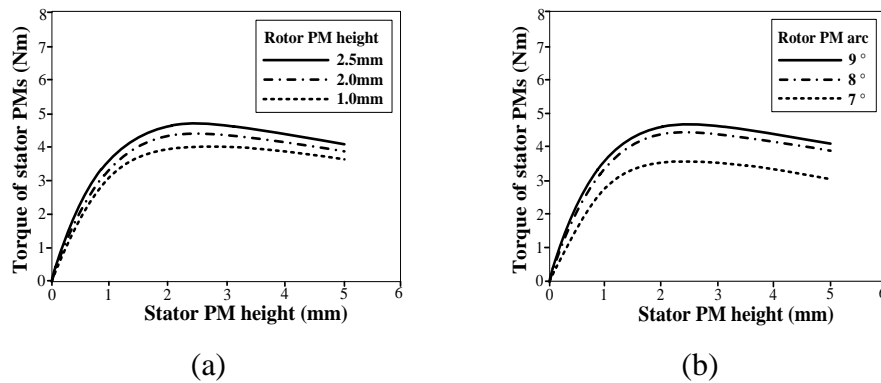
Fig. 4.22 Influence of rotor PM parameters on torque of stator PMs.

(a)   (b)
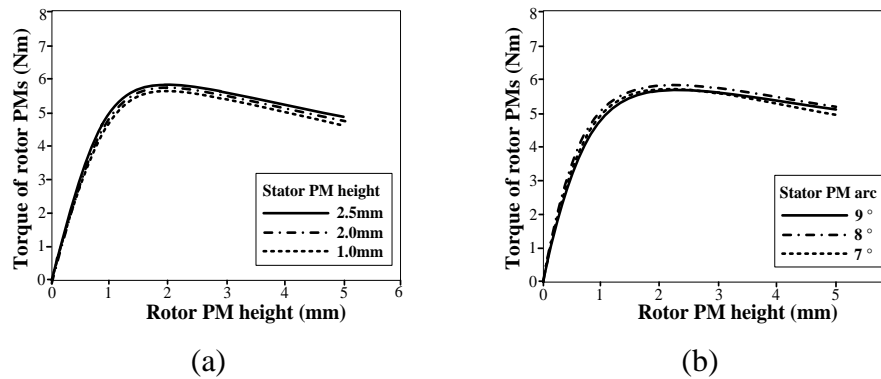
Fig. 4.23 Influence of stator PM parameters on torque of rotor PMs.

4.6.3 PM Split Ratio

The mutual influence of dimension parameters between dual PM sources on torque components is evaluated. As shown in Fig. 4.22, the torque contribution of stator PMs is closely related to the dimension parameters of rotor PMs. This is because, flux modulation effect of stator PMs depends on the rotor permeance variation, in which dimension parameters of rotor PMs are the leading influence factors. In contrast, as shown in Fig. 4.23, torque contribution of rotor PMs is almost not influenced by dimension parameters of stator PMs. This asymmetrical influence between dual PMs should be considered at design stage.

As analyzed above, on one side, rotor PMs essentially have stronger ability in torque generation compared with stator PMs. On other side, torque contribution of stator PMs is unilaterally influenced by design parameters of rotor PMs. Therefore, rotor PMs should be determined with higher design priority. Based on this principle, a design guideline is further presented for determining the PM usage in the proposed topology, as shown in Fig. 4.24.
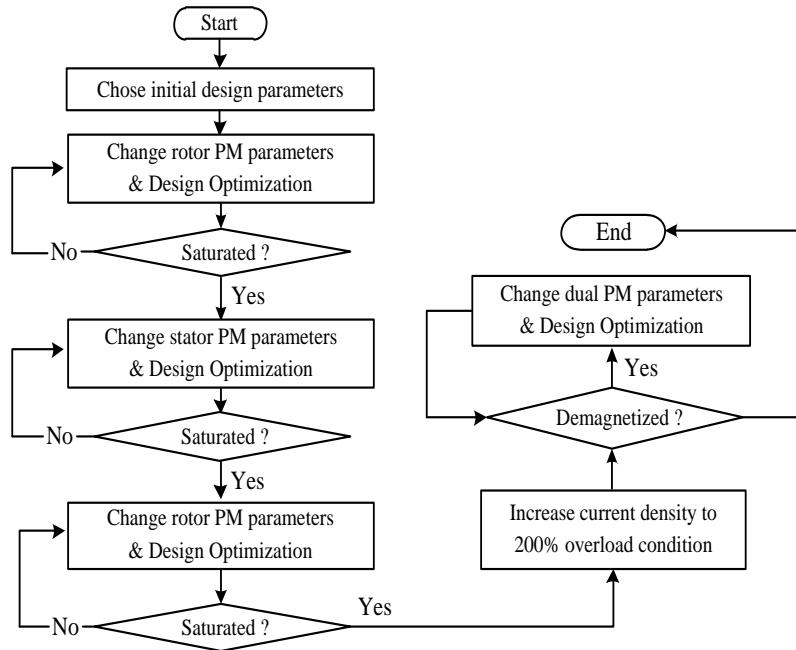
Fig.4.24 Flow chart of a general design procedure for DPMVM.

100

(1) Chose initial dimension parameters.

(2) Remove stator PMs. Change dimension parameters of rotor PMs including its height and arc, and meanwhile optimize other dimension parameters, until the torque component generated by rotor PMs arrives a saturation point. The saturation condition is defined as the point at which increasing PM volume will not increase torque

(3) Fix rotor PM parameters. Change dimension parameters of stator PMs and optimize other dimension parameters, until the torque of stator PMs arrives a saturation point.

(4) Fix stator PM parameters. Change dimension parameters of rotor PMs again to enhance the torque component of stator PMs, optimize other dimension parameters until the synthetic torque arrives a global saturation point.

(5) Check demagnetization of dual PMs at overload condition. If no risk, end. If risk exists, change PM dimension parameters until the demagnetization risk is eliminated.

TABLE 4.7 Specifications and Materials of Prototype

Specifications		Materials		
Rated speed	1000 rpm		Type	NdFeB35
Rated Phase voltage	22 V	PMs	Remanence	1.2 T
Rated power	612 W		Coercive force	915 kA/m
Peak Power	1153 W		Type	MG19_24
Phase inductance	0.98 mH	Steels	Saturated point	1.8 T
Phase resistance	0.043 Ω		Mass density	7650 kg/m^3

4.7 EXPERIMENTAL VERIFICATION

To verify the feasibility of the proposed machine, a prototype is built with relevant specifications and materials listed in Table 4.7. The stator laminations are designed with

extra stator pole shoes for slot PM support as shown in Fig. 4.25(a), (b) and (c) present the stator assembly and rotor assembly. With a single-layer concentrated armature winding, the process of wire wrapping is simplified and good electromagnetic isolation is obtained between phases. Two set of PMs are mounted at both stator and rotor sides. A test bed is further established in Fig. 4.26. Relevant tests are performed as follows.

(a)　　　　　　　　(b)　　　　　　　　(c)
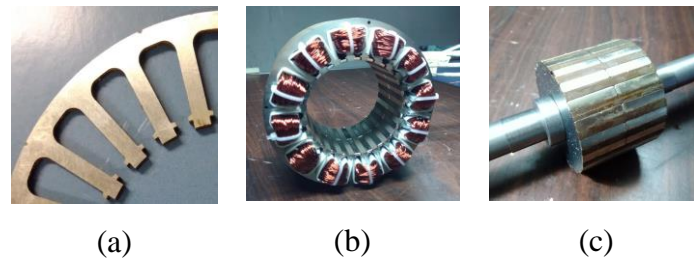
Fig. 4.25 Protype details. (a) Stator lamination. (b) Stator assembly. (c) Rotor assembly.
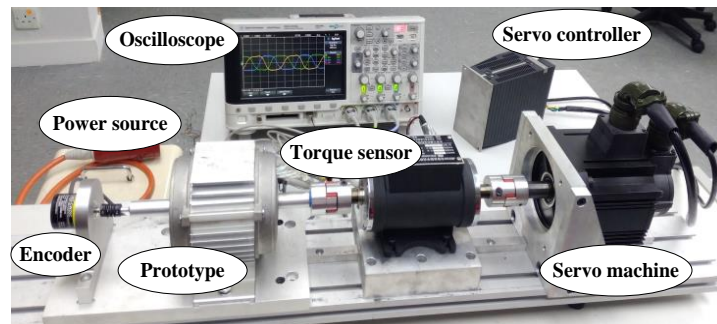
Fig. 4.26 Experimental platform based on the assembled prototype.

The no-load back-EMF is measured and plotted in Fig. 4.27(a), at 1000rpm without DC field excitation. The three-phase back EMF is balanced. And its altitude is about 21V, which basically agrees with finite element predication. A little distortion caused by higher-order harmonic components is observed in Fig. 4.27(b), which is due to the fabrication tolerance such as an uneven magnetization of PM materials. By collecting the altitude of back EMF against different DC excitation, the field regulation ability is measured and given in Fig. 4.28. One can see, the measured trend agrees well the FEA predication.

(a)

(b)
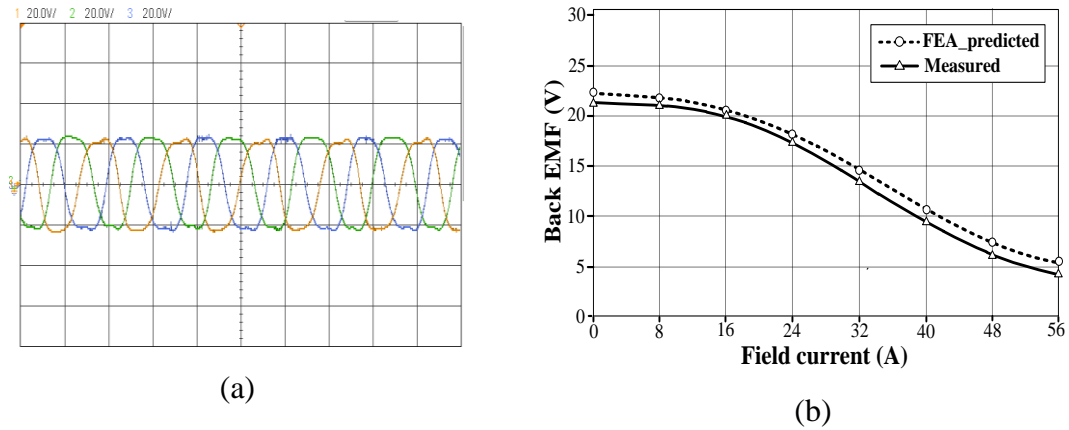
Fig. 4.27 (a) Measured no load back EMF. (b) Back EMF against DC field excitation.
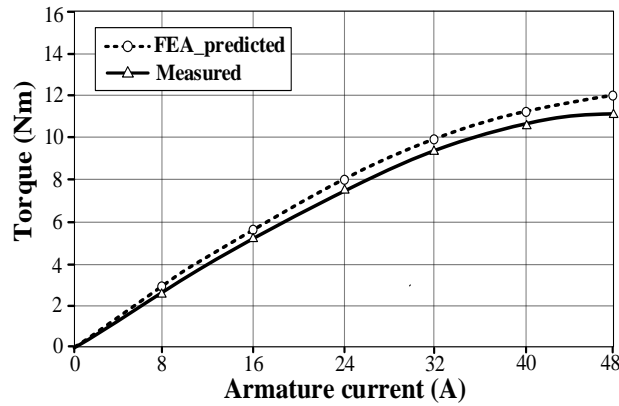
Fig. 4.28 Torque capacity curve.

Further, its torque capacity is tested as plotted in Fig. 4.28. With rated armature current 17A applied, the measured torque is about 5.8 Nm, which is in line with FEA predication. Meanwhile, about a 2-times peak torque can be obtained under overload situation. The torque speed curve is measured with different DC field excitation as plotted in Fig. 4.29. The base speed is 1000 rpm and The DC bus voltage supplied is 48V. It can be seen, when the machine operates over base speed and enters high-speed region, higher output torque is obtained by flux weakening operation. The reason is, by extra DC flux weakening, smaller i_d current is needed for flux weakening, thus under the same inverter current rating, larger i_q current can be allowed to produce torque in high-speed region.
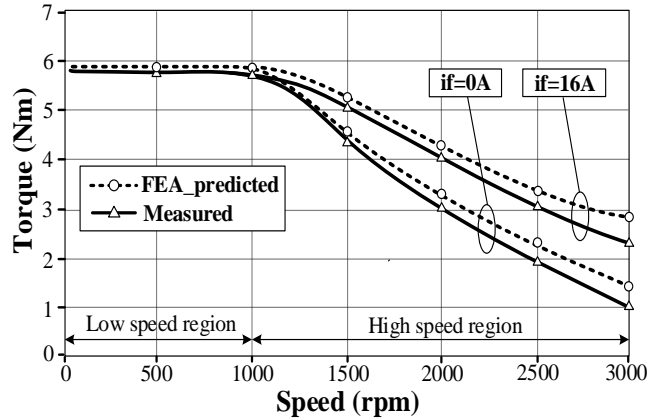
Fig. 4.29 Torque speed curves against different DC field excitation.

(a)

(b)
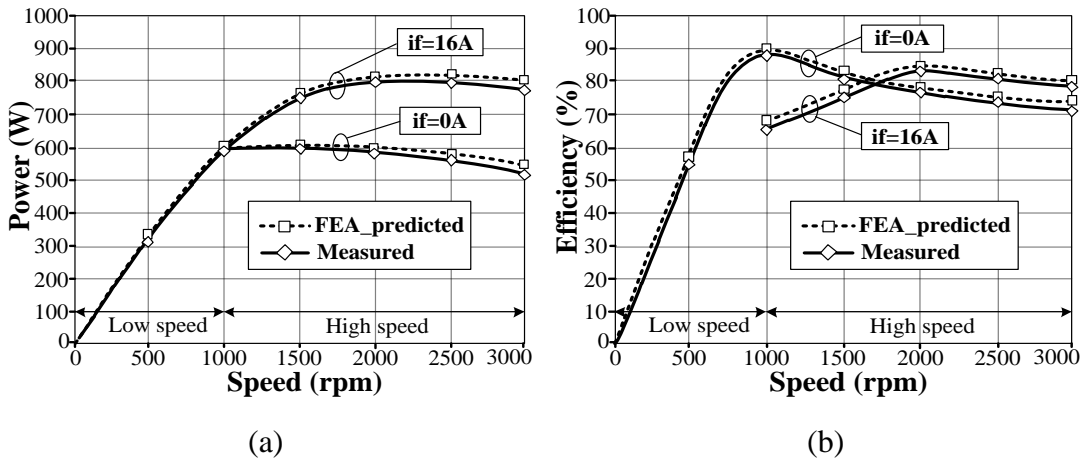
Fig. 4.30 Power and efficiency curves against different DC field excitation. (a) Power

speed curves. (b) Efficiency speed curves.

Finally, the output mechanical power and machine efficiency are evaluated and plotted

in Fig. 4.30(a) and Fig. 4.30(b), respectively. The power contribution of DC field excitation

is relatively weak due to the saturation effect of stator core, thus is recommended to be not

applied in the low-speed region. However, in the high-speed region, the negative DC field

excitation contribute to both enhanced output power and efficiency performance due to the

effective flux weakening operation, thus proving the feasibility of the proposed HE-DPMM

and its potential for EV/HEV wide-speed driving applications.

4.8 CONCLUSION

This chapter proposes a novel parallel hybrid excitation dual PM machine topology with triple flux modulation effect, which owns advantages of a compact and brushless structure, boosted torque density, improved flux weakening ability and reduced demagnetization risk. The key is by utilizing the harmonics diversity of a single-layer concentrated armature winding to effectively couple triple flux modulation effect excited by stator slot PMs, rotor PMs and DC field coils, which have entirely different pole pair numbers. The proposed topology and its design mechanism are both introduced, with its feasibility verified by both finite element analysis and prototype experiments. The features of this new topology are summarized as (1) With a new layout of slot PM source, the flux modulation effect of dual PM sources becomes symmetrical. Therefore, the proposed machine owns a higher torque generation at stator side, compared to that of the existing dual PM counterpart. Accordingly, the torque density of this new topology is more advantageous. (2) Benefiting from the harmonics diversity of a single-layer concentrated winding, the flux modulation effect of DC field source is integrated for flux weakening operation. This is a new perspective for flux weakening in dual PM machines, since in existing counterparts, flux weakening is realized by controlling stator PMs based on magnetic circuit observation. Moreover, the demagnetization risk for stator slot PMs is avoided due to parallel magnetic circuit. (3) The rich flux harmonics in the proposed machine leads to the non-negligible PM eddy current loss, which should be carefully evaluated during design stage. Ferrite magnets with much lower conductivity can be considered as an alternative solution. Meanwhile, although the power factor in the proposed machine is improved due to enhanced PM EMF, it is still not comparable to conventional PM machine and needs further improvement.

CHAPTER 5. PROPOSED HYBRID EXCITATION DUAL PM MACHINE WITH RELIEVING-DC-SATURATION STRUCTURE FOR HEV STARTER GENERATOR APPLICATION

5.1 INTRODUCTION

Starter generator (SG) integrated design is an effective method to realize hybrid energy strategy for HEVs [102]. The SG solution presented in literature usually adopts parallel architectures, which can be divided into two categories, namely the integrated starter generator (ISG) and belt-driven starter generator (BSG) [103-104]. ISG is inserted into the engine and needs a completely revised housing, while BSG as shown in Fig. 5.1, needs less modification of engine layout and thus becomes more cost-effective.
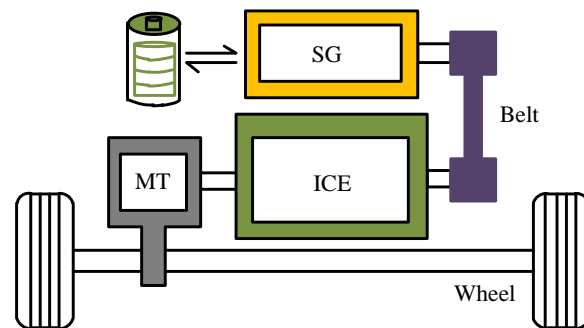
Fig. 5.1 Configuration of BSG system in HEV. (MT—mechanical transmission, ICE—internal combustion engine, SG—starter generator).

Electrical machine is the core of SG system and a variety of topologies have been studied and implemented as SG in HEVs. Induction machine (IM) is one of the popular SG candidates due to its low cost, robust structure, high overload ability and good flux weakening characteristic [105-107]. However, IM suffers from relatively low efficiency and power factor. Besides, its control strategy for wide-speed generation is complicated.

Permanent magnet (PM) synchronous machine (PMSM) is an attractive SG solution due to high torque density and high efficiency [108-110]. However, PMSM has drawbacks such as high cost, poor flux weakening ability and thus limited constant power speed range. Switched reluctance machine (SRM) is another SG candidate, which owns the merits of low cost and high reliability [111-113]. However, the severe torque ripple in SRM results in implicative engine vibration, which is a critical issue in SG system.

Hybrid-excited machine (HEM) is another emerging solution for SG system [114-115]. A typical rotor-PM HEM is investigated as SG for aerospace propulsion [116]. It utilizes a magnetic-shunt rotor structure, in which the rotor core is extended in axial direction to artificially produce axial magnetic circuit for PMs. Besides, DC field coil is housed in the extended rotor cavity for magnetic field regulation. In this way, it realizes a brushless configuration. However, its mechanical structure becomes very complicated, which is not attractive for SG system considering the robustness and cost. Meanwhile, since the space for SG in HEV is limited, using magnetic-shunt rotor leads to torque sacrifice. In [117], a typical stator-PM HEM SG is explored. It owns a simple and brushless structure. However, as a common issue in stator PM machines, its torque density is disadvantageous.

This chapter proposes a new relieving-DC-saturation hybrid Dual PM machine, which integrates good torque density and bidirectional flux regulation within a simple and brushless structure. The key is to artificially construct reluctance effect in a consequent-pole Vernier PM machine by introducing extra DC field excitation equipped with relieving-DC-saturation ability. In this way, the advantages of bidirectional flux control in stator-DC-excited reluctance machine and good torque density in CP-VPMM are well combined, making this new topology suitable for multi-mode starter generator application.

5.2 SG SYSTEM BASED ON THE PROPOSED MACHINE

5.2.1 Machine Construction

Fig. 5.2 presents the structure of the proposed RDCS-HE-DPMM for SG system, which consists of a 24-slot stator and a 22 pole-pair PM rotor. Both AC and DC coils are arranged in the stator slots. The DC field coils are uniformly wound on stator teeth in alternate directions, to form a uniform DC excitation field, which is then modulated by the rotor saliency effect to produce reluctance torque. Besides, the tangentially magnetized PMs are introduced into stator slots to relieve extra DC saturation effect caused by the constant DC flux component in stator core excited by DC field excitation. The rotor uses a consequent-pole structure, in which each PM and its adjacent core constitute a pair of magnetic poles. This PM field is further modulated by stator teeth to provide PM torque component. All rotor PMs are magnetized in the same radial direction. The AC armature winding adopts a single-layer concentrated connection, as shown in Fig. 5.3.

The features of the proposed topology can be listed as

(1) With a single stator and rotor, the machine structure is mechanically robust.

(2) Benefiting from a single-layer concentrated design of both DC field winding and AC armature winding, the winding ends are short, thus copper loss and materials are reduced.

(3) With unique relieving-DC-saturation design, the stator core utilization can be boosted and thus the reluctance torque contribution is enhanced.

(4) The DC field terminal enables a bidirectional field regulation, which provides flexible flux weakening as well as wide-speed generation operation, which is especially important for multi-mode SG operation in HEV.
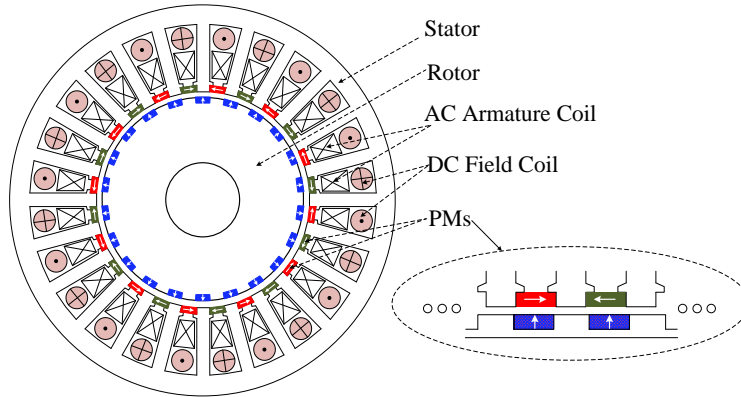
Fig. 5.2 Configuration of the proposed RDCS-HE-DPMM.
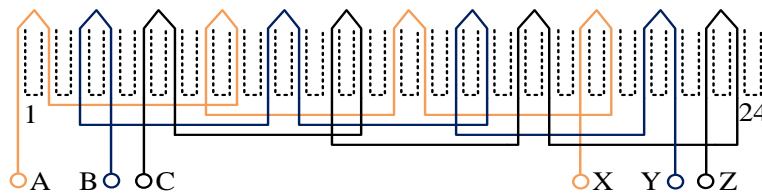
Fig. 5.3 Connection of the armature winding.
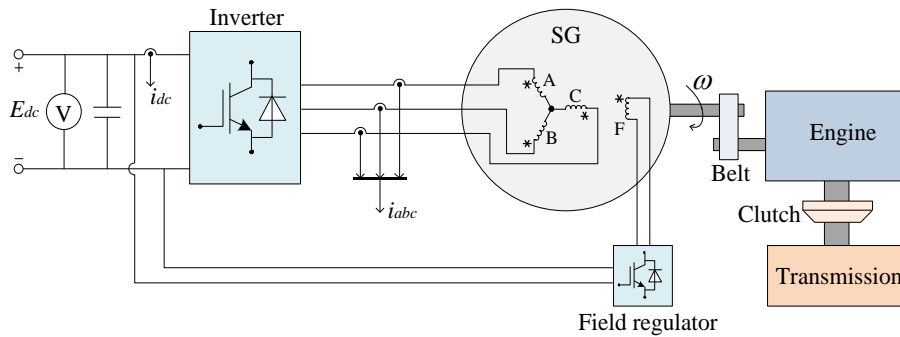
Fig. 5.4 SG system based on the proposed RDCS-HE-DPMM.

5.2.2 Operation Modes as a SG in HEV

Based on the proposed RDCS-HE-DPMM, a SG system is built as presented in Fig. 5.4. As a SG for HEV, the proposed machine mainly has these three working modes, namely engine cranking, battery charging and torque overlapping, respectively.

Mode I, engine cranking. When an HEV stops for a long time and needs to start again, the SG should work as an electromotor to drive the engine to the minimum operating speed.

109

Therefore, the SG should have the ability to provide a continuous starting torque to overcome the drag force of a cold engine.

Mode II, battery charging. When the engine runs to a steady speed and takes charge of the propulsion, the SG should work as a generator and charge the battery until it is full. Meanwhile, if the HEV operates downhill or braked, the SG should perform regenerative braking and charge the battery.

Mode III, torque boosting. When the HEV operates under a low-speed climbing circumstance, the SG is required to perform as an electromotor to provide extra torque, which can assist the torque generated by the engine, and in such a way, the HEV can achieve a better climbing performance.

With extra DC field terminal in the proposed machine, more flexible SG control can be achieved at different HEV working conditions, which can be summarized as

At Mode I, by injecting positive maximum DC field current, boosted cranking torque can be achieved to shorten the start-up process of engine. Further, by coordinating DC field control and vector field control, enhanced flux weakening operation can be achieved, thus leading to extended constant power speed range.

At Mode II, by regulating the DC field excitation, the output voltage can be continuously adjusted to ensure smooth charging characteristic under different engine speed, which accordingly increase the service life of the rectifier and battery. Meanwhile, de-excitation operation can be performed when a power device short-circuit situation occurs, which can avoid the huge current strike and corresponding braking torque.

At Mode III, similar with that at Mode I, with a positive DC field current, enhanced assistant torque can be obtained, which gives the HEV improved climbing-performance.

In general, the existence of DC field terminal in the proposed RDCS-HE-DPMM enables a more flexible torque and speed control at starting mode and wide voltage regulation at generation mode, thus it can be a potential SG candidate for HEVs.

(a)

(b)
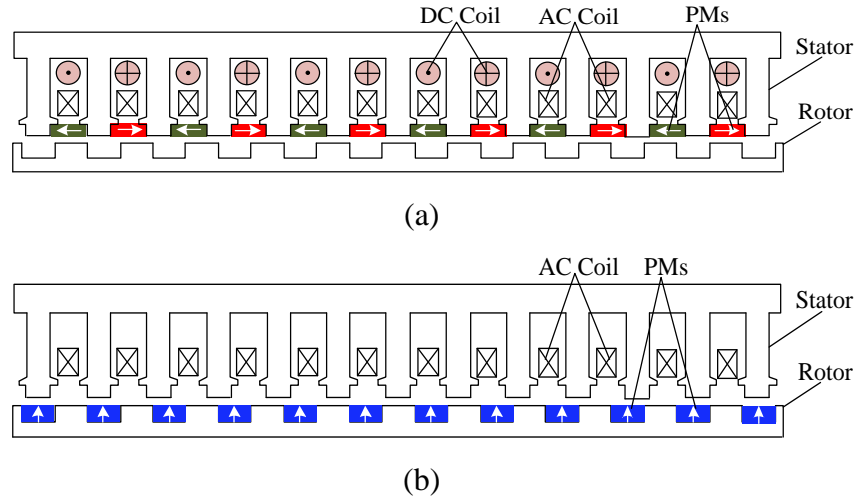
Fig. 5.5 Separation of the proposed RDCS-HE-DPMM. (a) RDCS-RM. (b) CP-VPMM.

5.3 DESIGN MECHANISM

Considering the parallel magnetic circuit excited by DC field coils and rotor PMs, the design principle of this new topology is explained by splitting it into two separate structures, namely relieving-DC-saturation reluctance machine (RDCS-RM) and consequent-pole Vernier PM machine (CP-VPMM), as denoted in Fig. 5.5. In the following, the operation principles of two different structures will be introduced, and their coupling relationship will be revealed to show the design mechanism of the proposed RDCS-HE-DPMM.

5.3.1 Relieving-DC-Saturation Reluctance Machine

Fig. 5.6 presents the flux distribution with rotor position variation in RDCS-RM. As denoted in Fig. 5.6(a), when the rotor salient pole is aligned with wound stator tooth, the loop reluctance for DC field excitation is minimized. Therefore, the coil flux of DC field

source reaches the maximum value. In contrast, as shown in Fig. 5.6(b), when the rotor rotates half of pole pitch, the wound stator tooth is now aligned with the rotor slot, and consequently, the loop reluctance for DC field excitation is maximized and the coil flux now reaches the minimum value. As shown in Fig. 5.7(a), with the rotor rotation, unipolar pulsating coil flux linkage can be established by DC field current, which can be expanded by using Fourier Series as

$$\varphi_{coil} = \varphi_{dc} + \sum \varphi_n \sin(n\omega t + \theta_n), n = 1, 2, 3... \tag{5.1}$$

where φ_{dc} is the DC flux bias, φ_n is the magnitude of the nth flux harmonics, ω is the electrical angle velocity, t is the time, θ_n is the initial phase. Based on a magnetomotive force (MMF) and permeance model, φ_{dc} can be expressed as

$$\varphi_{dc} = N_{dc} i_{dc} \cdot \Lambda_{ave} \cdot \theta_{st} d_{so} l \tag{5.2}$$

where N_{dc} is the turn number of DC field coil, i_{dc} is the magnitude of DC field current, Λ_{ave} is average permeance of DC flux loop, θ_{st} is arc of stator teeth, d_{so} is the outer diameter of the stator, and l is stack length.

Moreover, PMs are introduced into stator slots to relieve the DC saturation effect in stator core due to the biased flux feature. It can be seen in Fig. 5.6, regardless of the rotor position, slot PMs always link the stator core for the minimum reluctance principle, thus a constant PM flux bias is constructed at stator side, which can be utilized to cancel the DC flux bias. As denoted in Fig. 5.7(b), with a certain slot PMs, DC flux bias can be decreased to zero, at which the optimal RDCS operation is achieved. The usage of slot PMs for optimal RDCS operation can be determined by

$$H_c h_{pms} \cdot \Lambda_s \cdot \theta_{st} d_{so} l = \varphi_{dc} \tag{5.3}$$

where H_c is the coercivity of the slot PMs, h_{pms} is height of slot PMs, Λ_s is average permeance of slot PM flux loop. With this RDCS operation, the maximum flux density in stator core can be reduced, which enhances reluctance torque generation.
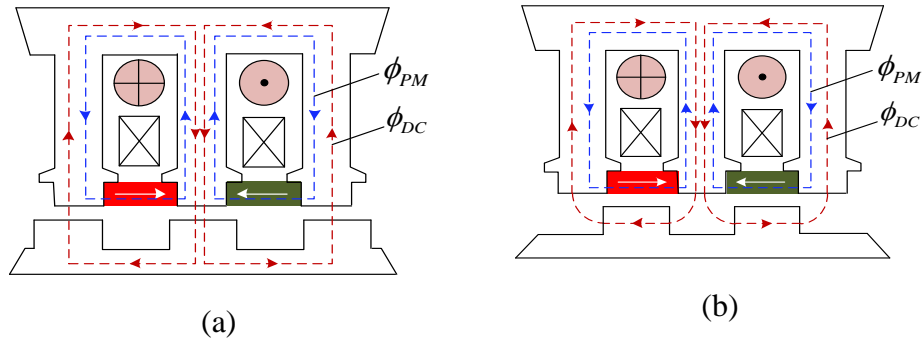
Fig. 5.6 Illustration of coil flux variation in RDCS-RM. (a) Position a, maximum DC flux. (a) Position b, minimum DC flux.
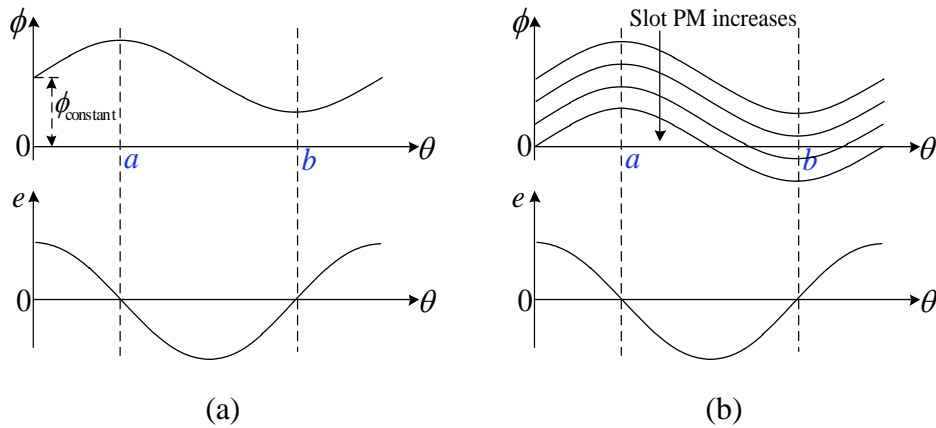
Fig. 5.7 Coil flux and back EMF. (a) Without slot PMs. (b) With slot PMs

5.3.2 Consequent-Pole Vernier PM Machine

For CP-VPMM, all PMs are magnetized in the same radially outward direction. Each PM and its adjacent core form a pair of magnetic poles, and the magnetomotive force (MMF) produced by rotor PMs is illustrated in Fig. 5.8, which can be expressed as

113

$$F_{PM}(\theta,t) = \sum_{n=1,3,5...}^{\infty} \frac{4F_{PM}}{n\pi} \sin(np_{PM}\frac{\theta_r}{2})\cos\left[np_{PM}(\theta-\theta_0-\omega_r t)\right] \qquad (5.4)$$

where F_{PM} is the amplitude of PM MMF, p_{PM} is the pole pair number of rotor PMs. θ_r is the arc of rotor pole. θ is the rotor mechanical angle and θ_0 is its initial value. ω_r is the angular velocity of rotor. t is the running time.
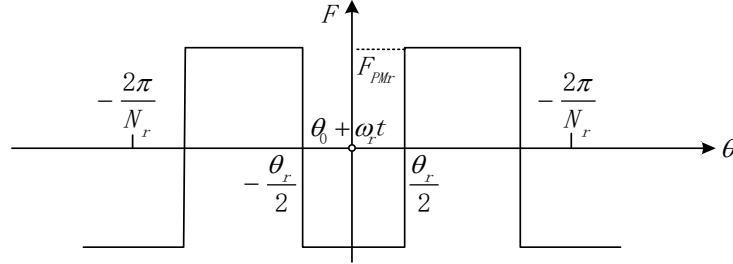
Fig. 5.8 MMF generated by rotor PMs.
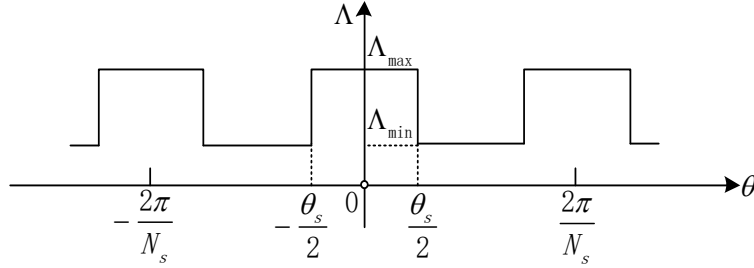
Fig. 5.9 Permeance distribution at the stator side

Due to the open-slot design at stator side, stator permeance is not uniform as shown in Fig. 5.9, which can be expanded as

$$\Lambda_s(\theta) = \Lambda_{s0} + \sum_{k=1}^{\infty} \frac{\Lambda_{s1}}{k\pi}\sin(kN_s\frac{\theta_s}{2})\cos(kN_s\theta) \qquad (5.5)$$

where Λ_{s0} and Λ_{s1} are the average value and peak to peak value of the stator permeance, respectively. N_s is the number of stator teeth. θ_s is the arc of stator teeth. Then, the air-gap field excited by rotor PMs can be derived by multiplying (5.4) and (5.5)

114

$$
\begin{cases}
B_{PM}(\theta,t) = F_{PM}(\theta,t)\Lambda_s(\theta) = \dfrac{4F_{PM}\Lambda_{s0}}{\pi} \sum_{n=1,3,5}^{\infty} C_n \sin\left[np_{PM}(\theta - \theta_0 - \omega_r t)\right] \\[2mm]
+ \dfrac{2F_{PM}\Lambda_{s1}}{\pi^2} \sum_{n=1,3,5}^{\infty} \sum_{k=1}^{\infty} C_n C_k \left[\cos(\varepsilon_1) + \cos(\varepsilon_2)\right] \\[2mm]
C_n = \dfrac{1}{n}\sin(np_{PMr}\dfrac{\theta_r}{2}), C_k = \dfrac{1}{k}\sin(kN_s\dfrac{\theta_s}{2}) \\[2mm]
\varepsilon_1 = \left(np_{PM} - kN_s\right)\left[\theta + \dfrac{np_{PM}}{np_{PM} - kN_s}(\theta_0 + \omega_r t)\right] \\[2mm]
\varepsilon_2 = \left(np_{PM} + kN_s\right)\left[\theta - \dfrac{np_{PM}}{np_{PM} + kN_s}(\theta_0 + \omega_r t)\right]
\end{cases}
\tag{5.6}
$$

TABLE 5.1 Harmonics Components Excited by Rotor PMs

Group	Spatial order	Amplitude	Rotation velocity
I	np_{PM}	$\dfrac{4F_{PM}\Lambda_{s0}}{\pi}C_n$	$n\omega_r$
II	$\|np_{PM} - kN_s\|$	$\dfrac{2F_{PM}\Lambda_{s1}}{\pi^2}C_n C_k$	$\dfrac{-np_{PM}}{\|np_{PM} - kN_s\|}\omega_r$
III	$np_{PM} + kN_s$	$\dfrac{2F_{PM}\Lambda_{s1}}{\pi^2}C_n C_k$	$\dfrac{np_{PM}}{np_{PM}+kN_s}\omega_r$

Based on Eq. (5.6), the excited harmonics by rotor PMs are summarized in Table 5.1. The harmonics in Group I are generated by PM field without modulation effect, similar with that in PM synchronous machine. The harmonics in Group II and Group III are produced by stator teeth modulation. Those harmonics with the same pole pair number and the same rotation speed as that in the armature field, will interact effectively and make PM torque generation. Based on the flux modulation theory, the pole pair number of armature winding p_a, and the rotation velocity of armature field ω_a, can be expressed as

$$
p_a = \left| p_{PM} - N_s \right|, \quad \omega_a = G_r \omega_r
\tag{5.7}
$$

where G_r is the magnetic gearing ratio and equals to $\dfrac{P_{PM}}{Pa}$.

(a)

(b)
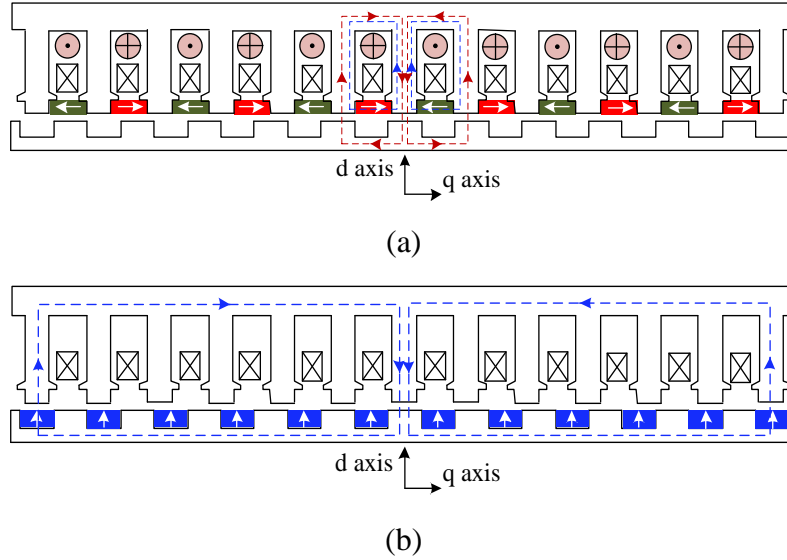
Fig. 5.10 D-axis flux for two structures. (a) RDCS-RM. (b) CP-VPMM.

5.3.3 Magnetic Coupling between Two Structures

As analyzed above, RDCS-RM and CP-VPMM both exist in the proposed topology. To effectively integrate two structures, two necessary conditions should be satisfied as.

(1) The armature winding must use a single-layer concentrated design. This is because, compared to double-layer concentrated design or distributed design, armature field excited by a single-layer concentrated design has more air gap harmonics, and thus it can synchronously interact with DC field excitation and rotor PM excitation.

(2) The main magnetic circuit for each structure should not be designed at saturation condition. This is because two structures share the common magnetic circuit in both stator core and rotor core. Once a structure is designed in close to the saturation point, the effectiveness of the other machine will not be distinct.

The maximum flux distribution for two structures are shown in Fig. 5.10. It reveals that two structures can obtain the maximum flux at the same d-axis position, which means, flux components in two structures are entirely in phase and can couple effectively.

116

5.4 SLOT POLE COMBINATION

The feasible slot/pole combinations in the proposed machine can be expressed as

$$\begin{cases} N_s = 2mj, \ j = 1, 2, 3 \ldots \\ N_r = N_s \pm 2k, \ k = 1, 2, 3 \ldots \end{cases} \tag{5.8}$$

where m is the phase number. The configurations with odd pole pairs are not employed considering the influence of unbalanced magnetic pull. Meanwhile, based on the flux modulation effect, N_r should be designed in close to N_s to achieve a relatively high pole ratio and torque density. Hence, using a 24-slot stator, four potential slot/pole combinations, 24/20, 24/22, 24/26 and 24/28 are studied in this paper. The slot angle can be expressed as

$$\gamma = \frac{360° N_r}{N_s} \tag{5.9}$$

With a single-layer concentrated winding design, the electrical angle difference $\Delta\theta_e$ between two adjacent AC armature coils in one phase can be calculated as

$$\Delta\theta_e = (2m\gamma) \bmod (360°) \tag{5.10}$$

The coil flux phasor diagrams are given in Fig. 5.11. Considering that phase A consists of coil A1, A2, A3 and A4, the coil flux for A1 can be expanded by Fourier analysis as

$$\varphi_{A1} = \varphi_{dc} + \sum \varphi_n \sin(n\omega t + \theta_n), n = 1, 2, 3 \ldots \tag{5.11}$$

where φ_{dc} is the DC flux component, φ_n is the amplitude of the nth harmonics, ω is electrical angular velocity, θ_n is the initial phase angle of the nth harmonics. For 24/20 and 24/28 designs, A1, A2, A3 and A4 have the same flux linkage. Accordingly, phase flux for 24/20 and 24/28 designs can be expressed as

$$\varphi_A = 4\varphi_{A1} = 4\varphi_{dc} + 4\sum \varphi_n \sin(n\omega t + \theta_n), n = 1, 2, 3 \ldots \tag{5.12}$$

However, in 24/22 and 24/26 cases, coil flux of A2 and A4, is delayed by 180° than A1 and A3, and thus can be written as

$$\varphi_{A2} = \varphi_{dc} + \sum \varphi_n \sin(n\omega t + n\pi + \theta_n), n = 1, 2, 3... \tag{5.13}$$

The phase flux for 24/22 and 24/26 cases can be expressed as

$$\varphi_A = 2(\varphi_{A1} - \varphi_{A2}) = 4\sum \varphi_n \sin(n\omega t + \theta_n), n = 1, 3, 5... \tag{5.14}$$

As shown in Equ. (5.14), in 24/22 and 24/26 cases, DC bias and all even-order harmonics can be cancelled in the final phase flux, while they are inherited in 24/20 and 24/28 designs. These harmonics cannot make torque generation but increase core loss and PM loss.
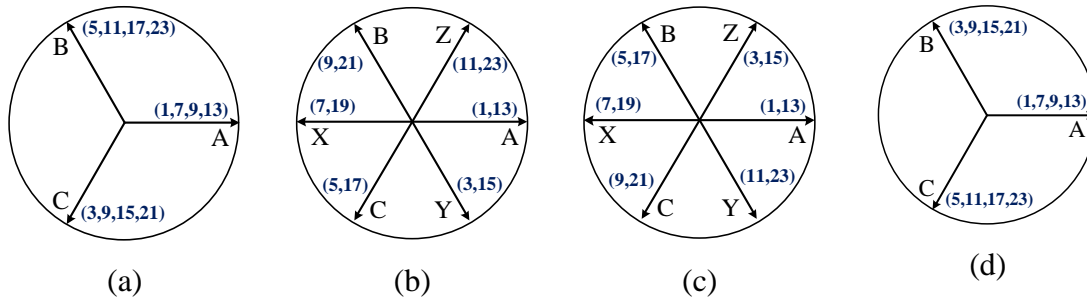
Fig. 5.11 Coil flux phasor diagrams. (a) 24/20. (b) 24/22. (c) 24/26. (d) 24/28.

Using finite element method with software Maxwell, the flux characteristic with different slot/pole combinations are assessed. The general dimension parameters are denoted in Fig. 5.12, with initial design values listed in Table 5.2. Fig. 5.13 and Fig. 5.14 shows the calculated no-load flux linkage of two structures, along with harmonic spectrums obtained by Fast Fourier Analysis. It can be found, for both RDCS-RM and CP-VPMM, 24/22 and 24/26 designs achieve more symmetrical flux linkage with larger fundamental components and reduced even-order components compared with that of 24/20 and 24/28 cases, which agrees with the theoretical analysis. The torque performance with different

slot/pole combinations is evaluated with four variable parameters optimized. It can be seen from Table 5.3, the 24/22 design obtains the largest rated torque, minimized cogging torque and torque ripple, thus it is recommended for further investigation.
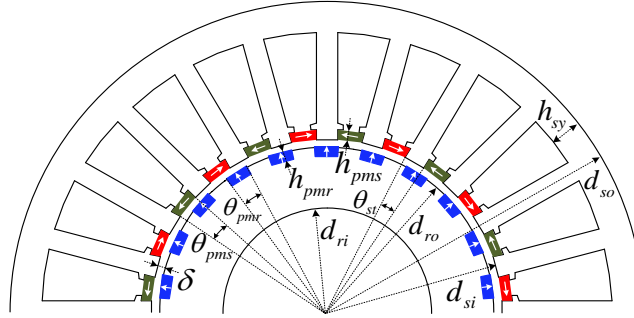
Fig. 5.12 General dimension parameters.

TABLE 5.2 Initial Design Parameters of the Proposed 24/22 RDCS-HE-DPMM

Symbol	Parameter	Unit	Value
d_{so}	Outer diameter of the stator	mm	120
d_{si}	Inner diameter of the stator	mm	69
d_{ro}	Outer diameter of the rotor	mm	68
d_{ri}	Inner diameter of the rotor	mm	40
δ	Air gap length	mm	0.5
l	Stack length	mm	50
h_{sy}	Height of stator yoke	mm	5
θ_{st}	Arc of stator teeth	°	7
h_{pms}	Height of slot PMs	mm	2
h_{pmr}	Height of rotor PMs	mm	2
θ_{pmr}	Arc of rotor PMs	°	7
	Slot factor	-	0.7
	Wire size (AWG)	-	20
	AC coil number of Turns	-	20
	DC coil number of Turns	-	20

(a)   (b)
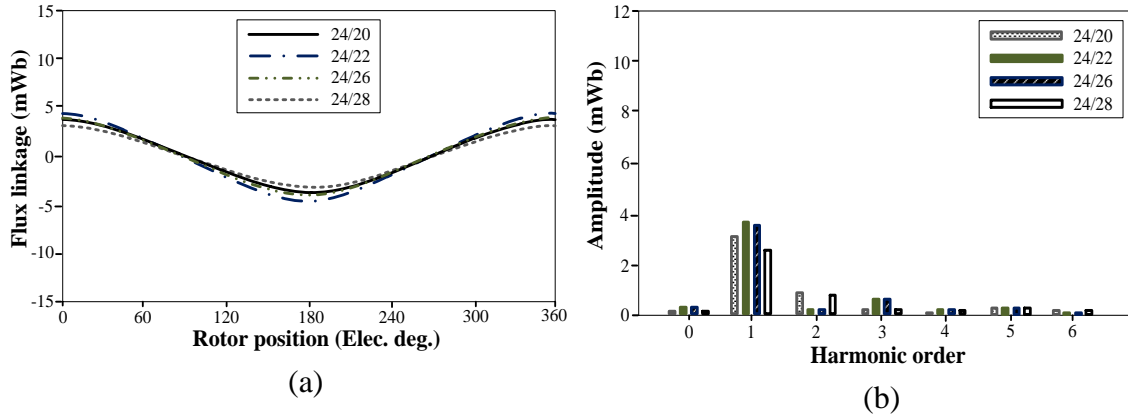
Fig. 5.13 RDCS-RM. (a) No-load phase flux. (b) Harmonics distribution.

(a)   (b)
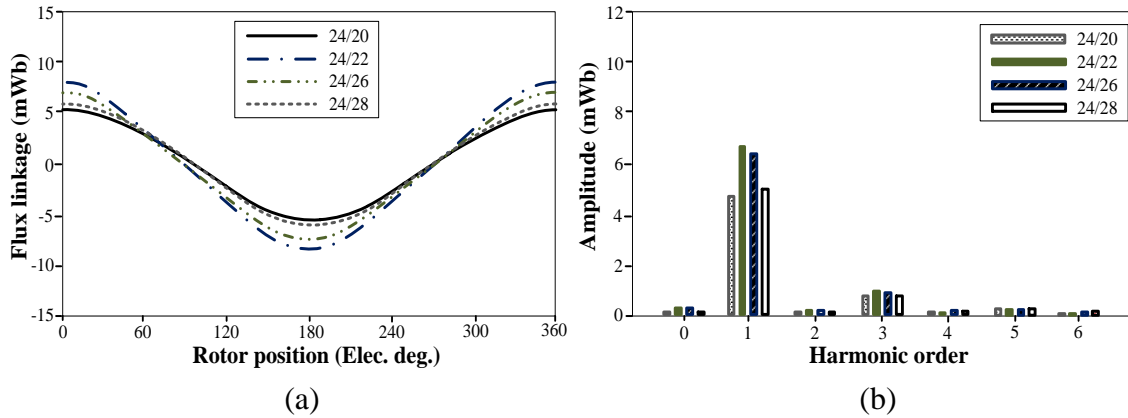
Fig. 5.14 CP-VPMM. (a) No-load phase flux. (b) Harmonics distribution.

TABLE 5.3 Torque Performance with Different Slot Pole Combinations

N_s	24	24	24	24
N_r	20	22	26	28
θ_{st} (°)	7.2	6.8	6.9	7.1
h_{pms} (mm)	1.7	1.8	2.0	2.1
h_{pmr} (mm)	2.5	2.2	2.5	2.2
θ_{pmr} (°)	8.8	7.8	6.6	6.4
Cogging torque (Nm)	1.42	0.30	0.42	1.63
Torque ripple (Nm)	1.59	0.59	0.76	1.68
Rated torque (Nm)	5.81	7.05	6.64	6.13

5.5 FINITE ELEMENT ANALYSIS

Fig. 5.15 gives the no-load flux distribution at different excitation status. As shown in Fig. 5.15(a), the flux linkage generated by DC current starts from the wound tooth, enters the rotor salient poles and finally comes back from adjacent stator teeth. This flux linkage contributes to reluctance torque generation. However, it intensifies the level of saturation in stator core. To solve this problem, PMs are introduced into stator slots to produce a constant flux component in stator core, which can be negatively combined with the DC flux bias. As presented in Fig. 5.15(b), with the assistance of slot PMs, the flux density in stator core can be greatly reduced, while that in rotor core keeps unchanged almost. In this way, the extra DC saturation effect is relieved, and thus the influence of DC field excitation on rotor PM torque generation is minimized. As presented in Fig. 5.15(c), when DC field current and dual PMs are both active, the flux distribution in stator core mainly arises from rotor PM field, while that in rotor core is a combination of DC field and PM field. This proves the no-load flux in two structures can effectively couple without DC saturation.

| (a) | (b) | (c) |
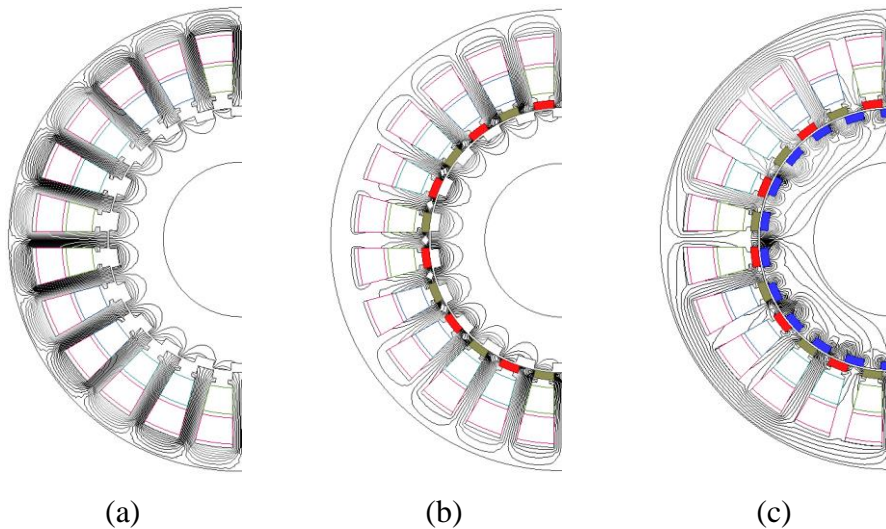
Fig. 5.15 No-load flux distribution. (a) Only 20A DC current. (b) 20A DC current and slot PMs. (c) 20A DC current and dual PMs.
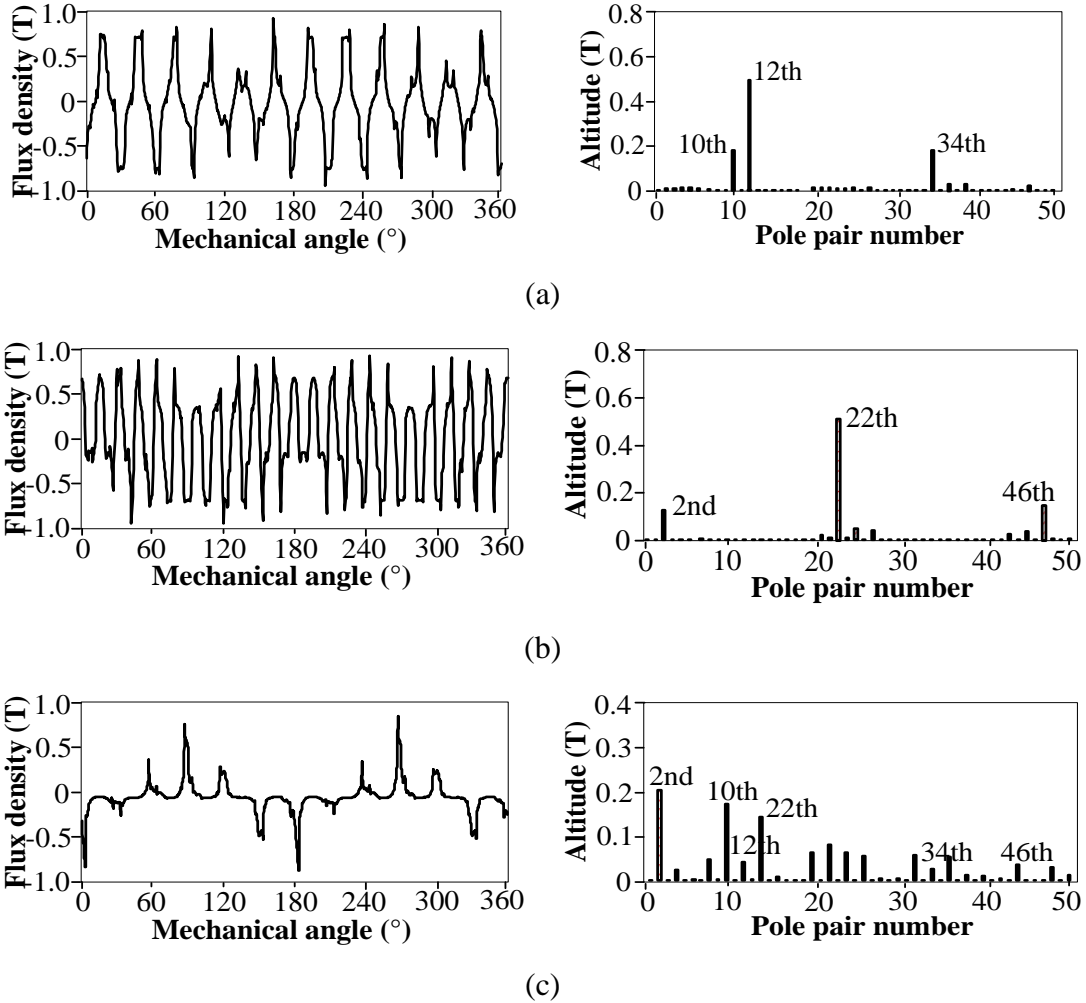
Fig. 5.16 Flux density in air gap and its harmonics distribution. (a) Only 20A DC field current. (b) Only rotor PMs. (c) Only 20A AC armature current.

Fig. 5.16 gives the calculated air gap flux density and harmonic distribution excited by different sources. As shown in Fig. 5.16(a) and Fig. 5.16(b), those harmonics excited by DC field current and rotor PMs have entirely different pole pair numbers. Therefore, to simultaneously interact with two excitation sources, armature field must be designed with multi working harmonics. Fig. 5.16(c) presents the air gap field excited by a single-layer concentrated armature winding. It is shown plentiful harmonics are produced by the armature field, and the dominant harmonic components are synchronous with those of two excitation sources. Therefore, it is proved that, in the proposed machine, the single-layer

concentrated armature winding can synchronously interact with two hybrid excitation sources benefiting from its harmonic diversity.

Fig. 5.17 presents the no-load flux linkage. It can be seen, with RDCS-RM and CP-VPMM both active, two flux components can overlap together. Fig. 5.18 shows the torque angle curve with 20A armature current applied. It is shown that reluctance torque in RDCS-RM and PM torque in CP-VPMM can be superposed effectively. Hence, the proposed machine can provide enhanced torque density for HEVs in starting period.
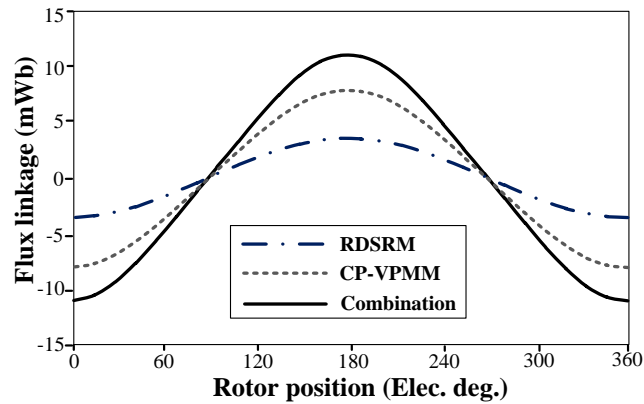
Fig. 5.17 No-load phase flux linkage.
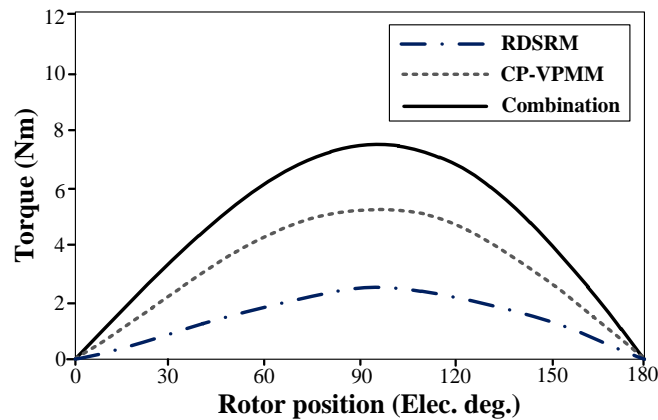
Fig. 5.18 Torque angle curve with 20A AC armature current.
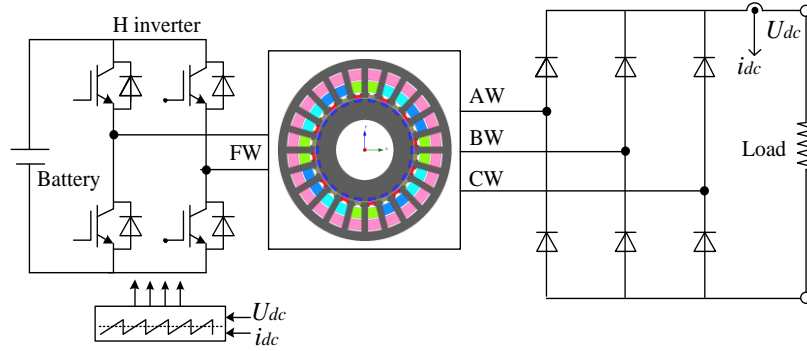
Fig. 5.19 Field-circuit coupling model for generating operation.
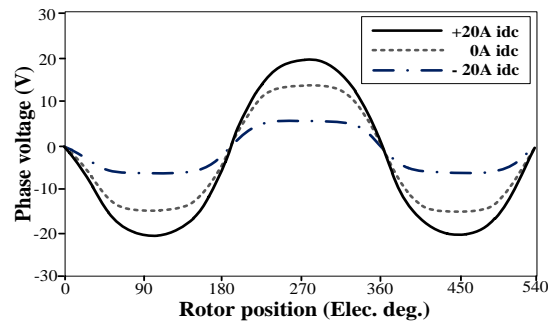
Fig. 5.20 No-load phase voltage at speed 1000 rpm.
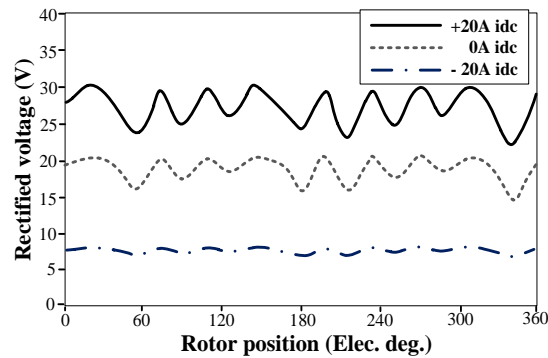
Fig. 5.21 No-load rectified DC voltage at speed 1000 rpm.

A field-circuit model is established for the proposed machine as shown in Fig. 5.19. The three phase windings are connected into a passive diode rectifier. The DC field current is regulated according to the feedback of output voltage and current. By changing input speed and load resistance, different generation conditions are evaluated.

124
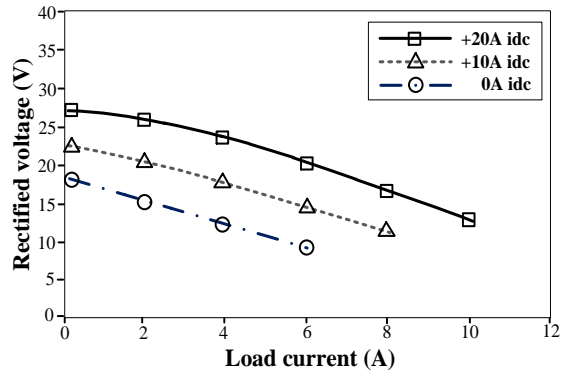
Fig. 5.22 Rectified voltage against load current at speed 1000 rpm.
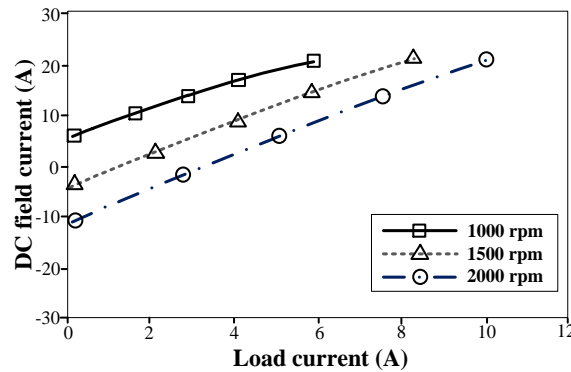
Fig. 5.23 DC field current regulation for constant voltage operation.

Fig. 5.20 presents the no-load phase voltage with bidirectional DC field current. It is shown the phase voltage can be weakened or boosted flexibly. Accordingly, controllable rectified voltage can be obtained at the output terminal as shown in Fig. 5.21. It is shown, the voltage drop range is larger than voltage boost range, which is caused by inner DC saturation effect. With load current changing, the output voltage characteristic is plotted in Fig. 5.22. It is revealed DC field current has little influence on the voltage regulation factor. The constant-voltage generation with variable speed is evaluated in Fig. 5.23. The constant voltage is set at 20V. By regulating DC field current according to load variation, the output voltage can be maintained constant in a wide speed range. Therefore, the proposed machine is very suitable for the wide-speed on-board generation in HEV.

5.6 PARAMETERS ANALYSIS AND DESIGN OPTIMIZATION

5.6.1 Dimension Parameters

The influence of important dimension parameters on torque generation in RDCS-HE-DPMM is investigated, including the stator yoke height, stator teeth arc, rotor PM height and rotor PM arc. The DC current and AC current are both fixed at 20A.

Fig. 5.24(a) presents the influence of stator yoke height. It can be noticed, with the increasing of stator yoke height, torque in RDCS-RM and CP-VPMM are almost constant, which means the stator yoke is far from saturated. This is benefiting from the relieving-DC-saturation effect produced by slot PMs.

Fig. 5.24(b) shows the influence of stator teeth arc. It is found, with the increasing of stator teeth arc, the torque components of RDCS-RM and CP-VPMM are almost unchanged. This means stator teeth arc shows little influence on combined torque.

Fig. 5.24(c) shows the influence of rotor PM height. With rotor slot height increasing from 1mm to 5mm, the reluctance torque of RDCS-RM shows a distinct increase. This is because RDCS-RM works on the rotor reluctance variation, and the larger rotor PM height is, larger reluctance variation exists. Besides, torque of CP-VPMM keeps increasing until PM height reaches 2mm, and after which it decreases due to the PM saturation effect. The synthetic torque arrives the saturation point with rotor PM height about 2 mm.

Fig. 5.24(d) shows the influence of rotor PM arc. The rotor PM height is fixed at 2 mm. With the increasing of rotor PM arc, the reluctance torque of RDCS-RM slightly increases due to the reduced DC leakage flux. The PM torque of CP-VPMM presents a faster growth along with the PM volume increasing. Therefore, to achieve higher combination torque, the rotor PM arc is recommended to be designed relatively larger.
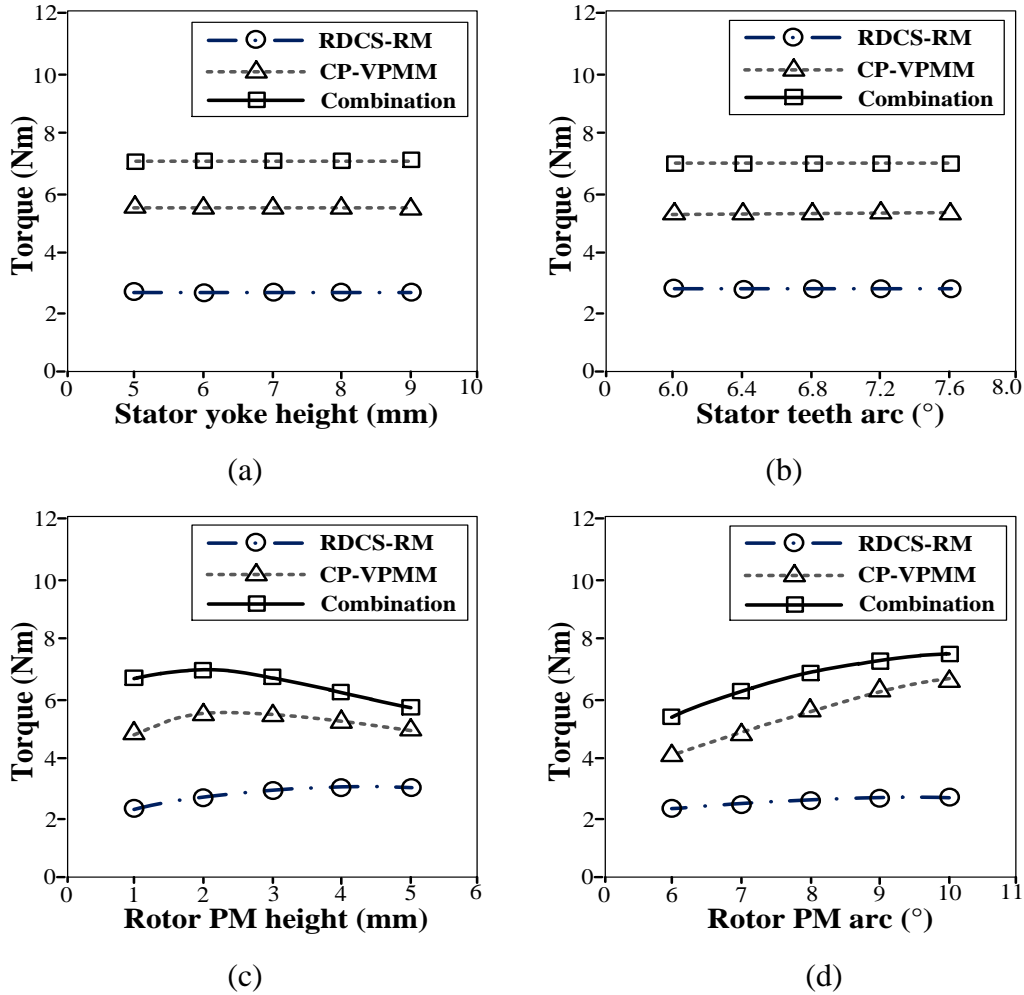
Fig. 5.24 Influence of dimension parameters on torque performance.

Based on above discussion, it is interesting to find, the torque performance of the proposed RDCS-HE-DPMM is more sensitive to rotor dimension parameters than stator dimension parameters, which can be considered during its design optimization.

5.6.2 AC to DC Split Ratio

In the proposed RDCS-HE-DPMM, AC coils and DC coils occupy the same stator slots. It is necessary to investigate the influence of slot split ratio between the AC coils and DC coils on machine performance. As shown in Fig. 5.25, the reluctance torque achieves the maximum value with split ratio of 1: 1, and the combination torque at this point is almost

the same as that with the whole AC design. This is because, when split ratio is larger than 1:1, the torque component of CP-VPMM trends to be saturated, while the reluctance torque of RDCS-RM can still make contribution.

Moreover, the voltage regulation ratio is defined as

$$V_r = \frac{e_{idc\_p} - e_{idc\_n}}{e_{idc\_0}}$$
(5.15)

where e_{idc_p}, e_{idc_n}, e_{idc_0} are the no-load back EMF values with the positive and negative maximum DC current, and zero DC current, respectively. This index represents the control ability of DC field terminal on flux weakening acceleration and constant-voltage generation. It is shown in Fig. 5.25, with the split ratio increasing, the voltage regulation ratio decreases linearly. With the split ratio of 1:1, the voltage regulation ratio is 84%.

Fig. 5.26 shows the calculated loss and efficiency performance with different split ratios. It is interesting to found when the split ratio increases, the core loss and PM eddy current loss increases distinctly. This is because the magnetic circuit of CP-PVMM is relatively easier to be saturated than that in RDCS-RM, due to flux modulation effect. Consequently, introducing DC field excitation equipped with RDCS effect can relieve the global saturation effect, and further the core loss and PM eddy current loss can be also mitigated. In Fig. 5.26, it can be seen the calculated efficiency with split ratio of 1:1, is higher than that with the whole AC design, which is an inspiring result.

Based on the above analysis, in the proposed RDCS-HE-DPMM, the AC to DC slot split ratio is recommended to be 1:1, thus to achieve the coordinated torque performance, optimal voltage regulation, mitigated loss distribution as well as boosted efficiency.
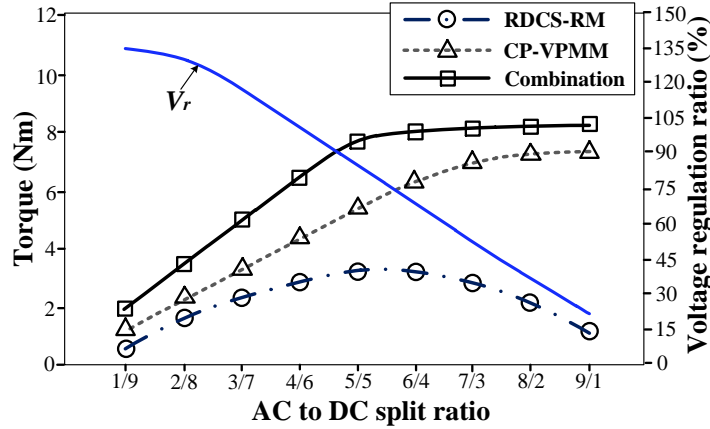
Fig. 5.25 Influence of AC to DC split ratio on torque and voltage regulation.
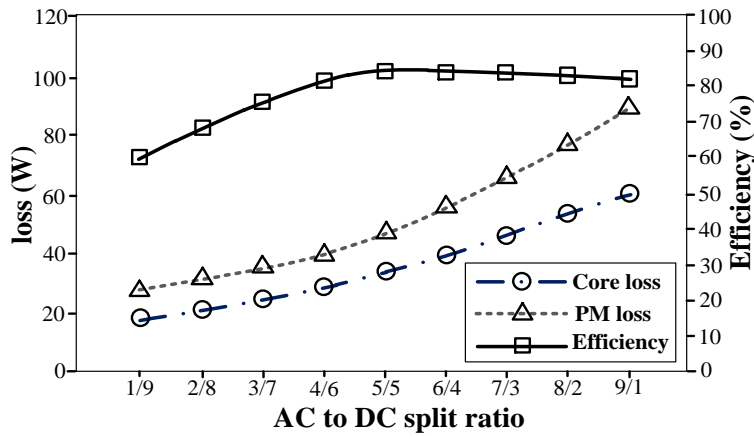
Fig. 5.26 Influence of AC to DC split ratio on loss and efficiency.

5.6.3 Design Optimization

Genetic algorithm (GA), which can search the optimal design by imitating nature selection effect, is employed for design optimization of the proposed design. Meanwhile, to reduce time consumption, a two-stage optimization procedure is performed. Specifically, considering the sensitivity of different dimensions parameters, in the first stage all the sensitive design parameters are synchronously optimized by GA with multi objectives, then in the second stage, the best candidate is optimized by involving insensitive parameters individually. The GA optimization flow is shown in Fig. 5.27. The maximum torque and

efficiency are considered as two optimization objectives. Besides, the optimal cases are evaluated by demagnetization analysis at both 200% overload condition and deep flux weakening status. Some final design parameters after optimization and corresponding torque and efficiency performance are presented in Table 5.4.
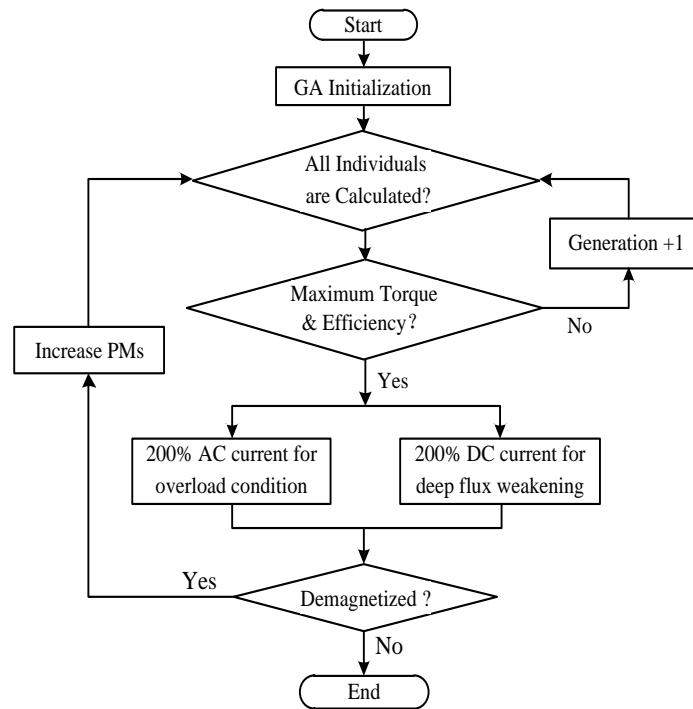
Fig. 5.27 Optimization flow chart for the proposed machine.

TABLE 5.4 Some Optimized Parameters and Electromagnetic Performance

Symbol	Parameter	Unit	Initial	Optimized
h_{sy}	Height of stator yoke	mm	5	5.5
θ_{st}	Arc of stator teeth	°	7	6.8
h_{pms}	Height of slot PMs	mm	2	1.7
h_{pmr}	Height of rotor PMs	mm	2	2.5
θ_{pmr}	Arc of rotor PMs	mm	7	7.9
	Efficiency	%	85	89
	Rated torque	Nm	7.73	8.35

(b)   (c)   (d)
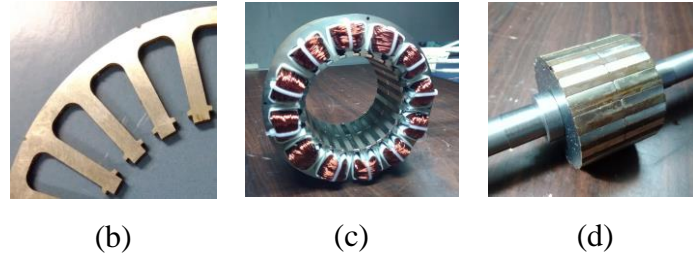
Fig. 5.28 Protype details. (a) Stator lamination. (b) Stator assembly. (c) Rotor assembly.
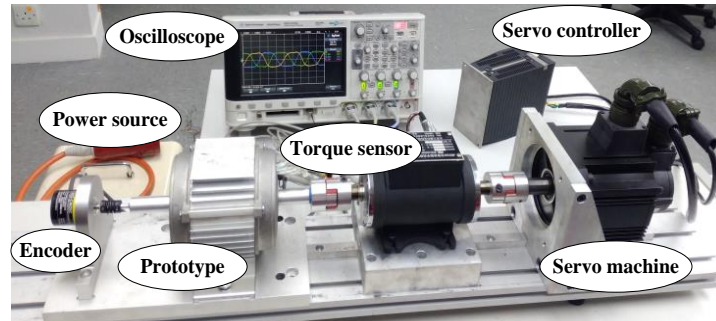
Fig. 5.29 Experimental platform based on the assembled prototype.

TABLE 5.5 Specifications and Materials of the Prototype

Specifications		Materials		
Rated speed	1000 rpm	PMs	Type	NdFeB35
Rated voltage	20 V		Remanence	1.2 T
Rated power	835 W		Coercive force	915 kA/m
Peak Power	1500 W	Steel	Type	MG19_24
Phase inductance	0.8 mH		Saturated point	1.8 T
Phase resistance	0.04 Ω		Mass density	7650 kg/m^3

5.7 EXPERIMENTAL VERIFICATION

To verify the feasibility of the proposed machine, a prototype is manufactured for experimental tests, based on the dimensions listed in Table 5.2 and Table 5.4. The major specifications and materials are listed in Table 5.5. Fig. 5.28 shows the details of prototype. To house PMs in slot openings, extra stator pole shoes are designed with stator teeth as

131

shown in Fig. 5.28(a). The stator assembly is presented in Fig. 5.28(b). Benefiting from a concentrated design, its wiring process is simple and slot factor is boosted. Fig. 5.28(c) shows the rotor assembly. Each PM is joint by two segments to reduce eddy current loss. The test platform is shown in Fig. 5.29, which consists of the prototype, torque sensor, servo machine and drive, DC power source and oscilloscope.

(a)   (b)
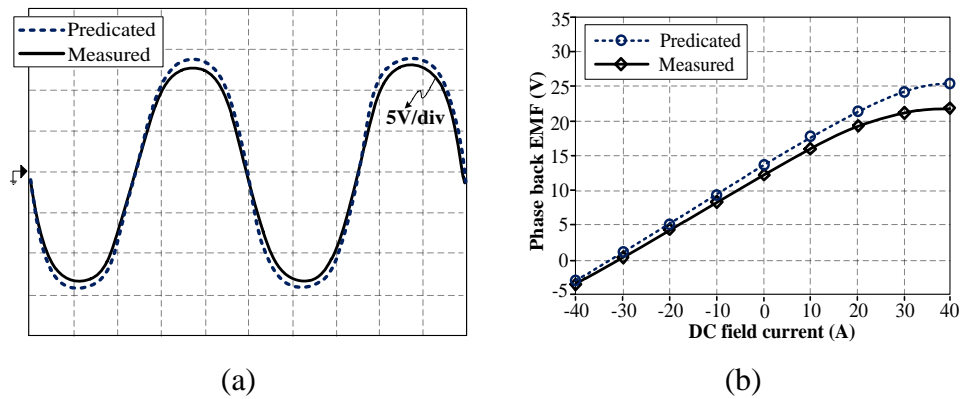
Fig. 5.30 (a) Phase back EMF at 1000 rpm without DC field current. (b) Phase back EMF with different DC field current.
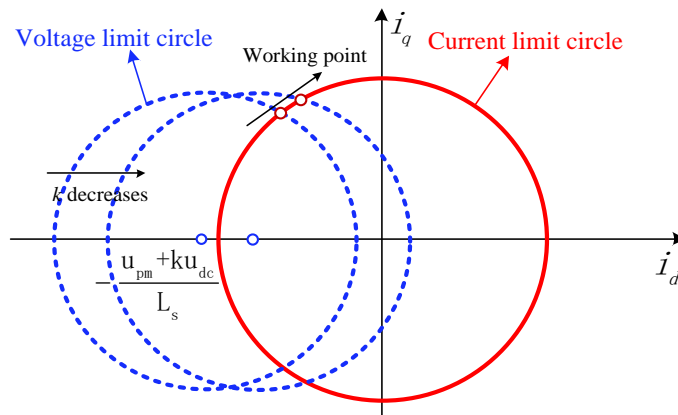
Fig. 5.31 Variation of current/voltage limits at fixed speed with extra DC control.

Fig. 5.30 presents the tested phase back EMF at 1000 rpm and its regulation ability with DC current control. It is shown in Fig. 5.30(a), the tested back EMF basically agrees with that of the finite element analysis, although its amplitude is a little smaller, which is due to

the manufacturing tolerance such as the nonuniform PM magnetization level. Fig. 5.30(b) indicates that the phase back EMF can be bidirectionally regulated by DC field current, which contributes bidirectional flux regulation ability.

The flux weakening performance is further evaluated for the proposed topology. In the flux weakening operation, the voltage and current limits should be considered as

$$\begin{cases} \left(u_d + u_0 \right)^2 + u_q^2 \leq u_{dc}^2 \\ i_d^2 + i_q^2 \leq i_{s\max}^2 \end{cases} \tag{5.16}$$

where u_0 is the no-load back EMF. u_{dc} is the DC bus voltage. $i_{s\max}$ is the inverter current scale. In the proposed RDCS-HE-DPMM, u_0 can be controlled by DC field current, leading to the change of working point during flux weakening as illustrated in Fig. 5.31. With the extra DC flux weakening effect, reduced i_d current is needed to satisfy the voltage limit, which means under a fixed inverter current scale, larger i_q current can be allowed for torque generation. Therefore, the experiment result in Fig. 5.32 indicates that larger torque can be produced with extra DC control during flux weakening operation. Consequently, a smaller starting time is consumed with extra DC control as shown in Fig. 5.33.
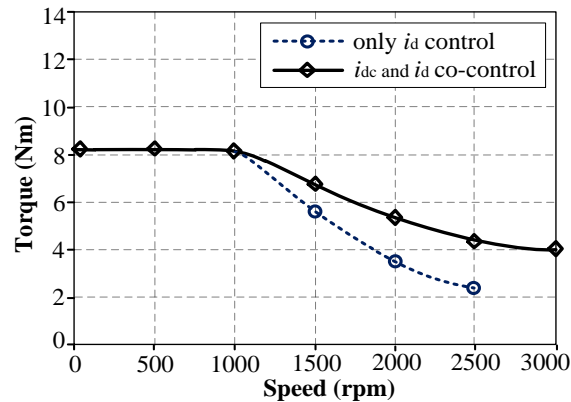
Fig. 5.32 Torque speed curves with different flux weakening controls.
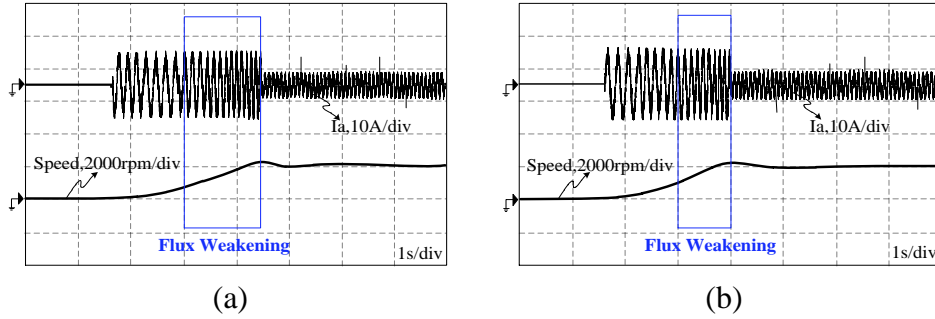
Fig. 5.33 Starting performance with load 2Nm. (a) With only id flux weakening. (b) With id and 20A idc combined flux weakening.
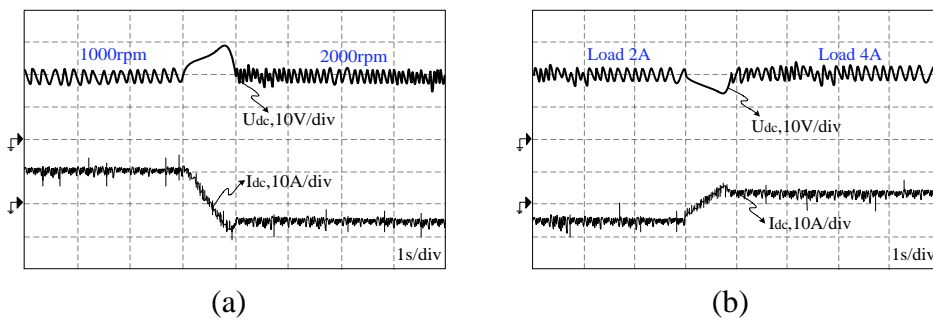
Fig. 5.34 Generation performance. (a) Constant load current of 2A, variable speed from 1000 rpm to 2000 rpm. (b) Constant speed of 1500 rpm, variable load from 2A to 4A.
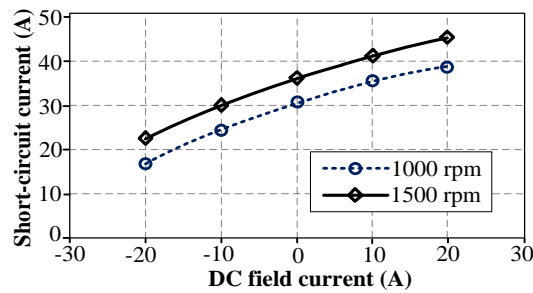
Fig. 5.35 Short-circuit current with different DC field current.

Fig. 5.34 shows the measured generating dynamic performance with speed and load changing. It is shown the output voltage can be maintained unchanged by regulating DC field current at different speed and load conditions. The short-circuit current is measured in Fig. 5.35. It is revealed that injecting negative DC field current can reduce short-circuit current, which is important for safety-critical on-board generation in HEV.

5.8 COMPARATIVE DISCUSSION

To assess the practicality of this new topology, a feature comparison is performed between the traditional CP-VPMM with whole AC coils and the proposed hybrid design, with consideration of the whole speed region in a multi-mode SG system for HEV.

(1) Low-speed constant-torque region. Adopting AC and DC hybrid coils with split ratio 1:1 can achieve comparable torque density to that with the whole AC design, as shown in Fig. 5.25. There are two reasons for this phenomenon. On one hand, with relieving-DC-saturation design, reluctance torque produced by DC excitation is boosted. On the other hand, PM torque excited by AC excitation is easier to be saturated.

(2) Medium-speed flux weakening region. Introducing extra DC coils in the proposed machine provides an additional flux weakening variable of DC current. Specifically, using AC and DC hybrid coils with split ratio 1:1 achieves about 84% voltage regulation ratio. This magnetization control can relieve the need of d-axis AC current for flux weakening, thus allow larger q-axis AC current for torque generation under a fixed inverter scale.

(3) High-speed power generation region. With DC field coils in the proposed machine, output voltage can be simply adjusted by DC terminal and a passive rectifier can be adopted for power conversion. This generation system is simpler and more reliable than that for the traditional machine with the whole AC design. Moreover, with extra DC field coils, short-circuit fault becomes bearable in the proposed RDCS-HE-DPMM.

Based on the above analysis, it can be concluded, compared to the traditional CP-VPMM with whole AC coils, the proposed RDCS-HE-DPMM achieve comparable torque density, boosted flux weakening ability, simpler and more robust power generation, which makes the proposed topology especially suitable for the multi-mode SG operation in HEVs.

5.9 CONCLUSION

This chapter proposes a new relieving-DC-saturation hybrid excitation dual PM machine (RDCS-HE-DPMM) as a novel SG candidate in HEVs. The innovation is to introduce the DC field excitation equipped with relieving-DC-saturation effect into the consequent-pole Vernier PM machine (CP-VPMM). And in this way, the advantages of flexible flux control in RDCS reluctance machine and excellent torque density in CP-VPMM are well combined in the proposed topology, making it very suitable for the multi-mode SG operation in HEVs. Especially, boosted reluctance torque and enhanced flux weakening can be achieved during starting period. Meanwhile, the output voltage can be regulated during generation period and short-circuit current is mitigated. In this chapter, the proposed machine configuration and design mechanism are illustrated in detail. Some slot pole combinations are compared, and 24/22 design is recommended for less flux harmonics and smaller torque ripple ratio. Leading design parameters are determined, especially, the slot split ratio is recommended to be 1:1 to achieve both good torque density and wide flux control. Relevant experiment results verify the feasibility and advantages of the proposed topology. The limitation of this topology is that slot PMs are effective under relatively higher current density by saturation relieving, while it leads low PM utilization factor if designed at low current density. One solution is to use ferrite magnet design as an alternative

CHAPTER 6. SUMMARY AND FUTURE WORK

6.1 SUMMARY

This thesis investigates a new class of electrical machines, namely hybrid excitation flux modulation machine, which incorporates the concepts of hybrid magnetic circuit and flux modulation mechanism to achieve both high torque density and good flux regulation ability in a simple and brushless structure. Four innovative machine concepts are proposed and implemented in this thesis, including hybrid excitation Vernier reluctance machine, zero-sequence-current-based Vernier reluctance machine, hybrid excitation dual PM machine, as well as relieving-DC-saturation hybrid excitation dual PM machine, respectively. The research objectives have been achieved by theoretical analysis, finite element simulation and prototype experiments. The conclusions are presented as follows

The first chapter introduces the research background and provides a literature review of hybrid excitation machines and flux modulation machines, respectively. Different machine topologies, operation principles and potential applications are well compared and discussed. It is revealed the existing hybrid excitation machines still have some common issues such as increased mechanical complexity and torque density sacrifice.

The second chapter proposes a new hybrid excitation Vernier reluctance machine with improved torque density and bidirectional flux regulation ability. The key is to artificially introduce consequent-pole PMs into stator slots to generate flux modulation effect and interact redundant armature harmonics, so that the torque density can be greatly improved compared to its non-PM counterpart. Moreover, the introduced slot PMs share a parallel magnetic circuit with armature excitation, providing bidirectional flux regulation ability and demagnetization withstand ability. Both finite element simulation and protype tests are

conducted, which verifies that by introducing consequent-pole PMs into stator slots, the machine torque density can be doubled compared to its non-PM counterpart.

The third chapter utilizes the zero-sequence current control to eliminate space conflict between AC armature coils and DC field coils in the proposed hybrid excitation Vernier reluctance machine, thus to further increase its torque density and efficiency. The control method of zero-sequence current is introduced, including its specialized space vector pulse width modulation strategy. By using finite element analysis, the optimal injection ratio of zero-sequence current is evaluated, considering the influence of both dimension parameters and electrical parameters. It is revealed, with 10% to 20% injection ratio of zero-sequence current, the proposed machine can achieve about 10% torque density boost and 30% torque ripple reduction. Meanwhile, core loss and PM eddy current loss can be distinctly mitigated with zero-sequence current injection, thus leading to certain efficiency increase.

The fourth chapter proposes a new hybrid excitation dual-PM machine. This machine employs dual consequent-pole PMs arranged in both stator slots and rotor slots, which contributes to high air gap flux density and torque density. Moreover, DC field excitation is introduced to provide an extra flux weakening variable, which can be coordinated with the traditional d-axis vector flux weakening to further extend the torque speed range. The finite element analysis and prototype experiments prove this machine can synchronously offer higher torque density, higher efficiency and better flux weakening ability compared to the existing hybrid excitation dual-PM topology.

The fifth chapter illustrates the phenomenon of extra DC saturation effect in stator core introduced by DC field excitation, and further proposes an innovative topology, namely relieving-DC-saturation hybrid excitation dual-PM machine. The innovation is to introduce

tangentially-magnetized stator slots PMs to generate an opposite flux bias and cancel the DC flux component excited by DC field excitation. In this way, the DC saturation effect in stator core is eliminated, which improves machine torque density and flux regulation ability. This new machine is explored as the starter generator candidate in hybrid electric vehicles. It is revealed that, with relieving-DC-saturation design, 25% torque density boost and 86% flux regulation ability can be both achieved, making this new hybrid excitation topology especially suitable for multi-mode starter generator application.

In conclusion, this thesis proposes and investigates a series of new hybrid excitation flux modulation machines by incorporating hybrid magnetic circuit and flux modulation theory. Some achievements are obtained in terms of improved torque density, eliminated space conflict between DC field coils and AC armature coils, as well as reduced stator DC saturation effect, which can provide some new design perspectives and technologies in the field of hybrid excitation machines. The theoretical modeling, finite element analysis and prototype tests are conducted, which verify the feasibility of the proposed topologies.

A comparative discussion for the proposed four topologies is provided in the following, which could serve a simple guideline for the topology selection in different applications. The hybrid excitation Vernier reluctance machine with separate DC field coils proposed in Chapter 2 is named as Topology I, its DC-coil-free design by zero-sequence current control in Chapter 3 is named as Topology II, the hybrid excitation dual-PM machine with triple flux modulation effect in Chapter 4 is referred as Topology III, and its associated topology with relieving-DC-saturation effect in Chapter 5 is referred as Topology IV, respectively. The performance including torque density, rated efficiency, flux weakening ability, control complexity, system cost, and fault-tolerant ability are compared and listed in Table 6.1

TABLE 6.1 Performance Comparison for Proposed Four Topologies

	Topology I	Topology II	Topology III	Topology IV
Torque density (kNm/m^3)	19.5	21.7	33.8	31.3
Rated efficiency	71%	75%	85%	82%
Flux weakening ability	Good	Good	Medium	Good
Control complexity	Low	High	Low	Low
System Cost	Low	High	Medium	Medium
Fault-tolerant ability	Good	Good	Poor	Poor

6.2 FUTURE WORK

Although this thesis obtains some achievements in hybrid excitation flux modulation machines, some challenges still exist, and future works are recommended as follows

1) Using rare-earth PMs in stator slots increases the machine cost. Future work, for instance, using ferrite magnet design may be an alternative.

2) Injecting zero-sequence current can improve machine performance, while the increased complexity of drive circuit and control strategy are disadvantageous. In future works, developing fault-tolerant capacity under this drive structure, could achieve a balance.

3) The proposed machines use concentrated windings, which is beneficial to flux regulation but leads to low winding factor under flux modulation structures. Future work, employing distributed and concentrated hybrid winding design may be an interesting solution.

4) The proposed machines are all based on flux modulation mechanism, which essentially leads to low power factor compared to traditional PM machines, thus needs improvement.

5) The pole pair number of the designed machine is high and therefore the core loss of the machine and its efficiency could be low. In future works, more slot pole combinations should be comprehensively analyzed for both torque and efficiency improvement

REFERENCES

[1]   D. K. Hong, W. Hwang, J. Y. Lee and B. C. Woo, "Design, analysis, and experimental validation of a permanent magnet synchronous motor for articulated robot applications," *IEEE Trans on Magn.*, vol. 54, no. 3, pp. 1-4, March 2018.

[2]   M. M. Swamy, T. Kume, A. Maemura, and S. Morimoto, "Extented high-speed operation via electronoic winding-change." *IEEE Trans. Ind. Appl.*, vol. 42, no. 3, pp. 742-752. 2006.

[3]   A. M. El-Refaie, T. M. Jahns, P. J. McCleer and J. W. McKeever, "Experimental verification of optimal flux weakening in surface PM Machines using concentrated windings," *IEEE Trans. Ind. Appl.*, vol. 42, no. 2, pp. 443-453, Mar./ Apr. 2006.

[4]   D. Fodorean, A. Djerdir, I. A. Viorel, and A. Miraoui, "A double excited synchronous machine for direct drive application—Design and prototype tests," *IEEE Trans. Energy Convers.*, vol. 22, no. 3, pp. 656–665, Sep. 2007.

[5]   X. Luo, and T. A. Lipo, "A synchronous permanent magnet hybrid AC machine", IEEE Trans. Energy Convers., vol. 15, no. 2, pp. 203-210, Jun. 2000.

[6]   T. Finken and K. Hameyer, "Study and geometry optimization of hybrid excited synchronous alternators for automotive applications," in Proc. IEEE IEMDC'07, Antalya, Turkey, 2007, pp. 124–128.

[7]   J. Nerg, M. Rilla, V. Ruuskanen, J. Pyrhönen, and S. Ruotsalainen, "Direct-driven interior magnet permanent-magnet synchronous motors for a full electric sports car," *IEEE Trans. Ind. Electron.*, vol. 61, no. 8, pp. 4286–4294, Aug. 2014.

[8]   P. B. Reddy, A. M. El-Refaie, K. K. Huh, J. K. Tangudu and T. M. Jahns, "Comparison of interior and surface PM machines equipped with fractional-Slot

concentrated windings for hybrid traction applications," *IEEE Trans. Energy Convers,* vol. 27, no. 3, pp. 593-602, Sept. 2012.

[9]   A. D. Akemakou and S. K. Phounsombat, "Electrical machine with double excitation, especially a motor vehicle alternator," U.S. Patent 6 147 429, Nov. 14, 2000.

[10]   Y. Amara, L. Vido, and M. Gabsi, "Hybrid excitation synchronous machines: energy-efficient solution for vehicles propulsion," IEEE Trans. Veh. Technol., vol. 58, no. 5, pp. 2137-2149, Jun. 2009.

[11]   J. A. Tapia, F. Leonardi, and T. A. Lipo, "Consequent-pole permanent-magnet machine with extended field-weakening capability", *IEEE Trans. Ind. Appl.*, vol. 39, no. 6, pp. 1704-1709, Dec. 2003.

[12]   Z. Zhang, Y. Yan, S. Yang and Z. Bo, "Principle of operation and feature investigation of a new topology of hybrid excitation synchronous machine," IEEE Trans. Magn., vol. 44, no. 9, pp. 2174-2180, Sep. 2008

[13]   Y. Liu, Z. Zhang and X. Zhang, "Design and optimization of hybrid excitation synchronous machines with magnetic shunting rotor for electric vehicle traction applications," *IEEE Trans. Ind. Appl.*, vol. 53, no. 6, pp. 5252-5261, Nov.-Dec. 2017.

[14]   W. Geng, Z. Zhang, K. Jiang and Y. Yan, "A new parallel hybrid excitation machine: permanent-magnet variable-reluctance machine with bidirectional field-regulating capability," *IEEE Trans. Ind. Electron.*, vol. 62, no. 3, pp. 1372-1381, March. 2015

[15]   L. Sun, Z. Zhang, L. Yu and X. Gu, "Development and analysis of a new hybrid excitation brushless DC generator with flux modulation Effect," *IEEE Trans. Ind. Electron.*, vol. 66, no. 6, pp. 4189-4198, Jun. 2019.

[16] L. Sun, Z. Zhang, X. Gu, L. Yu and J. Li, "Analysis of reactive power compensation effect of a new hybrid excitation brushless DC generator," *IEEE Trans. Ind. Electron.*, early access. 2019.

[17] O. Beik and N. Schofield, "An offshore wind generation scheme with a high-voltage hybrid generator, HVDC interconnections, and transmission," *IEEE Trans. Power Del.*, vol. 31, no. 2, pp. 867-877, Apr. 2016

[18] O. Beik and N. Schofield, "High-voltage hybrid generator and conversion system for wind turbine applications," *IEEE Trans. Ind. Electron.*, vol. 65, no. 4, pp, Apr. 2018

[19] A. S. Al-Adsani and O. Beik, "Characterization of a Hybrid PM Generator Using a 32-Phase Brushless Excitation Scheme," *IEEE Trans. Energy Convers.*, vol. 34, no. 3, pp. 1391-1400, Sep. 2019

[20] S. Al-Adsani and O. Beik, "Design of a multiphase hybrid permanent magnet generator for series hybrid EV," *IEEE Trans. Energy Convers.*, vol. 33, no. 3, pp. 1499-1507, Sep. 2018

[21] O. Beik and A. S. Al-Adsani, "Parallel Nine-Phase Generator Control in a Medium Voltage DC Wind System," *IEEE Trans. Ind. Electron.*, early access. 2019

[22] Y. Wang, W. Fu, and S. Niu, "A novel structure of dual-stator hybrid excitation synchronous motor", *IEEE Trans. Appl. Supercond.*, vol. 26, no. 1-4, Jun. 2016.

[23] J. Li and K. Wang, "A parallel hybrid excited machine using consequent pole rotor and AC field winding," *IEEE Trans. Magn.*, vol. 55, no. 6, pp. 1-5, June 2019

[24] D. Wang, D. Zhang, D. Xue, C. Peng and X. Wang, "A new hybrid excitation permanent magnet machine with an independent AC excitation port," *IEEE Trans. Ind. Electron.*, vol. 66, no. 8, pp. 5872-5882, Aug. 2019.

[25] D. Wang, C. Peng, D. Xue, D. Zhang and X. Wang, "Performance assessment and comparative study of a permanent magnet machine with axial flux regulator," *IEEE Trans. Energy Convers.*, vol. 34, no. 3, pp. 1522-1531, Sep. 2019

[26] S. Zhu, C. Liu, K. Wang, and Y. Ning, "A two-stage brushless excitation method for hybrid excitation synchronous generator," *IEEE Trans. Magn.*, vol. 51, no. 6, pp. 1-11, Jun. 2015

[27] S. Zhu, C. Liu, K. Wang, and Y. Ning, "Magnetic field distribution and operating characteristics of a hybrid excitation generator based on integrated brushless excitation," *IEEE Trans. Magn.*, vol. 52, no. 9, pp. 1-12, Sept. 2016

[28] Hussain, S. Atiq and B. Kwon, "Consequent-pole hybrid brushless wound-rotor synchronous machine," *IEEE Trans. Magn.*, vol. 54, no. 11, pp. 1-5, Nov. 2018

[29] M. Ayub, G. Jawad and B. Kwon, "Consequent-pole hybrid excitation brushless wound field synchronous machine with fractional slot concentrated winding," *IEEE Trans. Magn.*, vol. 55, no. 7, pp. 1-5, Jul. 2019.

[30] K. T. Chau, C. C. Chan and C. Liu, "Overview of permanent-magnet brushless drives for electric and hybrid electric vehicles," *IEEE Trans. Ind. Electron.*, vol. 55, no. 6, pp. 2246-2257, June 2008.

[31] M. Cheng, W. Hua, J. Zhang, and W. Zhao, "Overview of stator-permanent magnet brushless machines", *IEEE Trans. Ind. Electron.*, vol. 58, no. 11, pp. 5087-5101, Nov. 2011.

[32] Y. Liao, F. Liang, T. A. Lipo, "A novel permanent magnet motor with doubly salient structure", *IEEE Trans. Ind. Appl.*, vol. 31, pp. 1069-1078, Oct. 1995

[33] M. Cheng, K. T. Chau and C. C. Chan, "Design and analysis of a new doubly salient permanent magnet motor," *IEEE Trans. Magn.*, vol. 37, no. 4, pp. 3012-3020, Jul. 2001.

[34] Z. Q. Zhu and J. T. Chen, "Advanced flux-switching permanent magnet brushless machines," *IEEE Transactions on Magn*, vol. 46, no. 6, pp. 1447-1453, Jun. 2010.

[35] W. Hua, M. Cheng, Z. Q. Zhu and D. Howe, "Analysis and optimization of back EMF waveform of a flux-switching permanent magnet motor," *IEEE Trans. Energy Convers.*, vol. 23, no. 3, pp. 727-733, Sep. 2008

[36] R. P. Deodhar, S. Andersson, I. Boldea and T. J. E. Miller, "The flux-reversal machine: a new brushless doubly-salient permanent-magnet machine," *IEEE Trans. Ind. Appl.*, vol. 33, no. 4, pp. 925-934, Jul. 1997

[37] H. Y. Li and Z. Q. Zhu, "Analysis of flux-reversal permanent-magnet Machines with different consequent-pole PM topologies," *IEEE Trans. Magn.*, vol. 54, no. 11, pp. 1-5, Nov. 2018

[38] Z. Chen, B. Wang, Z. Chen and Y. Yan, "Comparison of flux regulation ability of the hybrid excitation doubly salient machines," *IEEE Trans. Ind. Electron.*, vol. 61, no. 7, pp. 3155-3166, Jul. 2014.

[39] Z. Zhang, Y. Tao, Y. Yan, "Investigation of a new topology of hybrid excitation doubly salient brushless DC generator," *IEEE Trans. Ind. Electron.*, vol. 59, no. 6, pp. 2550-2556, Jun. 2012

[40] W. Hua, G. Zhang, and M. Cheng, "Flux-regulation theories and principles of hybrid-excited flux-switching machines", *IEEE Trans. Ind. Electron.*, vol. 62, no. 9, pp. 5359-5369, Sep. 2015.

[41] J. T. Chen, Z. Q. Zhu, S. Iwasaki and R. P. Deodhar, "A novel hybrid-excited switched-flux brushless ac machine for EV/HEV applications," *IEEE Trans. Veh. Technol.*, vol. 60, no. 4, pp. 1365-1373, May 2011.

[42] E. Sulaiman, T. Kosaka and N. Matsui, "High power density design of 6-slot 8-pole hybrid excitation flux switching machine for hybrid electric vehicles," *IEEE Trans. Magn.*, vol. 47, no. 10, pp. 4453-4456, Oct. 2011

[43] A. Nasr, S. Hlioui, M. Gabsi, M. Mairie and D. Lalevee, "Design optimization of a hybrid-excited flux-switching machine for aircraft-safe DC power generation using a diode bridge rectifier," *IEEE Trans. Ind. Electron.*, vol. 64, no. 12, pp. 9896-9904, Dec. 2017.

[44] Y. Gao, D. Li, R. Qu, X. Fan, J. Li and H. Ding, "A novel hybrid excitation flux reversal machine for electric vehicle propulsion," *IEEE Trans. Veh. Technol.*, vol. 67, no. 1, pp. 171-182, Jan. 2018

[45] Z. Pan, S. Fang, H. Lin, H. Yang, L. Qin and S. Lyu, "A new hybrid-excited flux reversal arc permanent magnet machine having partitioned stators for large telescope application," *IEEE Trans. Magn.*, vol. 55, no. 7, pp. 1-10, Jul. 2019

[46] H. Hua, Z. Q. Zhu, H. L. Zhan, "Novel consequent-pole hybrid excited machine with separated excitation stator", *IEEE Trans. Ind. Electron.*, vol. 63, no. 8, pp. 4718-4728, Aug. 2016.

[47] H. Hua, Z. Q. Zhu, "Novel parallel hybrid excited machines with separate stators", *IEEE Trans. Energy Convers.*, vol. 31, no. 3, pp. 1212-1220, Sep. 2016.

[48] X. D. Xue, K. W. E. Cheng, T. W. Ng and N. C. Cheung, "Multi-objective optimization design of in-wheel switched reluctance motors in electric vehicles," *IEEE Trans. Ind. Electron.*, vol. 57, no. 9, pp. 29-29, Sept. 2010.

[49] B. C. Mecrow, E. A. El-Kharashi, J. W. Finch and A. G. Jack, "Preliminary performance evaluation of switched reluctance motors with segmental rotors," *IEEE Trans. Energy Convers.*, vol. 19, no. 4, pp. 679-686, Dec. 2004

[50] K. Nakamura, K. Murota, and O. Ichinokura, "Characteristics of a novel switched reluctance motor having permanent magnets between the stator pole-tips", Proc. Eur. Conf. Power Electron. Appl., pp. 1-5, Sep. 2007.

[51] P. Andrada, B. Blanqué, E. Martínez, M. Torrent, "A novel type of hybrid reluctance motor drive", *IEEE Trans. Ind. Electron.*, vol. 61, no. 8, pp. 4337-4345, Aug. 2014.

[52] J. Zhu, K. W. E. Cheng and X. Xue, "Design and analysis of a new enhanced torque hybrid switched reluctance motor," *IEEE Trans. Energy Convers.*, vol. 33, no. 4, pp. 1965-1977, Dec. 2018.

[53] S. Ullah, and G. J. Atkinson, "A permanent magnet assist, segmented rotor, switched reluctance drive for fault tolerant aerospace applications," *IEEE Trans on Ind. Appl.*, vol. 55, no. 1, pp. 298-305, Jan.-Feb. 2019.

[54] X. Liu, Z. Q. Zhu, "Electromagnetic performance of novel variable flux reluctance machines with DC-field coil in stator", IEEE Trans. Magn., vol. 49, no. 6, pp. 3020-3028, Jun. 2013.

[55] X. Liu and Z. Q. Zhu, "Stator rotor pole combinations and winding configurations of variable flux reluctance machines," *IEEE Trans. Ind. Appl*, vol. 50, no. 6, pp. 3675-3684, Nov.-Dec. 2014.

[56] X. Liu, Z. Q. Zhu, "Comparative study of novel variable flux reluctance machines with doubly fed doubly salient machines", *IEEE Trans. Magn.*, vol. 49, no. 7, pp. 3838-3841, Jul. 2013.

[57] I. A. A. Afinowi, Z. Q. Zhu, Y. Guan, J. Mipo and P. Farah, "Hybrid-excited doubly salient synchronous machine with permanent magnets between adjacent salient stator poles," *IEEE Trans. Magn.*, vol. 51, no. 10, pp. 1-9, Oct. 2015

[58] M. Zheng, Z. Q. Zhu, S. Cai and S. Xue, "A novel modular stator hybrid-excited doubly salient synchronous machine with stator slot permanent magnets," *IEEE Trans. Magn.*, vol. 55, no. 7, pp. 1-9, Jul. 2019

[59] Ishizaki, A.; Tanaka, T.; Takasaki, K.; Nishikata, S., "Theory and optimum design of PM Vernier motor," *Electrical Machines and Drives, 1995. Seventh International Conference on (Conf. Publ. No. 412)*, pp. 208-212, 11-13, Sept. 1995.

[60] Hosoya, R.; Shimada, H. and Shimomura, S., "Design of a ferrite magnet Vernier machine for an in-wheel machine," *Energy Conversion Congress and Exposition (ECCE), 2011 IEEE*, pp.2790-2797, 17-22 Sept. 2011

[61] L. Jian, Y. Shi, C. Liu, G. Xu, Y. Gong, and C. C. Chan, "A novel dual-permanent-magnet-excited machine for low-speed large torque applications," *IEEE Trans. Magn.*, vol. 49, no. 5, pp. 2381–2384, May 2013

[62] D. Jang and J. Chang, "Design of a Vernier machine with PM on both sides of rotor and stator," *IEEE Trans. Magn.*, vol. 50, no. 2, pp. 877-880, Feb. 2014.

[63] Q. Wang, S. Niu, "A novel hybrid-excited dual-PM machine with bidirectional flux modulation", *IEEE Trans. Energy Convers.*, vol. 32, no. 2, pp. 424-435, Jun. 2017.

[64] Q. Wang, S. Niu, L. Yang, "Design optimization of a novel scale-down hybrid-excited dual permanent magnet generator for direct-drive wind power application", *IEEE Trans. Magn.*, vol. 54, no. 3, pp. 1-4, Mar. 2018.

[65] K. Atallah and D. Howe, "A novel high-performance magnetic gear," in *IEEE Trans. Magn.*, vol. 37, no. 4, pp. 2844-2846, Jul. 2001.

[66] K. Atallah, S. D. Calverley and D. Howe, "Design, analysis and realisation of a high-performance magnetic gear," IET Electr. Power Appl., vol. 151, no. 2, pp. 135-143, 9 Mar. 2004.

[67] P. O. Rasmussen, T. O. Andersen, F. T. Jorgensen and O. Nielsen, "Development of a high-performance magnetic gear," *IEEE Trans. Ind. Appl.*, vol. 41, no. 3, pp. 764-770, May 2005.

[68] J. Rens, R. Clark, S. Calverley, K. Atallah and D. Howe, "Design, analysis and realization of a novel magnetic harmonic gear," *International Conference on Electrical Machines (ICEM)*, Vilamoura, pp. 1-4. 2008

[69] J. Rens, K. Atallah, S. D. Calverley, D. Howe, "A novel magnetic harmonic gear", *IEEE Trans. Ind. Appl.*, vol. 46, no. 1, pp. 206-212, Feb. 2010.

[70] K. T. Chau, D. Zhang, J. Z. Jiang, C. Liu "Design of a magnetic-geared outer-rotor permanent-magnetic brushless motor for electric vehicles", *IEEE Trans. Magn.*, vol. 43, no. 6, pp. 2504-2506, Jun. 2007.

[71] L. Jian, K. T. Chau and J. Z. Jiang, "A magnetic-geared outer-rotor permanent-magnet brushless machine for wind power generation," *IEEE Trans. Ind. Appl.*, vol. 45, no. 3, pp. 954-962, May 2009

[72] E. Gouda , S. Mezani, L. Baghli, and A. Rezzoug, "Comparative study between mechanical and magnetic planetary gears," *IEEE Trans. Magn.*, vol. 47, no. 2, pp. 439–450, Feb. 2011

[73] K. Atallah, J. Rens, S. Mezani, D. Howe, "A novel "pseudo" direct-drive brushless permanent magnet machine", *IEEE Trans. Magn.*, vol. 44, no. 11, pp. 4349-4352, Nov. 2008.

[74] P. M. Tlali, S. Gerber, and R. J. Wang, "Optimal design of an outer-stator magnetically geared permanent magnet machine", *IEEE Trans. Magn.*, vol. 52, no. 2, Feb. 2016.

[75] L. L. Wang, J. X. Shen, P. C. K. Luk, W. Z. Fei, C. F. Wang, H. Hao, "Development of a magnetic-geared permanent-magnet brushless motor", *IEEE Trans. Magn.*, vol. 45, no. 10, pp. 4578-4581, Oct. 2009.

[76] Y. Fan, L. Zhang, J. Huang, X. Han, "Design analysis and sensorless control of a self-decelerating permanent-magnet in-wheel motor", *IEEE Trans. Ind. Electron.*, vol. 61, no. 10, pp. 5788-5797, Oct. 2014

[77] Q. Wang, S. Niu, S. Yang, "Design optimization and comparative study of novel magnetic-geared permanent magnet machines", *IEEE Trans. Magn.*, vol. 53, no. 6, Jun. 2017

[78] X. Guo, S. Wu, W. Fu, Y. Liu, Y. Wang, and P. Zeng, "Control of a dual-stator flux-modulated motor for electric vehicles", *Energies*, vol. 9, no. 7, pp. 517, 2016.

[79] Y. Chen, W. Fu, and X. Weng, "A concept of general flux-modulated electric machines based on a unified theory and its application to developing a novel doubly-fed dual-stator motor", *IEEE Trans. Ind. Electron.*, vol. 64, no. 12, pp. 1-9, Dec. 2017.

[80] C. H. Lee, "Vernier Motor and Its Design," *IEEE Trans. Power App. and Systems*, vol. 82, no. 66, pp. 343-349, Jun 1963.

[81] A.Ishizaki, T.Tanaka, K.Takasaki, and S.Nishikata, "Theory and optimum design of PM Vernier motor," Proc. of IEE ICEMD, pp.208-212, 1995

[82] A. Toba, and T. A. Lipo, "Novel dual-excitation permanent magnet Vernier PM machine", *Conf. Rec. IEEE IAS Annu. Meeting*, pp. 2539-2544, 1999.

[83] A. Toba, and T. A. Lipo, "Generic torque-maximizing design methodology of surface permanent-magnet Vernier machine", *IEEE Trans. Ind. Appl.*, vol. 36, no. 6, pp. 1539-1546, Nov. 2000.

[84] B. Kim and T. A. Lipo, "Operation and design principles of a PM Vernier motor," *IEEE Trans. Ind. Appl.*, vol. 50, no. 6, pp. 3656-3663, Dec. 2014

[85] J. Li, and K. T. Chau, J. Z. Jiang, C. Liu and W. Li, "A new efficient permanent-magnet Vernier machine for wind power generation," *IEEE Trans. Magn.*, vol. 46, no. 6, pp. 1475-1478, Jun 2010

[86] D. Li, R. Qu and T. A. Lipo, "High-power-factor Vernier permanent-magnet machines," *IEEE Trans. Ind. Appl.*, vol. 50, no. 6, pp. 3664-3674, Nov. 2014

[87] D. Li, R. Qu, W. Xu, J. Li and T. A. Lipo, "Design procedure of dual-stator spoke-array Vernier permanent-magnet machines," *IEEE Trans. Ind. Appl.*, vol. 51, no. 4, pp. 2972-2983, Aug. 2015

[88] W. Liu and T. A. Lipo, "Analysis of consequent pole spoke type Vernier permanent magnet machine with alternating flux barrier design," *IEEE Trans. Ind. Appl.*, vol. 54, no. 6, pp. 5918-5929, Dec. 2018.

[89] X. Ren, D. Li, R. Qu, Z. Yu and Y. Gao, "Investigation of spoke array permanent magnet Vernier machine with alternate flux bridges," *IEEE Trans. Energy Convers.*, vol. 33, no. 4, pp. 2112-2121, Dec. 2018

[90] K. Kiyota, T. Kakishima and A. Chiba, "Comparison of test result and design stage prediction of switched reluctance motor competitive with 60-kW rare-earth PM motor," *IEEE Trans. Ind. Electron.*, vol. 61, no. 10, pp. 5712-5721, Oct. 2014.

[91] Z. Chen, and Y. Yan, "A doubly salient starter-generator with two-section twisted-rotor structure for potential future aerospace application", *IEEE Trans. Ind. Electron.* vol. 59, no. 9, pp. 88-95, Sept. 2012

[92] C. Yu and S. Niu, "Development of a magnetless flux switching machine for rooftop wind power generation," *IEEE Trans on Energy Convers*, vol. 30, no. 4, pp. 1703-1711, Dec. 2015.

[93] J. T. Shi, X. Liu, D. Wu and Z. Q. Zhu, "Influence of stator and rotor pole arcs on electromagnetic torque of variable flux reluctance machines," *IEEE Trans. Magn.*, vol. 50, no. 11, pp. 1-4, Nov. 2014.

[94] D. H. Lee, T. H. Pham and J. W. Ahn, "Design and operation characteristics of four-two pole high-speed SRM for torque ripple reduction," *IEEE Trans. Ind. Electron*, vol. 60, no. 9, pp. 3637-3643, 2013.

[95] C. H. T. Lee, K. T. Chau, C. Liu, T. W. Ching and F. Li, "Mechanical offset for torque ripple reduction for magnetless double-stator doubly salient machine," *IEEE Trans. Magn.*, vol. 50, no. 11, pp. 1-4, Nov. 2014.

[96] S. Jia, R. Qu, J. Li, D. Li and H. Lu, "Design considerations of stator DC-winding excited Vernier reluctance machines based on the magnetic gear effect," *IEEE Trans. Ind. Appl.*, vol. 53, no. 2, pp. 1028-1037, April 2017.

[97] Z. Q. Zhu and B. Lee, "Integrated field and armature current control for dual three-phase variable flux reluctance machine drives," *IEEE Trans on Energy Convers.,* vol. 32, no. 2, pp. 447-457, June 2017.

[98] Q. Wang, S. Niu and X. Luo, "A novel hybrid dual-PM machine excited by AC with DC bias for electric vehicle propulsion," *IEEE Trans. Ind. Electron.,* vol. 64, no. 9, pp. 6908-6919, Sept. 2017.

[99] S. Jia, D. Li, and R. Qu, "A high torque density concentrated winding vernier reluctance machine with DC-biased current," *IEEE Trans. Magn.*, vol. 54, no. 11, pp. 1-5, Nov. 2018.

[100] S. Jia, R. Qu, J. Li, D. Li and W. Kong, "A stator-PM consequent-pole Vernier machine with hybrid excitation and DC-biased sinusoidal current," *IEEE Trans. Magn.*, vol. 53, no. 6, pp. 1-4, June 2017.

[101] S. Jia, and R. Qu, "Hybrid excitation stator PM vernier machines with novel DC-biased sinusoidal armature current," *IEEE Trans. Ind. Appl*, vol. 54, no. 2, pp. 1339-1348, Mar. 2018.

[102] L. Chedot, G. Friedrich, J.-M. Biedinger, and P.Macret, "Integrated starter generator: The need for an optimal design and control approach, application to a permanent magnet machine," *IEEE Trans. Ind. Electron.*, vol. 43, no. 2, pp. 551–559, Mar. 2007.

[103] A. Bruyere, and J.C. Mipo, "Modeling and control of a seven-phase claw-pole integrated starter alternator for micro-hybrid automotive applications," in *Proc. IEEE Veh. Power Propulsion Conf.*, pp. 1–6, 2008.

[104] S. Chen, B. Lequesne, R. R. Henry, Y. Xue, and J. J. Ronning, "Design and testing of a belt driven induction starter generator," in *Proc. IEEE IEMDC*, pp. 2–9, 2001.

[105] R. Bojoi, A. Cavagnino, M. Cossale, A. Tenconi, "Multiphase starter generator for a 48-V mini-hybrid powertrain: Design and testing", *IEEE Trans. Ind. Appl.*, vol. 52, no. 2, pp. 1750-1758, Mar. 2016.

[106] A. Tenconi, A. Tenconi and S. Vaschetto, "Experimental characterization of a belt-driven multiphase induction machine for 48-V automotive applications: losses and temperatures assessments", *IEEE Trans. Ind. Appl.*, vol. 52, no. 2, pp. 1-9, Apr. 2016.

[107] R. Bojoi, A. Cavagnino, A. Tenconi and S. Vaschetto, "Control of shaft-line-embedded multiphase starter/generator for aero-Engine," *IEEE Trans. Ind. Electron.*, vol. 63, no. 1, pp. 641-652, Jan. 2016.

[108] C. F. Wang, M. J. Jin, J. X. Shen, and C. Yuan, "A permanent magnet integrated starter generator for electric vehicle onboard range extender application," *IEEE Trans. Magn.*, vol. 48, no.4, pp. 1625–1628, Apr. 2012.

[109] J. Wei, B. Zhou, M. Shi and Y. Liu, "The control strategy of open-winding permanent magnet starter-generator with inverter-rectifier topology," *IEEE Trans. Ind. Inform,* vol. 9, no. 2, pp. 983-991, May 2013.

[110] M. C. Kulan, N. J. Baker, "Design and analysis of compressed windings for a permanent magnet integrated starter generator", *IEEE Trans. Ind. Appl.*, vol. 53, no. 4, pp. 3371-3378, Aug. 2017.

[111] A. V. Radun, C. A. Ferreira and E. Richter, "Two-channel switched reluctance starter/generator results," *IEEE Trans. Ind. Appl.*, vol. 34, no. 5, pp. 1026-1034, Sept.-Oct. 1998.

[112] N. Schofield, and S. Long, "Generator operation of a switched reluctance starter/generator at extended speeds," *IEEE Transactions on vehicular technology*, vol. 58, no. 1, pp. 48-56, 2009.

[113] W. Ding and D. Liang, "A fast analytical model for an integrated switched reluctance starter generator," *IEEE Trans. Energy Convers.*, vol. 25, no. 4, pp. 948–956, Dec. 2010.

[114] I. A. Viorel, R. Munteanu, and D. Fodorean, "On the possibility to use a hybrid synchronous machine as an integrated starter-generator," *IEEE International Conference on Industrial Technology*, pp. 1195-1200, 2006.

[115] E. Afjei, H. Toliyat, H. Moradi, "A novel hybrid brushless dc motor/generator for hybrid vehicles applications", *Proc. Int. Conf. Power Electron. Drives Energy Syst.*, pp. 1-6, 2006.

[116] Z. Zhang, Y. Liu and J. Li, "A HESM-Based variable frequency AC starter-generator system for aircraft applications," *IEEE Trans. Energy Convers.*, vol. 33, no. 4, pp. 1998-2006, Dec. 2018.

[117] C. Liu, K. T. Chau, and J. Z. Jiang, "A permanent-magnet hybrid brushless integrated starter–generator for hybrid electric vehicles", *IEEE Trans. Ind. Electron.*, vol. 57, no. 12, pp. 4055-4064, Dec. 2010.